H2020-SC5-2016-TwoStage – Raw materials Innovation action / Intelligent mining on land	
Project title:	Real-Time Mineral X-Ray Analysis for Efficient and Sustainable Mining
Project acronym:	X-Mine
Grant Agreement No:	730270
Deliverable D1.2	**3D near-mine ore models for target sites**
Associated WP 1	Ore Deposit Modelling
Associated Tasks	Task 1.2
Due Date	31/05/2019
Date Delivered	16/07/2019
Prepared by (Lead Partner)	SGU
Partners involved	SGU, ORE, LOV, HG, AMED, HCM, IGR, UU
Authors in alphabetical order/partner. Names in bold are key and contributing authors.	Ildiko Antal Lundin**, Nikolaos Arvanitidis (SGU)**, Ronald Arvidsson (SGU), **Edine Bakker (SGU), Johan Jönberger (SGU), Peter Hedin (SGU), Stefan Luth (SGU), Edward Lynch (SGU),** Mats Thörnelöf (SGU), **Mikael Bergqvist (ORE),** Eric Landström (ORE), Karin Högdahl (UU), **Viorica Milu (IGR), Stefan Sädbom (LOV), Desislav Ivanov (AMED),** Ventislav Stoilov (AMED), Vaggelis Bacalis (HG), **Pavlos Tsitsanis (HG),** Ventislav Stoilov (AMED), **Lazaros Georgiou (HCM),** Georgios Kalogeropoulos (HCM).
Dissemination Level	Public (PU)

Abstract

X-Mine's Work Package (WP) 1, "Ore Deposit Modelling", addresses the development of geological 3D-models making use of up-to-date geophysical and geological modelling enhanced with high-resolution drillcore XRF/XRT computed tomography data. The present Deliverable 1.2 (D1.2**),** responding to Task 1.2 of WP1, aims at building 3D near-mine scale ore deposit models for all four mine pilots in Sweden, Greece, Bulgaria and Cyprus by setting up a methodology for performing 3D modelling by integrating available and collected multi-disciplinary geodata mentioned and described in D1.1. The models include the distribution of the rock types, and their alteration zones, the structural setting of mineralisations and their geochemical signatures, together with an interpretation of the continuation of the ores outside of the drilled area. Integrated modelling of geological and geophysical data robust contributes to selective and efficient near- and in- mine exploration and production drilling, when combined with the real-time XRF/XRT sensing and related results obtained by using the drillcore analysis prototypes and corresponding software, built in WP4and further developed based on user feed back, throughout the entire project.

3D and 4D geomodelling is nowadays an efficient tool, applied in better understanding mineral resources appraisal during exploration activities. In the X-Mine project, the 3D-geomodelling applied, was using the software capabilities, the options and the solutions, provided by SKUA-GOCAD and Leapfrog Geo.

In the Swedish Lovisa mining area pilot the presented geological- and geophysical models provide a good three-dimensional understanding on the shape and spatial distribution of the Lovisa, Håkansboda, Stråssa and Blanka ore bodies as well as on their regional geological framework (Guldsmedshyttan syncline). The modelled ore bodies reach between 38 and 1200 meters below the surface, but most bodies are likely to continue to greater depths according to interpretations from geophysical modelling (Stråssa) and drilling (Håkansboda).

In the Bulgarian Assarel, based on the modelled fault network, a total of 122 fault blocks subdivide the near-mine model area. Cross-faulting at both Assarel and Medet comprises c. NE-trending faults that are either bound or cross-cut by WNW- to NNW-oriented faults or shear zones. These structural intersection zones represent areas of higher secondary permeability and likely formed focused areas of increased hydraulic conductivity and fluid flow, which may have promoted Cu ± Au ± Mo mineralization.

The presented models for the Greek Mavres Petres-Piavitsa mining area provide a good three-dimensional overview on the spatial distribution of mineralization and their hosting lithological units along and within the Stratoni fault zone. The combined visualization of geological and geophysical models at various scales contributed to the characterization of the lithological units and the definition and extrapolation of lithological- and tectonic boundaries at depth.

In the Cypriot Skouriotissa-Apliki mining area the3D models highlight a clear connection between the mineralization and the fault structures. This link was known previously, but a more detailed examination is needed to gain a better understanding of the structures themselves and why the mineralization is related to only some of them.

1. Introduction: Background and objectives

1.1. X-Mine: a brief introduction

The X-MINE project supports better resource characterization and estimation as well as more efficient ore extraction in existing mine operations, making the mining of smaller and complex deposits economically feasible and increasing potential European mineral resources (specifically in the context of critical raw materials) without generating adverse environmental impact. The project will implement large-scale demonstrators of novel sensing technologies improving the efficiency and sustainability of mining operations based on X-Ray Fluorescence (XRF), X-Ray Transmission (XRT) technologies, 3D vision and their integration with mineral sorting equipment and mine planning software systems.

The project deploys these technologies in 4 existing mining operations in Sweden, Greece, Bulgaria and Cyprus (Fig. 4.1). The sites have been chosen to illustrate different sizes (from small-scale to large-scale) and different target minerals (zinc-lead-silver-gold, copper-gold) including the presence of associated critical metals such as indium, gallium, germanium, platinum group metals and rare earth elements. The pilots will be evaluated in the context of scientific, technical, socio-economic, lifecycle, health and safety performances. The sensing technologies developed in the project will improve exploration and extraction efficiency, resulting in less blasting required for mining. The technologies will also enable more efficient and automated mineral-selectivity at the extraction stage, improving ore pre-concentration options and resulting in lower use of energy, water, chemicals and men hours (worker exposure) during downstream processing.

The consortium includes 6 industrial suppliers, 4 research/academic organizations, 4 mining companies and 1 mining association. The project has a duration of 3 years and a requested EC contribution of €9.3M.

1.2. Purpose and structure in relation to WP1 & D1.2

WP1 "Ore Deposit Modelling", addresses the development of geological 3D-models making use of up-to-date geophysical and geological modelling enhanced with high-resolution drillcore XRF/XRT computed tomography data. These models are to be used for near-mine exploration (mine planning, drillhole targeting) and in-mine exploration along with ongoing mining exploitation and extractive operations of the ore bodies related to sulphide mineral systems present in the mines selected as demonstrators in this project. The objectives of this WP are:

- To collect available and new multidisciplinary data from 4 mining sites. We will focus upon geological, structural, 3D-geophysical, mineralogical and geochemical, data (task 1.1/D1.1)
- To build 3D ore deposit models for 3 mining sites, using also data collected by new techniques to create new and better ore geological models, and obtain a more accurate geometry of currently mined ore bodies (task 1.2/D1.2)

- To demonstrate the applicability of 3D ore deposit modelling combined with drillcore XRF/XRT real-time sensing to optimise in-mine exploration and mining operations in general. (task 1.3/D1.3)

Deliverable 1.2 (D1.2) responds to Task 1.2 aiming at building 3D near-mine scale ore deposit models for all target sites by setting up a methodology for performing 3D processing/modelling integrating available and collected multi-disciplinary geodata mentioned and described in D1.1, including also any 3D geophysical models determined. Subsurface interpretations in regions with sparse data are based on advanced surface extraction techniques and interpolation from curvilinear grids including multi-geological parameters. Drillcore/drillchip data available and derived from task 1.1, is about to result in initial estimates of ore potential and host rock types, including alteration zones. The models intend to include the distribution of the rock types, and their alteration zones, their mineralogy and their geochemical signatures, together with an interpretation of the continuation of the ores outside of the drilled area. The task anticipates integrating geological and geophysical data to produce robust framework models contributing to selective and efficient near- and in- mine exploration and production drilling, as well as mining planning issues, in combination with the real-time XRF/XRT sensing and related results obtained by using the drillcore analysis prototypes and corresponding software, built in WP4 and further developed based on user feedback, throughout the entire project.

2. 3D Geological Modelling Overview

2.1. Geological understanding in a 3D geospatial environment

3D geomodelling, a computer method for modelling and visualizing geological structures in three spatial dimensions, is a common exploration tool used in oil and gas since more than several decades. When adding time, 4D modelling allows reproducing the dynamic evolution of geological structures and reconstructing the past deformation history of geological formations. 3D geomodelling has been applied to mineral exploration with growing success since more than 15 years but can be considered still challenging for modelling bedrock settings. Even if very few 4D modelling case studies have been carried out in mineral exploration, it nowadays begins to be applied in structural geology and mineral resources exploration.

2.2. Integrated 3D modelling targeting ore exploration

As a matter of fact, 3D and 4D approaches provide significant knowledge and improvements in better understanding the geological background of the mineralization zones, based on compilation of available surface and subsurface data sources. There is a growing interest in many parts of the world, including Europe, in 3D/4D geomodelling to assess mineral potential. Challenges for future developments in the 3D and 4D research geomodelling are: (i) a geological 3D model is never complete. It is continuously developed with the acquisition of new data and new ideas, and automatic procedures would be helpful in up-dating geomodels when new data are acquired; (ii) current 3D and 4D software enables 4D geological structural modelling, and can be used to make more than a single interpretation or model to support a range of alternative interpretations when knowledge of the geologic history is poorly constrained (iii) 3D geomodels contribute to extend the life of a mine.

Mineral exploration collects and uses data coming from different sources of information such as drilling logging, chemical analysis, structural geology, geophysics etc. These data are heterogeneous and need to be integrated on the same platform targeting deep exploration and location of deeper-seated mineral deposits. Partnerships between mining companies, technology providers, public research institutes and geological surveys, such as the X-Mine one, enable the multidisciplinary expertise needed to add exploration value, increase the resource potential and stimulate mining activities in Europe.

2.3. Software packages used

3D and 4D geomodelling is nowadays applied in mineral resources surveys as an exploration tool by geo-practitioners and geoscientists involved in better understanding mineral resources appraisal, both at the mining exploitation and at the exploration stages for identifying potential new mineral resources. Data acquired during mining exploration and exploitation is interpreted and processed using computers. Several packages are available on the market for processing 2D and 3D datasets such as GIS and geomodelers. Among them, the most widely used are: 3D Geomodeler, Intrepid, GOCAD-SKUA for geological applications, GOCAD Mining, AutoCAD, Irap RMS, Isatis, Leapfrog Geo, MicroMine, Microstation, MineSight Implicit Modelling (MSIM), Move3D, Petrel, Surfer, Surpac Gems and Vulcan3D. These software programs generally address one or more specific modelling applications, but none of them can encompass all tasks generally required in an integrated exploration and mine feasibility study, including: structural geology modelling, restoration, geophysical inversion and interpretation, geochemical analysis, resource and reserves estimation, mine planning, mine design and risk and environmental impact mitigation (Fig. 2.1). In the X-Mine project the 3D-geomodelling applied was using the software capabilities, the options and the solutions provided by SKUA-GOCAD and Leapfrog Geo.

3. Primary sources of information and data

To have the best possible applied near- mine 3D geomodelling approach, all available geo-referred data, along with the new ones collected by the X-Mine partners (as also described in the D1.1 already submitted and approved) in the mines and adjacent areas of Lovisa, Assarel, Mavres Petres-Piavitsa and Skouriotissa-Apliki (Tab. 3.1), were used to progress and establish corresponding geomodels.

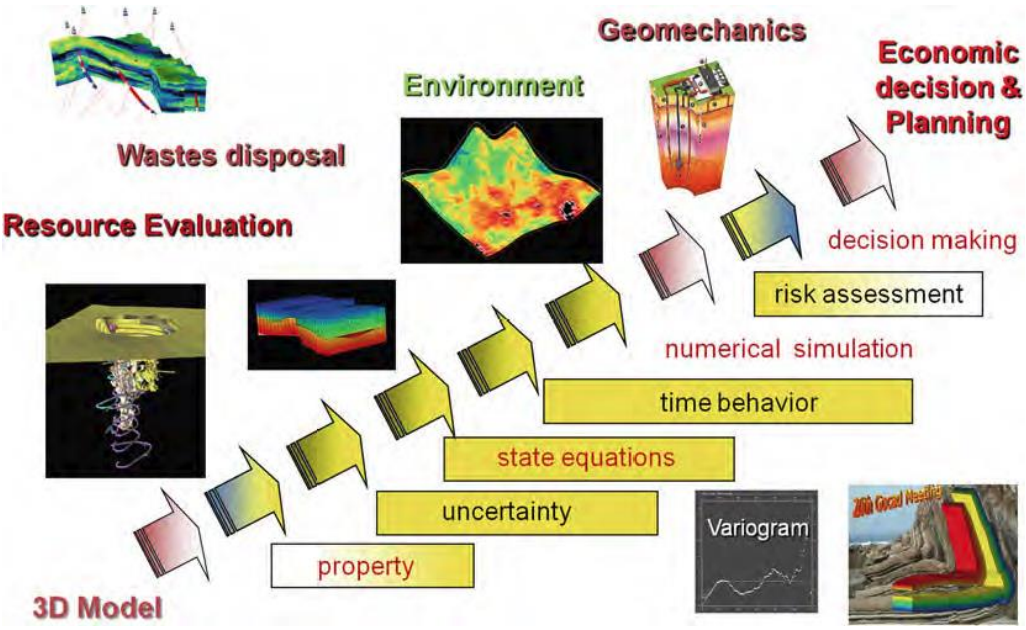

Figure 2.1: Mineral exploration is a complex multidisciplinary activity with 3D- modelling applications having a central and essential role from the early stages to feasibility evaluation and final economic approach

3.1. Geological maps

Available geological maps of various scales and levels of information were used to review and combine lithostratigraphic setting and structural geology with rock types and alteration zones in a more comprehensive way through a regional scale 3D modelling approach focusing and highlighting on features that are "critical" and characteristic for each of the ore deposits targeted.

3.2. Geophysics and petrophysics

Re-evaluation and 3D modelling of available geophysical data and collected petrophysical measurements were integrated into acquired geomodels, targeting a better understanding of mineralised structures and an improved interpretation of related ore-forming processes and systems.

3.3. Drillcore logs and assays

Lithological and structural information obtained from wellbore logs was interpreted and referred to geological mapping and geophysics, and any existing models were considered and evaluated to be potentially incorporated in the X-Mine near-mine modelling.

3.4. XRT-XRF-generated drillcore data

Core samples and intervals from all mines were scanned and the tomographic and compositional results obtained were compared and quality assessed against conventionally analysed and received geochemical and mineralogical data. Some of the scanning results, particularly those related to computed 3D-tomographic structures/textures and density issues, were taken into consideration to improve the near-mine 3D modelling.

Table 3.1: Available and collected data used for near-mine 3D geomodelling in each mine

Mine	**Geological maps**	**Geophysical data**	**Structural data**	**Alteration zones**	**Drillcore logs & assays**	**Scanning results**
Lovisa	Various scales, from regional to local deposit scale	Airborne and ground magnetics and gravity, Petrophysical Samples from surface	Database and maps	Based on available mineralogy and geo-chemistry	Ore grades, Wall-rock-lithologies, mineralisation	Drillcore samples and intervals
Assarel	1:100 000 c. 1:75 000 (see Table 4.2.1 also)	None	None	Maps	None for near-mine model	Outcrop samples Drillcore samples and intervals
Mavres Petres Piavitsa	1:50 000 1:5 000	Airborne electro-magnetics, magnetics, radiometrics, petrophysical samples from surface and boreholes	Data base and maps		Wall rock lithologies Mineralisation Deformation structures	Outcrop samples Drillcore samples and intervals
Skouriotissa Apliki	1:31 680 1:5000	None	Maps	None for near-mine model	Cu-assays	Outcrop samples

4. Building integrated near-mine 3D ore models

Collected available and new (Tab.3.1) multidisciplinary geological, structural, 3D-geophysical, mineralogical and geochemical data, derived from surface, drilling and in-mine surveys, were used to build multi-parameter integrated 3D near-mine ore deposit models for Lovisa, Assarel, Mavres Petres-Piavitsa and Skouriotissa-Apliki mining sites. This approach clearly demonstrates the applicability of 3D ore deposit modelling combined with drillcore XRF/XRT real-time sensing in order to optimise regional and in-mine exploration, and mining operations in general.

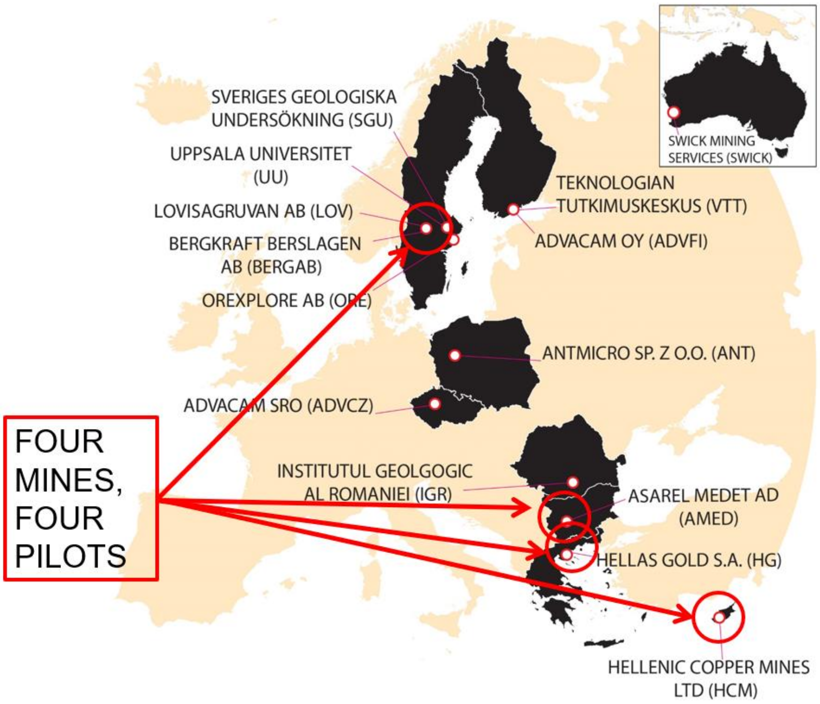

Figure 4.1. Map showing the origin of the X-Mine partners and the location of the four pilot-test mines.

4.1. Lovisa mining area in Sweden

4.1.1. Modelled volumes

Geological modelling near the Lovisa mine has been carried out on a semi-regional to deposit scale (Fig. 4.1). The semi-regional scale model measures 7 x 7 x 2 km and covers largely the area of the high-resolution airborne magnetics survey conducted by SGU in 2017. The purpose of the model is to solve for the complex geometries of the northern tip of the Guldsmedshyttan syncline and to serve as a regional framework for 3D deposit models located in the area. Deposit scale models have been produced for the polymetallic sulfide deposits Lovisa and Håkansboda as well as for the iron-oxides deposits Stråssa and Blanka. The deposit models include multiple ore-bodies of various sizes and shapes reaching depths between 38 and 1200 m below the surface.

4.1.2 Geological setting

The Bergslagen mining province is part of the Bergslagen lithotectonic unit of the Fennoscandian Shield (Stephens and Andersson 2015) (Fig. 4.1.1). The unit largely consists of syn-orogenic plutonic rocks intruded in a succession dominated by felsic metavolcanics rocks, which were deposited in a continental back-arc basin during the Svecokarelian orogeny (1.9 – 1.8 Ga) (Stephens and Andersson 2015). The metavolcanic succession is interbedded by volcanoclastic mass flow deposits, limestone, BIFs and sulphide mineralization. Deformation was polyphase, and metamorphism was low-pressure up to amphibolite facies during metamorphic peak conditions. Large-scale folding and shearing resulted in the formation of inliers of the supracrustal rocks, which became bounded by plutonic rocks and shear zones. A relatively large inlier in western Bergslagen is the 45 km long, NE-trending Guldsmedshyttan syncline, hosting many iron-oxides and base metal sulphide deposits along strike. The deposits for this study (Lovisa, Håkansboda, Stråssa and Blanka) are situated in the northern tip of the syncline (Figs. 4.1.2-4.1.3) (Luth et al. 2019).

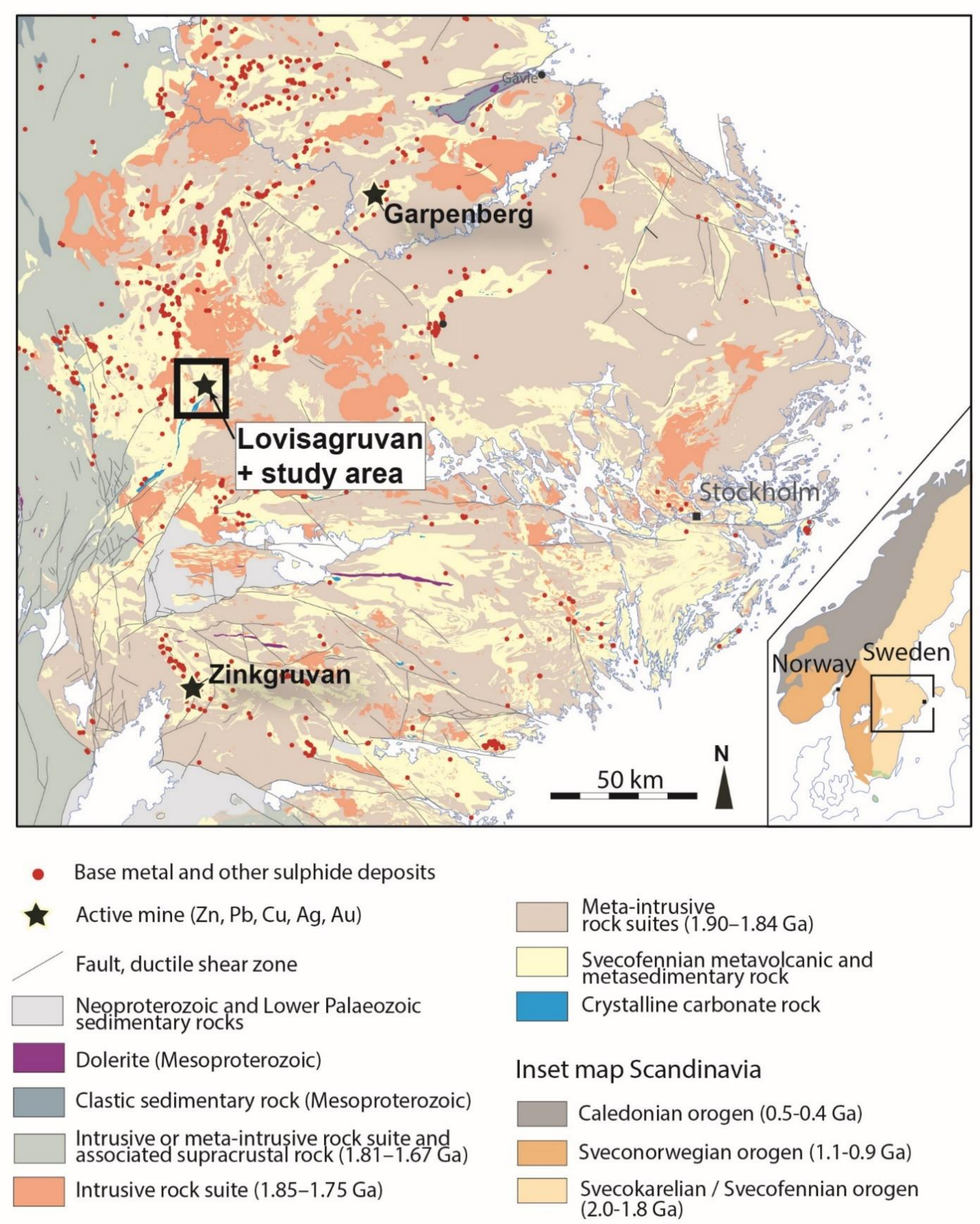

Figure 4.1.1. Geological map of the Bergslagen region including the outline of the study area. Inset shows the main tectonic domains in Norway and Sweden.

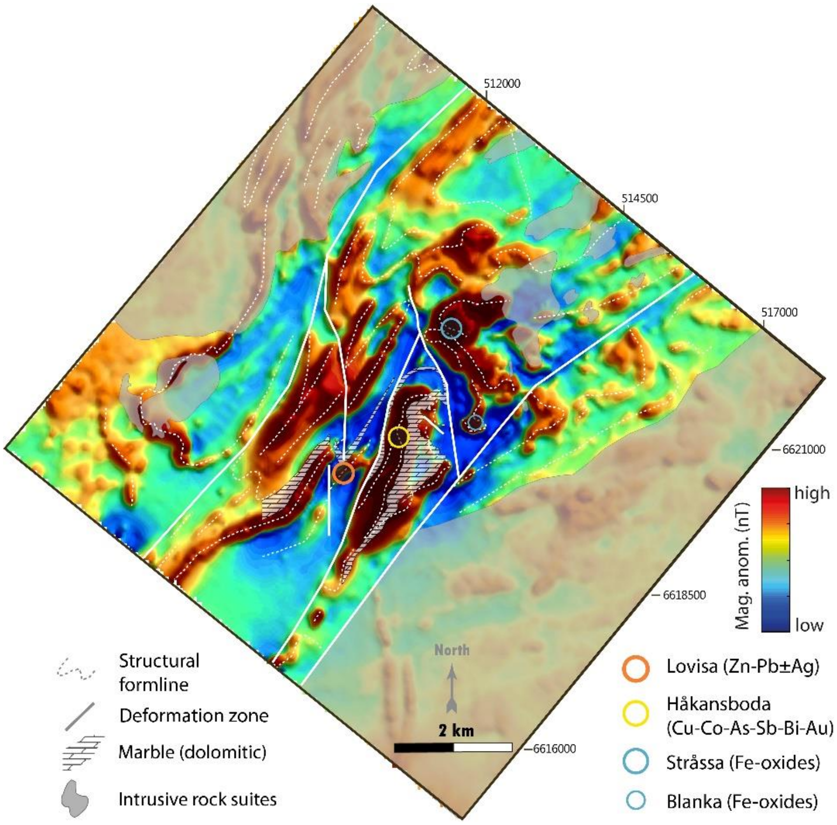

Figure 4.1.2. Magnetic anomaly map including interpreted lineaments (shear zones) and locations of the deposits. The map is based on airborne measurements (100 meters line spacing at 60 meters ground clearance). Black square outlines the semi-regional model area (see Fig. 4.1.3).

4.1.2.1 The Lovisa Zn-Pb-(Ag) deposit

The Lovisa sulphide deposit on the western fold limb of the Guldsmedshyttan syncline (Fig. 4.1.3) is actively mined with a reserve of 675 000 tons ore with zinc (9,5%), lead (3,9%) and some silver (Lovisagruvan AB annual report 2018). The reserve is proven by 90 drill holes 1100 m along strike and down to 425 m and is open at depth and to the south. The Lovisa deposit is stratiform and consists of two steeply dipping horizons (Jansson et al. 2018). A laminated, sphalerite-dominated "Sphalerite Ore" (>15% Zn) and a horizon of galena-dominated "Main ore" (>40% Zn+Pb). The ore layers are separated by a 1 to 3 meters wide zone of barren rock (< 1% Zn+Pb). The total thickness of the ore layers varies between less than 1 m to up to 3 meters. The host rock as well as the interbedded layers between the ore layers are rhyolitic ash siltstones and chloritic schists. The formation of stratiform ore layers is interpreted as syn-genetically in a vent-distal, seafloor exhalative setting (Jansson et al. 2018). Subsequently the ore layers and the surrounding rocks became metamorphosed to upper amphibolite facies and ductile and brittle deformed resulting in post-genetic ore textures (e.g. metablastic growth, shearing and folding, mineral intergrowth) and remobilization (Sahlström et al. 2019).

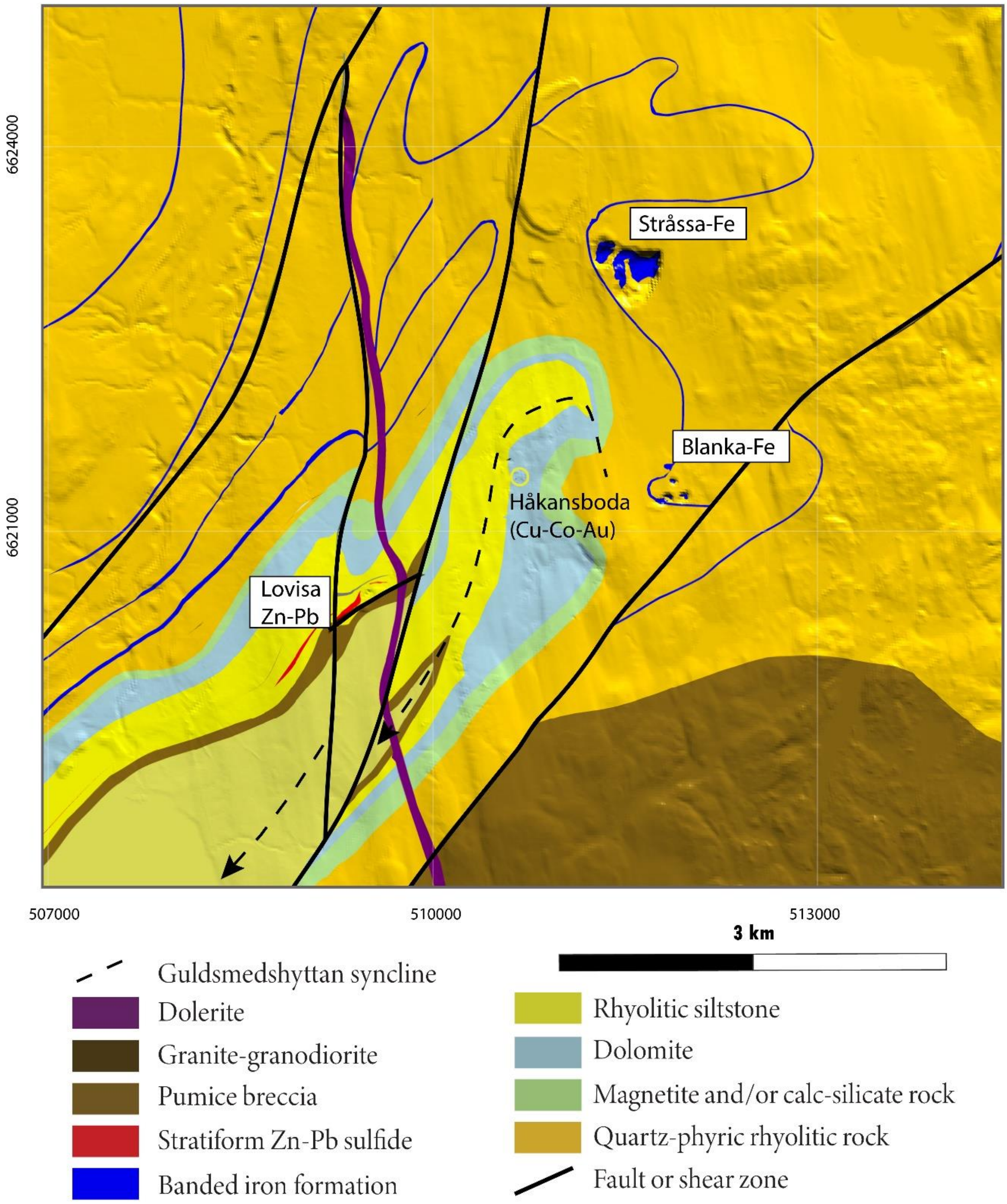

Figure 4.1.3. Geological map of the modelled area including the main deposits. The map is largely based on the map from Jansson et al. (2018) near the Lovisa and Håkansboda deposits, and on Lundström (1983). Lithological contacts and shear zone traces are mainly interpreted from the magnetic anomaly map (see Fig. 4.1.2) and are supplemented by field observations.

4.1.2.2 The Håkansboda (Cu-Co-As-Bi-Au) deposit

The Håkansboda deposit (Fig. 4.1.3) is hosted by massive limestones with interbeds of calc-silicate rocks and rhyolitic ash siltstone and is interpreted to occur on the eastern fold limb and stratigraphically below the stratiform Lovisa deposit (Lundström, 1983; Carlon & Bleeker

1988). Mineralization is known for 850 m along strike and to a depth of 600 m but is open at depth and to the south. The indicated reserve is 629.000 tons of 1,4% Cu, 0,4 g/t Au and 14,3 g/t Ag (in-situ grades) (Kopparberg Mineral AB, 2012). The dominant ore minerals are chalcopyrite, cobaltite, glaucodot, arsenopyrite, pyrrhotite, pyrite, sphalerite and galena, and accessory bismuth minerals (e.g. Magnusson 1973). The ore occurs as massive lenses, schlieren or banded mineralisation, disseminated sulphides and as breccias. The ore textures indicate post-genetic deformation and remobilization (Carlon and Bleeker 1988). Carlon and Bleeker (1988) suggested that the Håkansboda deposit formed in a feeder zone for stratiform mineralization in the area (e.g. Lovisa deposit).

4.1.2.3 The Stråssa and Blanka (Fe-oxide) deposits

The Stråssa iron-oxide deposit (Fig. 4.1.3) consists mainly of quartz-magnetite and hematite ores with variable amounts of magnetite, hematite and skarn minerals (hornblende, diopside, epidote). The iron content varies between 25% and 45%. Sulphides (pyrite, chalcopyrite, and pyrrhotite) occur only locally within the iron ores at Stråssa, however, at Blanka, which is situated at the same stratigraphic horizon 1.7 km south of Stråssa, pyrite and chalcopyrite are more common and are observed mostly in the actinolite skarns (Koark, 1960). In addition, the iron ores from Blanka are less stratified than at Stråssa and intense deformation of the ore bodies resulted in discordant stocks, specularite-schists and large-scale mullions plunging 50° to the SE (Bleeker and Carlon 1988).

4.1.3 Used datasets for geological modelling

The 3D semi-regional model is primarily based on surface data derived from geological maps, structural measurements and airborne derived magnetic anomaly and tilted derivative maps (Fig. 4.1.2). In addition to the pre-exiting geological maps from Lundström 1983 and Jansson et al. 2018, new field data from approximately 150 observations points has been used to constrain the model (Fig. 4.1.4). Cross-sections from Bleeker (1984) and Carlon (1987) added soft constraints to the model but were mainly used as structural concepts. The cross-section published by Jansson et al. (2018) supplied, however, hard constraints as it builds on surface- and drill data (Fig. 4.1.5). The deposit models are based primarily on sub-surface data from drilling, mine maps from the active mining period and structural analysis (e.g Koark).

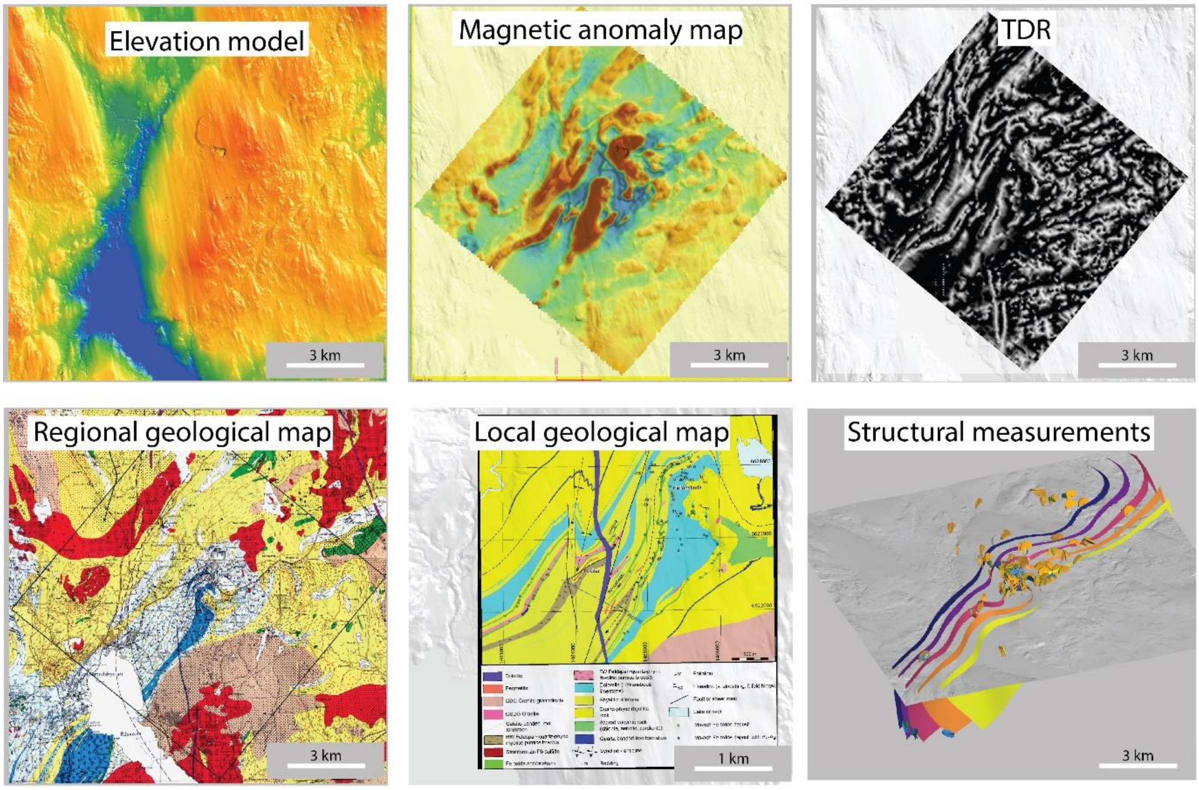

Figure 4.1.4. Surface data sets used for the three-dimensional modelling in this study. Elevation model from Lidar (2 meters resolution). Magnetic data from SGU airborne survey 2017. Regional- and local geological maps are from Lundström (1983) and Jansson et al. (2018), respectively. Structural measurements from SGU field surveys 2017 and 2018.

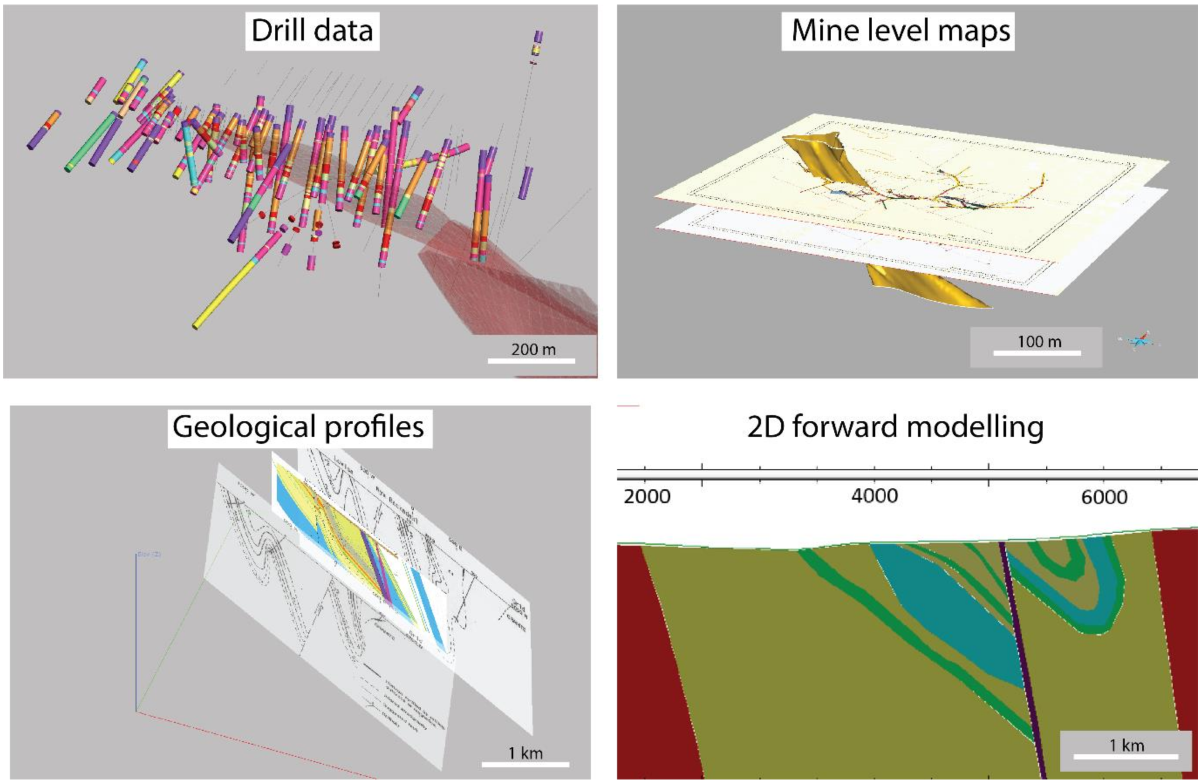

Figure 4.1.5. Subsurface data sets used for the three-dimensional modelling in this study (see text for details).

4.1.4 Methodology geological modelling

4.1.4.1 Deposit scale

Four main deposits located within the semi-regional model space were modelled in three dimensions. Modelling of the Lovisa Zn-Pb-(Ag) deposit was performed in Leapfrog Geo (version 4.4) utilizing mainly drill data and in-mine observations. The outline of the ore body was modelled as a “Vein” allowing for pinch outs between neighboring drill holes that contain or lack mineralization. Away from the drill holes, the modelled ore body was extrapolated down and to the south by assuming a southward continuation parallel to the pumice breccia in the overlying hanging wall. Modelling of the Håkansboda (Cu-Co-Au), Stråssa-Fe and Blanka-Fe deposits was performed in SKUA-GOCAD (Paradigm) using digitized level plans and cross-sections inherited from several mining companies. Following georeferencing the sections in 3D, the outline of the ore bodies was digitized and somewhat simplified but maintaining the general shape and character. Subsequently, the digitized curves from each level were used as a frame to build surfaces from enclosing the ore bodies.

4.1.4.2 Semi-regional scale

Modelling in a semi-regional scale focused on the northern tip of the Guldsmedshyttan syncline in western Bergslagen. At first, fault blocks were defined mainly by geophysical lineaments representing major deformation zones. The dip of the deformation zones was extrapolated from mylonitic fabrics observed in the rocks located within a 200 m distance from the lineament. The deformation zones were then extrapolated down to 2 km (total model depth). Subsequently, the lithology was modelled at depth for each fault block separately using surface data, geological profiles and drilling data. Map traces of lithological contacts were digitized from geological maps and extrapolated to depth at angles consistent to nearby structural measurements. The map from Jansson et al. (2018) was used for the direct surrounding for the Lovisa and Håkansboda mines, whereas the map from Lundström (1983) in combination with magnetic anomaly maps was used to trace the folded horizons of quartz banded iron formations around the Stråssa and Blanka Fe-oxides mines. The modelled surfaces were then modified by subsurface constraints from profiles and drill data. The structural trend of key horizons in the Lovisa fault blocks, such as the Zn-Pb layer, were primarily derived from correlations between drill holes. Modelled surfaces located beyond the extent of drilling (e.g. BIF layers) were mainly modelled as “offset surfaces” trending parallel and within a specified range to neighboring surfaces or local deposit-scale models. In the Håkansboda fault block, the outline of the large synform was highly conceptual and its detailed shape and depth extend are poorly constrained. Sub-surface interpretations based on geophysical modelling (2D forward or 3D inversion) were not implemented in the geological modelling at this stage.

4.1.5 Results of the Geological Modelling

The semi-regional model is divided by major shear zones into 5 fault blocks (Fig. 4.1.6). The Western- and Eastern shear zones are striking NE-SW and dip steeply towards the southeast. Both deformation zones separate the *NW-* and *SE fault blocks* from the model's central region of intense folding and shearing (Guldsmedshyttan syncline) (Fig. 4.1.7). This central region is subdivided by the ESE-dipping Engvall shear zone into the *Håkansboda fault block* and the *Lovisa fault blocks*. The latter is in turn divided by the Lovisa shear into the *Lovisa north-* and *Lovisa south fault block*. The Central shear zone, located within the Lovisa north block, is observed in the Lovisa mine (Jansson et al. 2018) but seems less significant on a semi-regional scale. In the following sections a brief description on the three dimensional lithological and structural build-ups of each fault block is presented (Figs. 4.1.6-4.7).

4.1.5.1 SE fault block

A large part of the SE-block (Fig. 4.1.6) consists of a granite to granodiorite intrusion from the GDG intrusive suite (e.g. Stephens et al. 2008) (Fig. 4.1.7). The overall geometry of the intrusion is poorly constrained at depth and a spheroidal shape is assumed based on the intrusion's surface expression. Interpretations from outcrops and lidar data reveal a distinctive fracture pattern consisting of steeply dipping NNW- and NE-striking fracture sets. The boundary between the granitic intrusion and the metavolcanics rocks in the north is adapted from Lundström (1983) and dips assumably towards the south. The adjacent volcanic rocks to the north consist of quartz-phyric rhyolitic rocks, granitic veins and pegmatite veins. In addition, the succession hosts a stratiform 2 to 20 m thick folded layer of quartz-banded iron formation (BIF), which was mapped by Jansson et al. (2018). The BIF is displaced by the Eastern Shear with an apparent sinistral sense of shear and most likely also a southern-block-up sense of shear with respect to the Håkansboda block. At depth, the BIF-layer is interpreted as the southern limb of an inclined non-cylindrical synform.

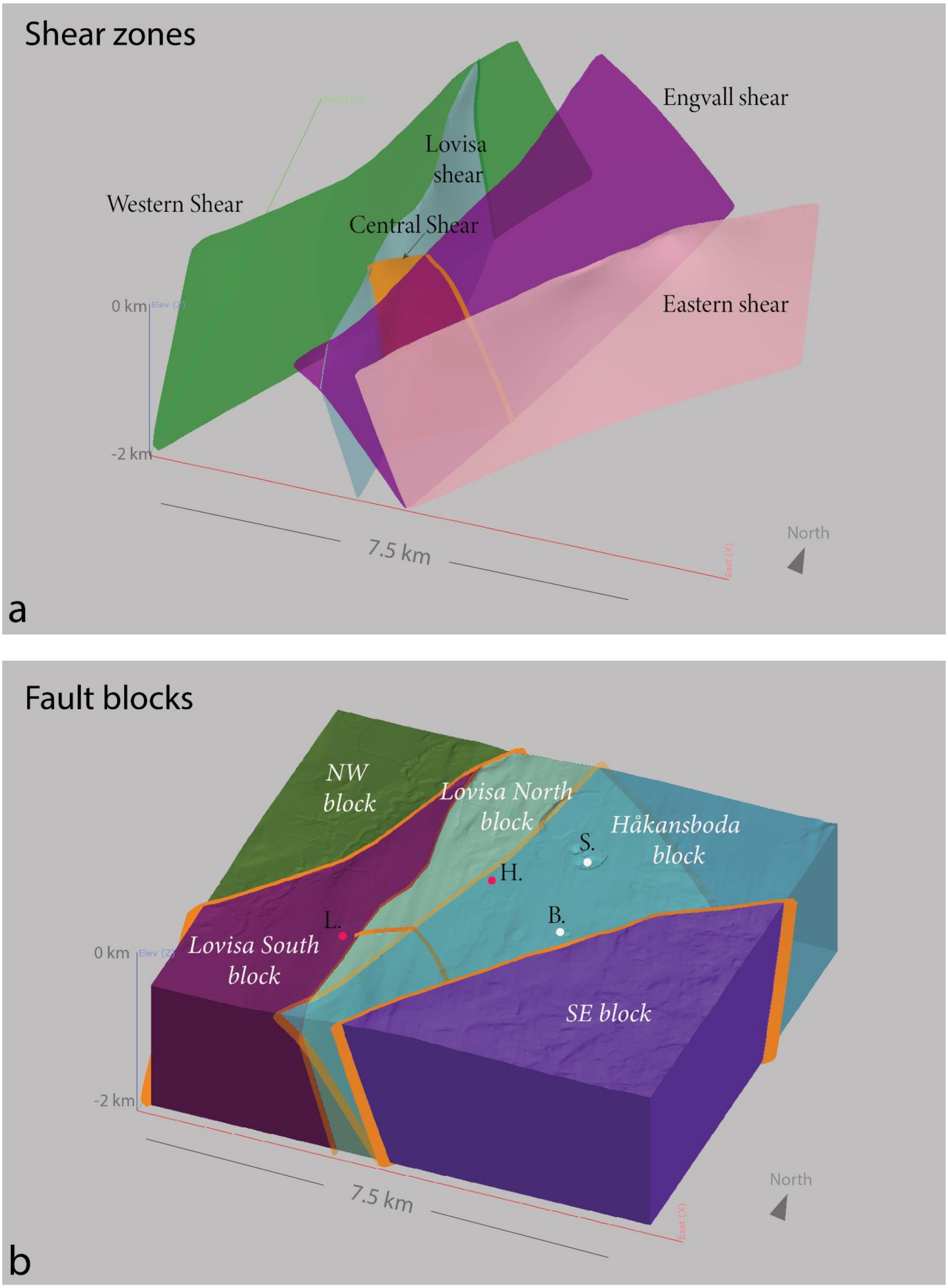

Figure 4.1.6. a) Major shear zones modelled in three dimensions based on geological data. b) Fault block model with bounding deformation zones shown in orange.

4.1.5.2 NW fault block

The NW fault block is bounded by the Western shear in the south and is dominated by quartz-phyric rhyolitic rock (Fig. 4.1.6 and 4.1.7). The two parallel, steeply SE-dipping quartz banded iron layers (BIF) are most likely stratigraphically identical implying that the stratigraphic sequence is folded and partly overturned by a steeply inclined, SW plunging antiform. At the surface, the fold closure of the antiform appears M-shaped on the magnetic anomaly maps and is located to the west of the model space. Furthermore, a gentle refolding of the antiform on a kilometer scale along a NW-SE axial plane may have resulted from drag along the SW-shear zone. Considering the large map extend of the antiform as well as the poor depth constraints, no fold closures were interpreted at depth.

4.1.5.3 Håkansboda fault block

The Håkansboda fault block hosts the refolded northern tip of the Guldsmedshyttan syncline (Figs. 4.1.7 and 4.1.8). The block is bounded to the west by the Engvall shear zone, which intersects on a low angle with the northwestern limb of the main syncline. To the southeast the block is bounded by the SE-shear zone. The Håkansboda block contains a large part of the folded regional stratigraphic sequence (Usken formation). Quartz-phyric rhyolitic rocks dominate in the north and are locally intruded by granitic and pegmatitic rocks (not included in the 3D model). The quartz-banded iron formation (BIF) has been mapped and modelled at depth using the magnetic anomaly maps and structural measurements, respectively. The modelled BIF layer reveals a complex folding pattern with an E-W trending synform in the north tracing into an inclined S-fold pattern between the Stråssa- and Blanka deposits. In general, the fold plunges change from steeply plunging at surface levels to a moderate and shallow plunge at depth. To the southwest, the lithological contacts at the surface are well constrained by the magnetic anomaly maps as well as by a dense network of structural measurements. The data reveals a tight syncline with an axial plane dipping 50 to 60° to the southeast. At depth, the main fold plunges towards the south with local deviations due to parasitic folds along the limbs and refolding along NW-striking axial planes. The syncline deepens towards the southwest and the contact base magnetite-skarn and top rhyolitic-siltstone (stratigraphically below the dolomite) reaches a maximum depth of approximately 1200 m in the southernmost part of the Håkansboda fault block (see also Fig. 4.1.17).

4.1.5.4 Lovisa blocks

The Lovisa fault block is bounded to the east by the Engvall shear zone and is divided by the Lovisa-shear zone into a Lovisa north- and Lovisa south block (Figs. 4.1.7 and 4.1.8). Relative movements along the Lovisa shear zone were approximately 200 meters in a dextral sense of shear as inferred from displacement of strata among the north and south block. More than half of the block consists of quartz-phyric rhyolitic rock interbedded by two layers of quartz banded iron formation (BIF). Like the NW block, the two BIF layers are probably stratigraphically identical indicating isoclinal folding along steeply SE-dipping axial planes. In the Lovisa north block, the BIF layers are refolded as both Z- and S-folds. The overlying

stratigraphy is represented by the Håkansboda dolomite, rhyolitic ash-siltstone with Mn-rich Fe-oxides mineralization, the Lovisa Zn-Pb (Ag) ore horizon and a rhyolitic pumice breccia. The entire sequence is located on the northwestern limb of the Guldsmedshyttan syncline and is dipping moderately to the southeast but appears shallower dipping and gently folded at deeper levels (Fig. 4.1.8). Most of the sub-surface model constraints were obtained from drilling where the Lovisa Zn-Pb-(Ag) ore horizon acted as a reference surface to the surrounding surfaces. The remaining surfaces were modelled as "offset surfaces" in order to maintain a stratigraphic sequence and to prevent these from intersecting. The intersecting dolerite dyke was modelled as a "vein" without pinch out and dips sub vertically.

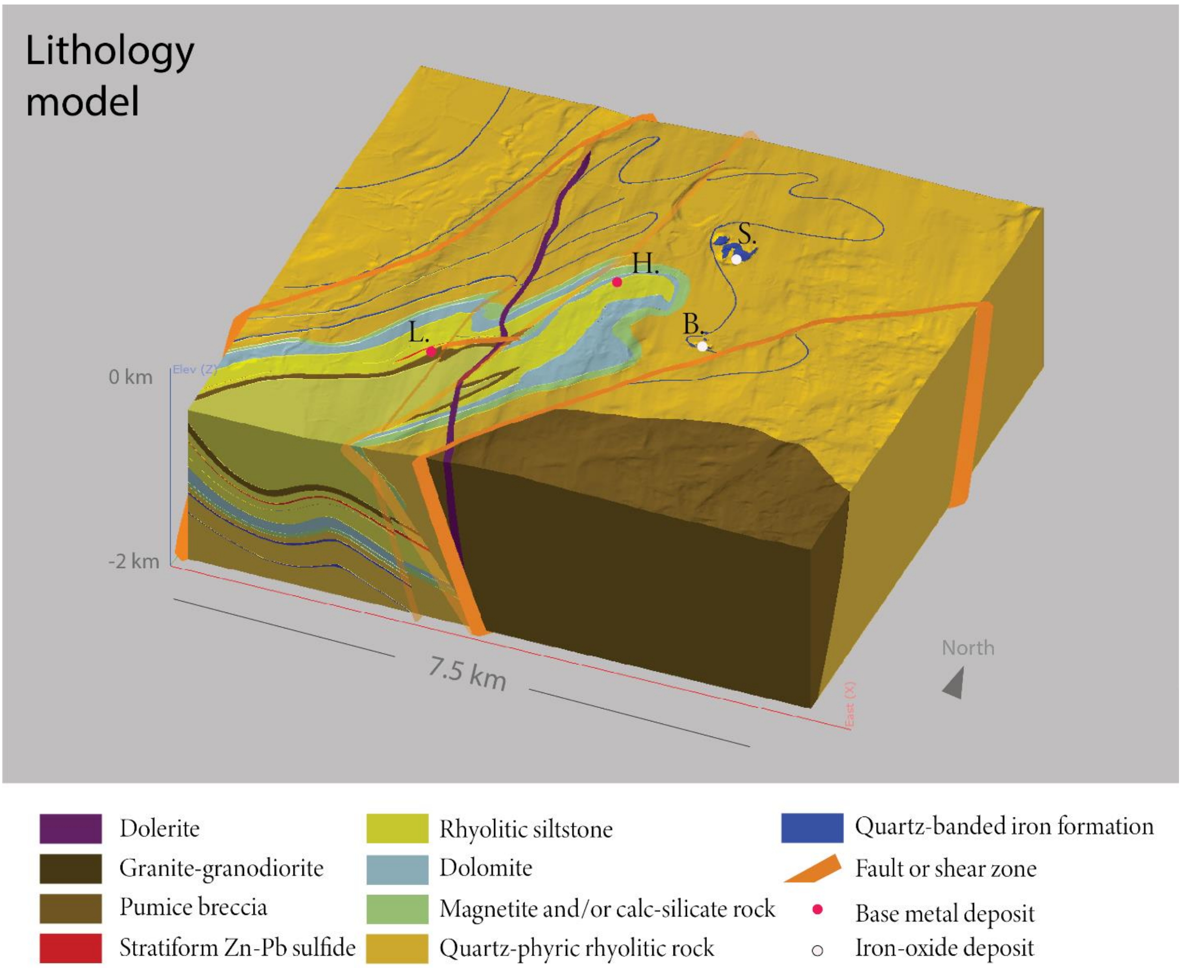

Figure 4.1.7. Semi-regional 3D lithology model and major shear zones. L: Lovisa Zn-Pb deposit, H: Håkansboda sulphide deposit, S: Stråssa Fe-oxides deposit, B: Blanka Fe-oxides deposit.

4.1.5.5 Deposit-scale models

The models reveal a distinctive outline for each deposit (Fig. 4.1.8). The Lovisa Zn-Pb-Ag ore body was modelled as a single tabular orebody including the "Main ore", "Sphalerite ore" and interlayers of barren rocks. The ore body has a thickness of 1 to 10 meters and is gently folded around a fold axis plunging 50° to the south east. The orebody is dismembered by the steeply east-dipping Lovisa shear and the southeast-dipping Central shear (Fig. 4.1.6a). The former accommodated a reverse-dextral displacement of the orebody of approximately 20 to 40 meters. At Stråssa, two modelled iron orebodies represent a tight fold closures plunging 50° to the southeast reaching a maximum depth of 200 and 360 meters below the surface. The Blanka ore bodies are moderate to steeply plunging rods located on opposing fold limbs at shallow levels but appear to merge into a single ore body below 240 meters below the surface. Modelling of the Håkansboda deposit shows several rod-shaped ore bodies that plunge steeply to the south-east reaching a depth of 200 meters below the surface. Despite the variation of the obtained geometries among the deposits, a typical feature of all deposits is their average plunge of 50° to 70° towards the south-southeast.

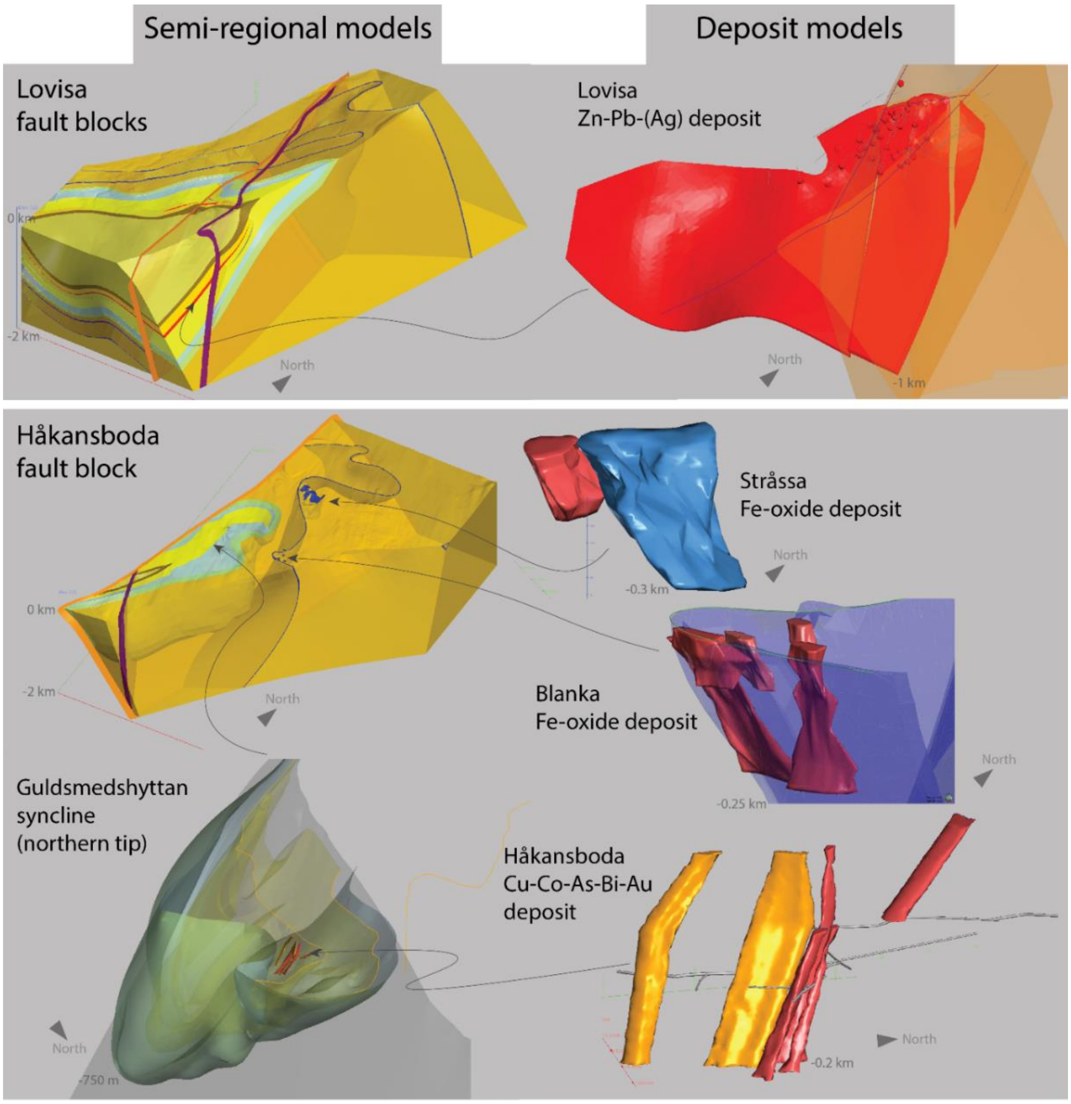

Figure 4.1.8. Geological models of the ore deposits at Loivsa, Stråssa, Blanka and Håkansboda and their regional setting. The Lovisa Zn-Pb-(Ag) deposit is modelled as a single layer with a thickness ranging between 1 and 10 meters including the “main-ore”, “sphalerite ore” and interlayers of barren rocks. The model is based on constraints from drilling (red circles) and in-mine observations and uncertainties are high outside the drilled regions (blue color). The orebody is dismembered by the steeply east-dipping Lovisa shear and the south-east-dipping Central shear (not displayed but see fig. 4.5a). The Stråssa and Blanka iron orebodies are associated with folding and thickening of a BIF-layer occurring throughout the region. Also, at Håkansboda, the steep plunge of the rod-shaped orebodies is in line with the regional-scale folding pattern at the northern tip of the Guldsmedshyttan syncline. Different coloring of the individual ore bodies has no geological meaning.

4.1.6 Geophysical modelling

4.1.6.1 Geophysical data and Petrophysics

The area of interest at the Lovisa mine has been surveyed by several airborne geophysical campaigns where various geophysical data set have been acquired. A summary of those campaigns can be found in X-Mine Deliverable 1.1. The most recent geophysical airborne survey over the Lovisa mine area was conducted in 2017. Figure 4.1.9 shows the magnetic anomaly field, expressed as the difference between the total magnetic field and an upward continuation to 1 km, acquired in that survey.

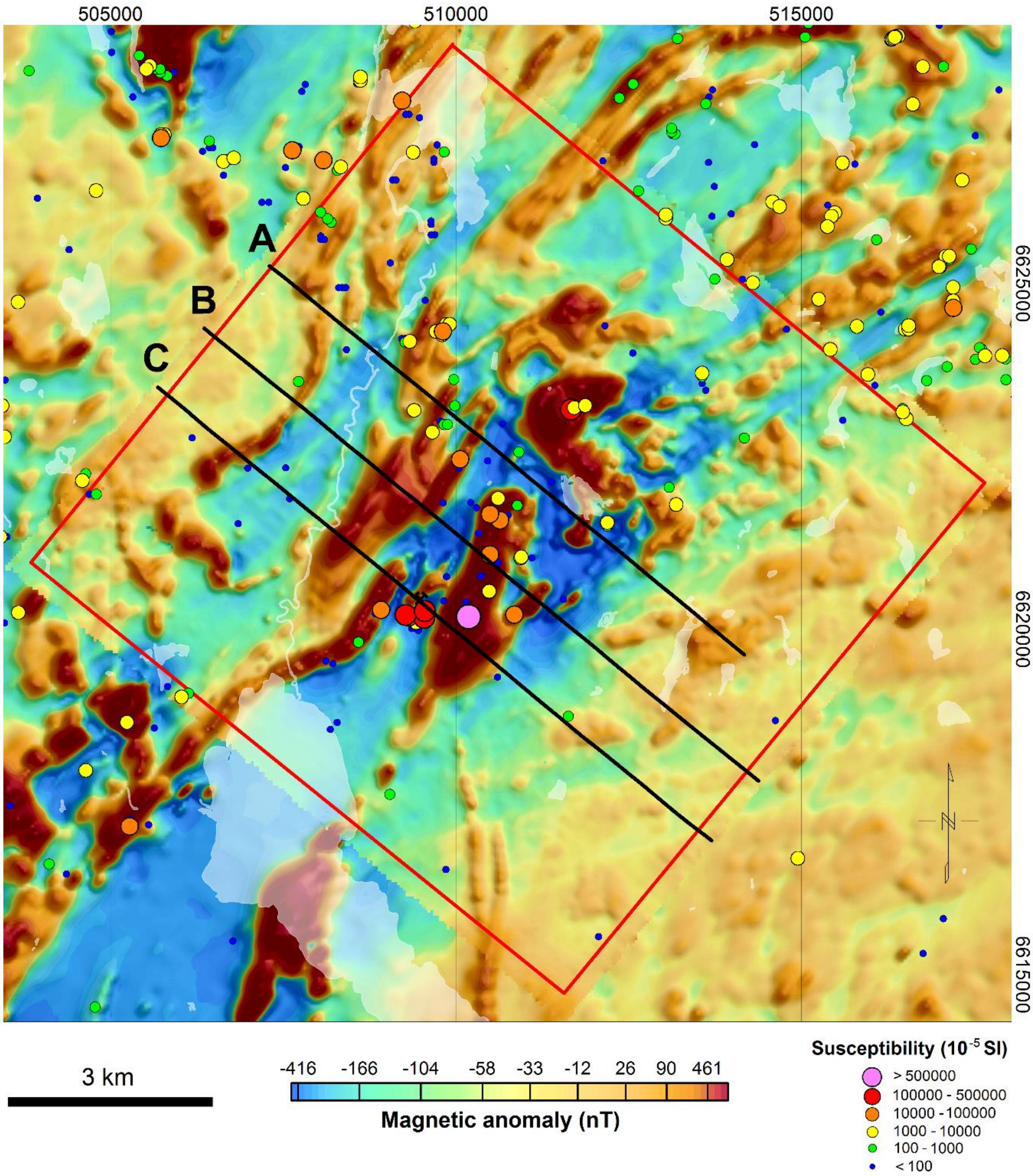

Figure 4.1.9. Magnetic anomaly map over the Lovisa mine area. The study area is shown with a red rectangle. The circles of different colors and sizes represent the susceptibilities of acquired petrophysical samples. The black lines labelled A, B, and C correspond to the modelled 2D cross-sections using magnetic and gravity data.

In 2017, a ground gravity campaign was also conducted, which densified the existing data set. Figure 4.1.10 shows the residual gravity field, expressed as the difference between the Bouguer anomaly and an upward continuation to 3 km.

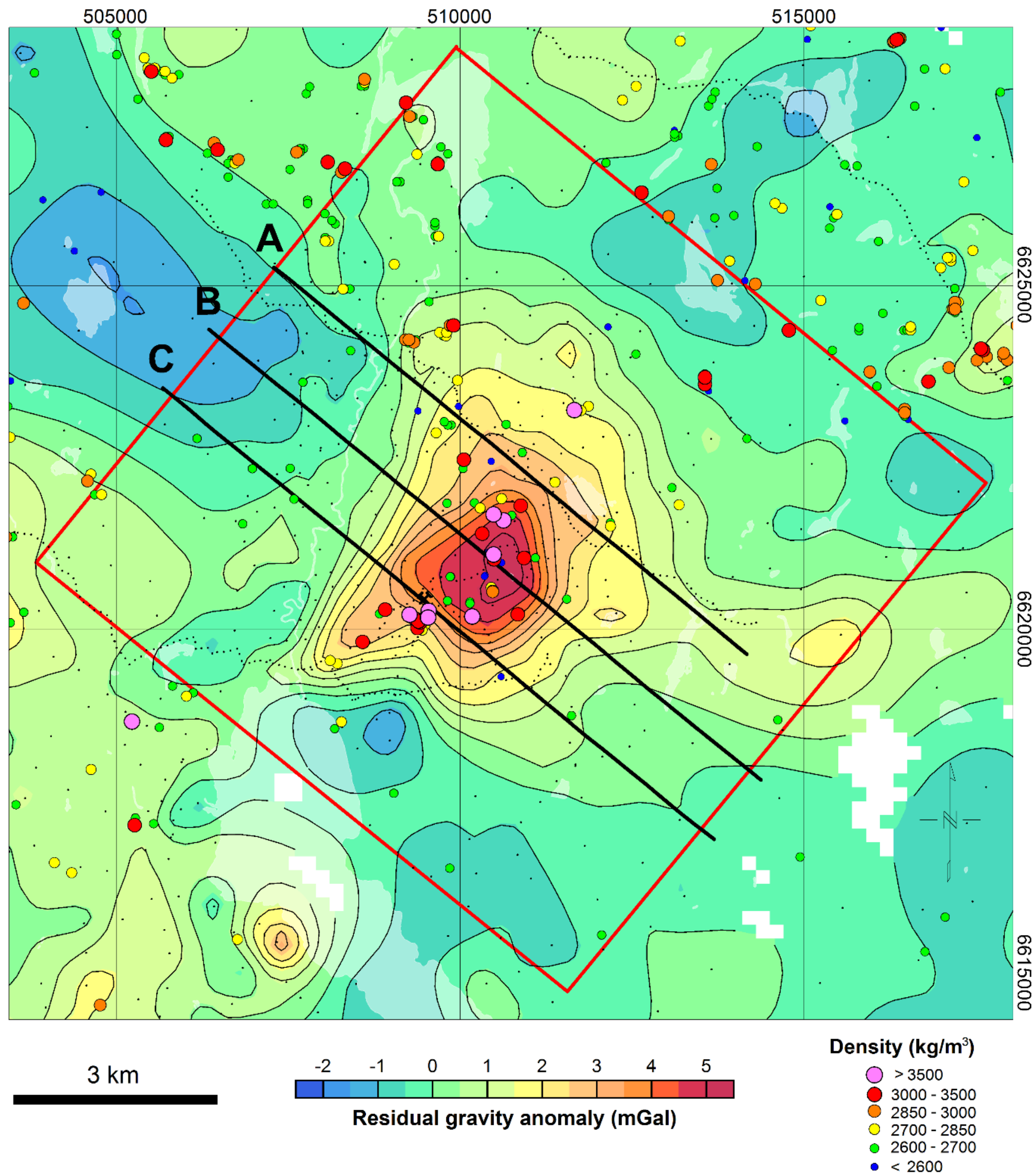

Figure 4.1.10. Residual gravity anomaly map over the Lovisa mine area and surroundings. Black dots show the location of gravity measurements. The study area is shown with a red rectangle. The circles of different colors and sizes represent the densities of acquired petrophysical samples. The black lines labelled A, B, and C correspond to the modelled 2D cross-sections using magnetic and gravity data.

The study area consists predominantly of felsic volcanic rhyolitic rocks with low densities, which are mostly associated with gravity lows on the gravity anomaly map (Fig. 4.1.9). Some of the gravity lows are also underlain by granites and pegmatites, particularly in the south. A pronounced gravity high exist in the center of the study are coinciding to a large extent with the Håkansboda dolomite. The strongest magnetic anomalies in the area are related to magnetite skarns, banded iron formations (BIF's) and iron-oxides mineralizations at Stråssa and Blanka (Fig. 4.1.8). The content of magnetite or other magnetic minerals in the felsic volcanic rocks is generally low but can be high locally (Table 4.1.1).

In the study area, the physical properties of 386 samples have been analyzed (Table 4.1.1 and Fig. 4.1.11). The samples were taken largely from outcrops, but 62 samples originate from drill core or underground exposures in the Lovisa mine. Table 1 shows the measured petrophysical properties for each rock type. Figure 4.1.11 shows graphically the distribution of densities and magnetic susceptibilities within each of these rock types.

Table 4.1.1. Density and magnetic properties for the dominating rock types within the area of interest, including the mineralizations. The table contains data from both previously acquired petrophysical data as well as those acquired within the X-Mine project. Densities are given in kg/m^3 and susceptibilities in 10^{-5} SI.

Rock type	Number of samples	Density (mean)	Density (std dev)	Susceptibility (min)	Susceptibility (max)	Susceptibility (median)
Basalt-andesite	10	3 046	170	65	93 300	6 020
Dolerite	15	2 874	41	200	3 400	2 900
Dolomite	22	2 837	69	1	8 900	60
Gabbro-diorite	36	2 996	75	56	18 300	350
Granite	22	2 627	35	3	2 900	30
Granodiorite-tonalite	8	2 789	52	68	4 290	800
Iron mineralization	6	3 893	180	8 600	733 400	148 500
Pegmatite	14	2619	40	1	285	6
Rhyolite-dacite	205	2 669	47	1	10 650	35
Sandstone-siltstone	27	2 620	61	3	30	13
Schist	6	2 741	133	5	880	30
Skarn	10	3 233	171	20	59 900	440
Sulphide mineralization	5	3 643	373	120	471 600	51 500

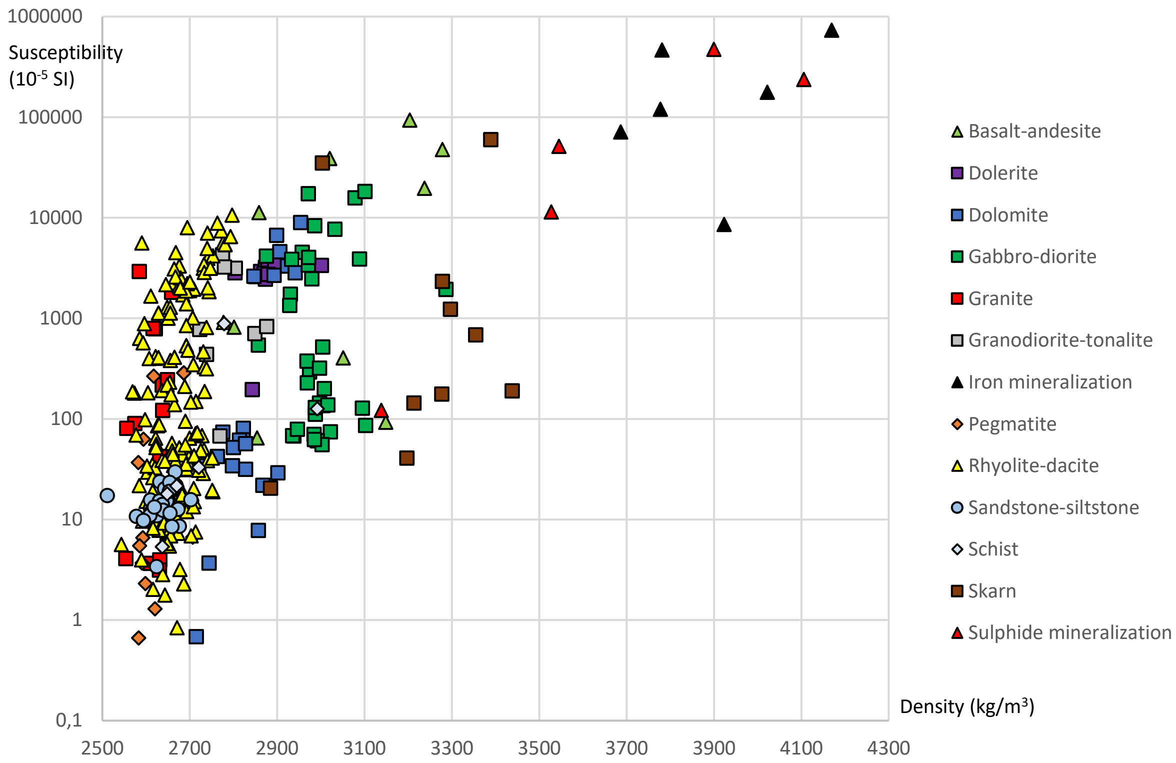

Figure 4.1.11. Petrophysical properties of the most common rock types in the Lovisa mine area. Magnetic susceptibility vs density. The total number of measured petrophysical samples is 386.

4.1.6.2 Methodology geophysical modelling

Geophysical models of the study area have been constructed both as three-dimensional inversions of magnetic data and as two-dimensional forward models by combining gravity and magnetic data. The three-dimensional models have been generated with the *Voxi* module in the *Geosoft Montaj* software. The two-dimensional forward models were created using the software *Potent*. Petrophysical data has been used to constrain the models by assigning each rock type the measured values for its density and magnetic susceptibility. The obtained values from samples located directly along the 2D sections were used for that specific lithology, rather than a mean value.

4.1.6.3 Results geophysical modelling

Profile A

The extent of the northern profile is labelled "A" in Figures 4.1.9 and 4.1.10, and it traverses the northern end of the Guldsmedshyttan syncline. There has been dense gravity measurement with approximately 100 m station spacing in the absolute vicinity of this profile.

These gravity measurements, along with magnetic data from a flight line, have been used as input data for constructing the interpreted geological model in Figure 4.1.12.

The felsic volcanic rocks along the profile are represented by yellow bodies. Red bodies represent granites and dark green bodies at the southeastern end of the profile are gabbros/diorites. The thin, purple body at 2 500 m along the horizontal axis represents dolerite, which has been assigned a density of 2 900 kg/m^3 and the magnetic susceptibility 3 000 x 10^{-5} SI. The central part of the profile crosses the dolomite (blue bodies), which is exposed at the surface at two locations close to the northern tip of the syncline.

The density and magnetic susceptibility of the dolomite have been set to 2 850 kg/m^3 and 60 x 10^{-5} SI, respectively. Felsic volcanic rocks or siltstones surrounds the dolomite. These rocks which surround the dolomite are less dense, which also is stated in table 4.1.1. The density of the shallow felsic volcanic rocks that overlay the dolomite have been set to 2 670 kg/m^3 and their magnetic susceptibility has been specified to 100 x 10^{-5} SI. The felsic volcanic siltstone (dark yellow body in Figure 4.1.7) that overlay the dolomite at 4 750 m along the horizontal axis has been assigned a density of 2 620 kg/m^3 and the magnetic susceptibility 10 x 10^{-5} SI. Since the density of the dolomite is significantly higher than the rocks surrounding it, the positive gravity anomaly in the central part of the profile indicate that the dolomite has a greater lateral extent in the subsurface than is visible at the surface. The depth extent of the dolomite is approximately 600 – 1000 m below the surface to satisfy the gravity anomaly.

Several deformation zones have been interpreted along the lateral extent of the dolomite, which offset the rock. One of these zones is the Engvall fault, which reaches the surface at 4200 m along the horizontal axis. At the borders of the dolomite there are magnetized horizons (green bodies in Figure 4.1.5). Calcite-banded iron horizons are present at 4500 m and 5000 m along the horizontal axis (Jansson et.al, 2018) whom generate positive magnetic anomalies. Stronger magnetic anomalies are present at 3200 m, 3800 m and 5800 m. The cause of these anomalies are quartz-banded iron formations (Jansson et.al., 2018), which have been assigned a density of 3 900 kg/m^3 and the magnetic susceptibility 1.5 SI in the interpretation model. These horizons are generally thin, approximately around 10 m, with a depth extent of around 100 m. The dip of these horizons is towards southeast. The strongest anomaly along the profile is the one at 5800 m, where the Blanka mine is situated. According to the interpreted geological model, the lateral extent of that body is 30 m with a depth extent of 500 m.

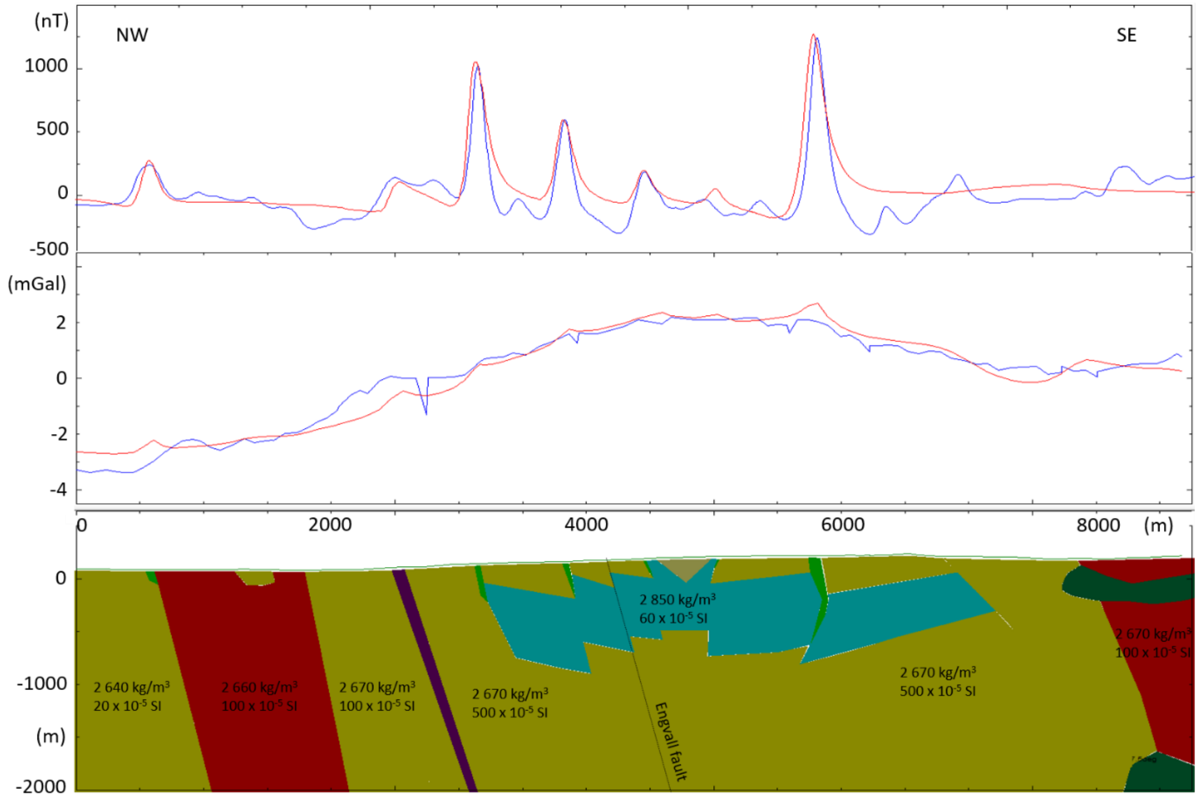

Figure 4.1.12. Forward model of profile A based on geophysical and petrophysical data. The cross-section is displayed from northwest (left side) to southeast (right side). The lateral extent of the profile is shown in Figures 1-2. Upper: variations in the magnetic field. Middle: the gravity field. Blue lines in these boxes are observed data; red lines are the response from the model.

Profile B

The extent of the middle profile is labelled "B" in Figures 4.1.9 and 4.1.10, and it traverses the central part of the area of interest. Gravity data has been extracted from an interpolated grid along a profile, along with magnetic data from a flight line. These data have been used as input data for constructing the interpreted geological model in Figure 4.1.13.

The felsic volcanic rocks along the profile are represented by yellow bodies and the red bodies represent granites. The thin, purple body at 3 300 m along the horizontal axis represents dolerite, which has been assigned the same petrophysical properties as the dolerite body in Figure 4.1.7, which are a density of 2 900 kg/m^3 and the magnetic susceptibility 3 000 x 10^{-5} SI. The felsic volcanic rock just southeast of the dolerite (at 3 700 m along the horizontal axis) has been assigned a magnetic susceptibility of 3 000 x 10^{-5} SI because petrophysical samples which have been acquired from this rock have a higher content of magnetite. The magnetic field is also showing an increase in amplitude over this area.

The central part of the profile crosses the dolomite (blue bodies), which is exposed at the surface at 4 200 m, and between 5 500 – 6 000 m. The density and magnetic susceptibility of the dolomite have been set to 2 850 kg/m^3 and 60 x 10^{-5} SI, respectively. Felsic volcanic siltstone (dark yellow bodies in Figure 4.1.7) overlays the dolomite. The density of the shallow felsic volcanic siltstone that overlay the dolomite have been set to 2 620 kg/m^3, and its magnetic susceptibility has been specified to 10 x 10^{-5} SI, which is according to the statistics in table 4.1.1. Within the siltstones, there is a highly magnetic and high-density layer of iron-mineralization (green body in Figure 4.1.7). The layer has a synclinal shape with an overall dip to the southeast. This layer clearly stans out in the magnetic data, where a strong, positive anomaly is present at 5 250 m along the horizontal axis. By assigning this layer the density and magnetic property which is presented in table 1 for iron-mineralizations (3 900 kg/m^3 and 1.5 SI, respectively), the width of the layer is 35 m and its depth extent is almost 200 m to satisfy the magnetic anomaly. There are other, weaker positive magnetic anomalies present along the profile. Two of these anomalies are present at 4 200 m and 6 200 m, which probably are caused by calcite-banded iron formations (green bodies in Figure 4.1.7). In the model, these formations are situated at the border of the dolomite and are following its rim at the subsurface, creating a synclinal.

There is a pronounced positive gravity anomaly where the dolomite is present. The anomaly is caused by the dolomite together with the high-density magnetite rich layers that either overlays it or surrounds it. The depth extent of the dolomite and the calcite-banded iron formation is 1 400 – 1 600 m to satisfy the positive gravity anomaly. Along this profile, one deformation zone has been interpreted, which offset the rock. This is the Engvall fault, which reaches the surface at 4 600 m along the horizontal axis.

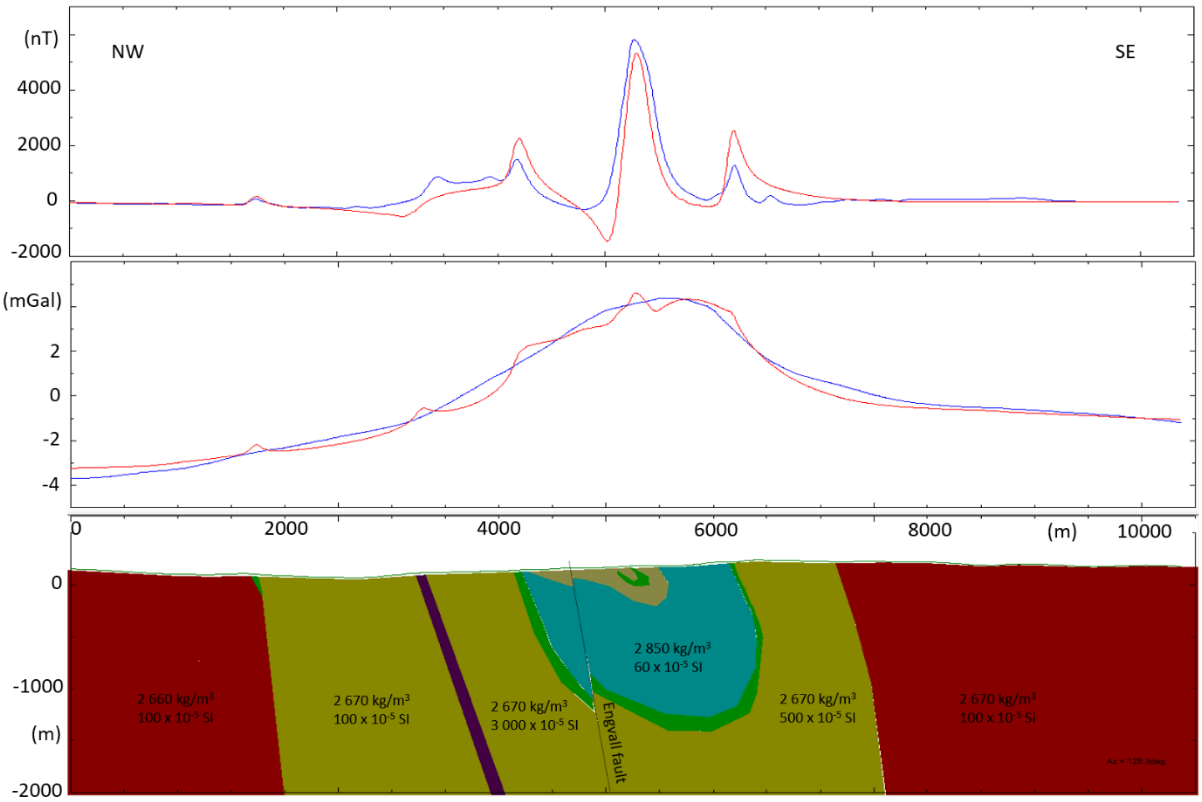

Figure 4.1.13. Forward model of profile B based on geophysical and petrophysical data. The cross-section is displayed from northwest (left side) to southeast (right side). The lateral extent of the profile is shown in Figures 1-2. Upper: variations in the magnetic field. Middle: the gravity field. Blue lines in these boxes are observed data; red lines are the response from the model.

Profile C

The extent of the southern profile is labelled “C” in Figures 4.1.9 and 4.1.10, and it traverses the Lovisa mine area together with the surroundings. Gravity data has been extracted from an interpolated grid along a profile, along with magnetic data from a flight line. These data have been used as input data for constructing the interpreted geological model in Figure 4.1.14. The detailed geological cross section that is available in Jansson et.al (2018) has also been used to further constrain the distribution of rock types between 4 500 – 5 500 m along the horizontal axis and down to 500 m below the surface.

The felsic volcanic rocks along the profile are represented by yellow bodies and the red bodies represent granites. The thin, purple body at 5 100 m along the horizontal axis represents dolerite, which has been assigned a density of 2 900 kg/m^3 and the magnetic susceptibility 3 000 x 10^{-5} SI. The location of the dolomite also coincides with the Engvall fault, which offsets the rock units on either side. The central part of the profile crosses the dolomite (blue bodies), which is exposed at 4 000 m and 6 000 m along the horizontal axis.

The density and magnetic susceptibility of the dolomite have been set to 2 850 kg/m^3 and 60 x 10^{-5} SI, respectively. Felsic volcanic rocks or siltstones surrounds the dolomite, along with magnetite rich layers (green bodies in Figure 4.1.7). The density of the shallow felsic volcanic rocks or siltstones that overlay the dolomite have been set to 2 620 kg/m^3. Their magnetic susceptibility has been specified to 10 x 10^{-5} SI. On the southeastern side of the dolomite, the magnetite rich layers have been assigned those petrophysical properties which are given in table 4.1.1 for iron mineralizations, which is a density of 3 900 kg/m^3 and the magnetic susceptibility of 1.5 SI. To fit both the gravity and the magnetic field on this side of the dolerite, the width of the magnetite-rich layers is around 30 – 40 m. One of these layers follow the border of the dolomite down to 900 m below the ground surface. Southeast of the dolerite, layers of dolomite, felsic volcanic siltstones and magnetite skarn are folded into a southeast dipping syncline. Northwest of the dolerite, the iron rich layers have been interpreted as less rich in magnetite than further toward the southeast due to the relatively low magnetic anomalies they produce. For this reason, they have been assigned a density of 3 200 kg/m^3 and the magnetic susceptibility 0.5 SI. The dolomite which is present at the surface at 4 000 m along the horizontal axis, has a southeastern dip and thickens at depth to satisfy the positive gravity anomaly. The dolomite reaches a depth of 1 300 m near the Engvall fault.

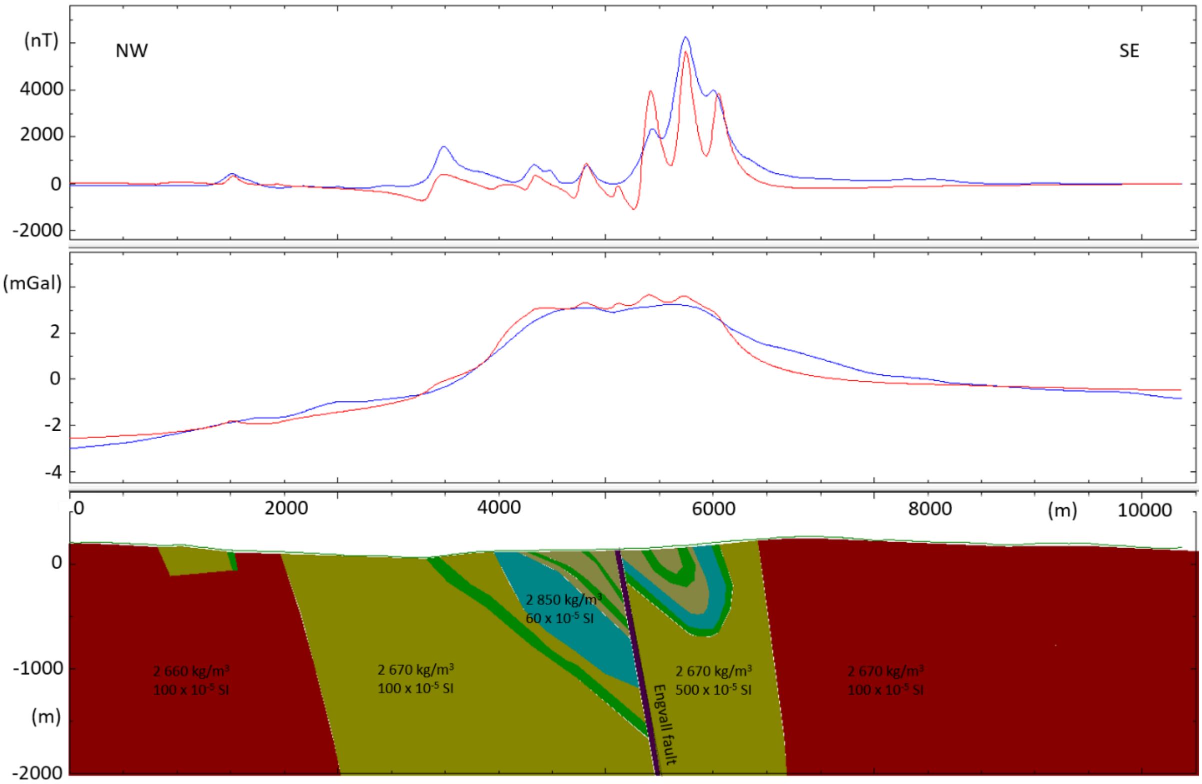

Figure 4.1.14. Forward model of profile C based on geophysical and petrophysical data. The cross-section is displayed from northwest (left side) to southeast (right side). The lateral extent of the profile is shown in Figures 1-2. Upper: variations in the magnetic field. Middle: the gravity field. Blue lines in these boxes are observed data; red lines are the response from the model.

4.1.7 Discussion and implications

4.1.7.1 Comparison between geological- and geophysical modelling results

A great strength of 3D geomodelling is using the variety of interpretation, modelling and inversion techniques based on geological-, geochemical- and geophysical datasets. For this study, geological- and geophysical modelling was conducted independently and a better integration between both is aimed for during the ongoing investigations within the X-Mine project (see following section). However, at this stage a first comparison between the results obtained using different modelling techniques can already be made and a short description summarizing the main outstanding features observed in figs. 4.1.15 to 4.1.18 is provided below.

To compare the semi-regional geological model with the results from the 2D forward model and the unconstrained 3D inversion of magnetic data, three sections are displayed for each model located along the same profile lines as for the 2D forward models presented in the previous section (see Figs. 4.1.9 and Figs. 4.1.15 to 4.1.18).

At profile A (Fig. 4.1.15), the most outstanding feature is the relatively large, flat-lying volume of dolomite in the center of the 2D forward model. Based on observations on only a few outcrops and structural measurements, the geological model shows here a simple syncline reaching depth not beyond a few tens of meters below the surface. It should be stated that this area is very poorly exposed, and no drilling has been conducted that can confirm dolomite in the subsurface. On the other hand, the solution of the 2D forward model is not unique and the relatively high gravity anomaly coinciding with a magnetic low in this area may be caused by other lithologies as well. The 3D magnetic inversion along the same line displays three moderate- to steeply plunging, high-magnetic bodies near the surface of which the most eastern one coincides with the Blanka deposit. Here, the Blanka deposit appears as an antiform. To the west of Blanka, a large synform may be interpreted based on a volume of relatively high magnetic rocks below a low magnetic rocks of which the base reaches a depth of 1200 m below the surface. The relatively high magnetic rocks may well represent banded iron formations but whether the low magnetic domain represents rhyolitic rocks or dolomite remains very uncertain at this stage. Along profile "B", both the geological- and the forward model display a steeply southeast dipping syncline in the center of the area (Guldsmedshyttan syncline) (Fig. 4.1.16). The dolomite is significantly thicker in the forward model (*c*. 750 m) with respect to the geological model (*c*. 400 m). In addition, highly magnetic skarn layers seem to appear both below and above the dolomite in the forward model. In the geological model, the skarn stratigraphically above the dolomite has been modelled as separate lenses and therefore does not appear on this section. The 3D magnetic inversion along profile B shows a large volume of highly magnetic material extending far beyond 2 km in depth. At the surface, this magnetic volume coincides with a banded iron formation in the west and more towards the center of the profile with skarn and the Håkansboda deposit. At depth, the thickness and diffuse character of the high-magnetic domain, however, makes a comparison with the other models very uncertain and more constraints are needed. In profile C, the geological- and the forward model both display a steeply southeast dipping syncline (Guldsmedshyttan syncline), of which its northwestern limb has been displaced by the Engvall fault in a reverse-sense (Fig. 4.1.17). The dolomite unit west of the fault appears at least three times as thick in the forward model (*c.* 350 m) compared to the geological model (*c.* 100 m). The 3D magnetic inversion shows a large, steeply west dipping synform of a volume of high magnetic susceptibility enclosing a low magnetic volume. The overall geometries interpreted from this model strongly contrast with the structural pattern observed in the geological- and forward model. Providing better constraints to the 3D magnetic inversion may help to achieve consistency with the geological- and 2D forward model.

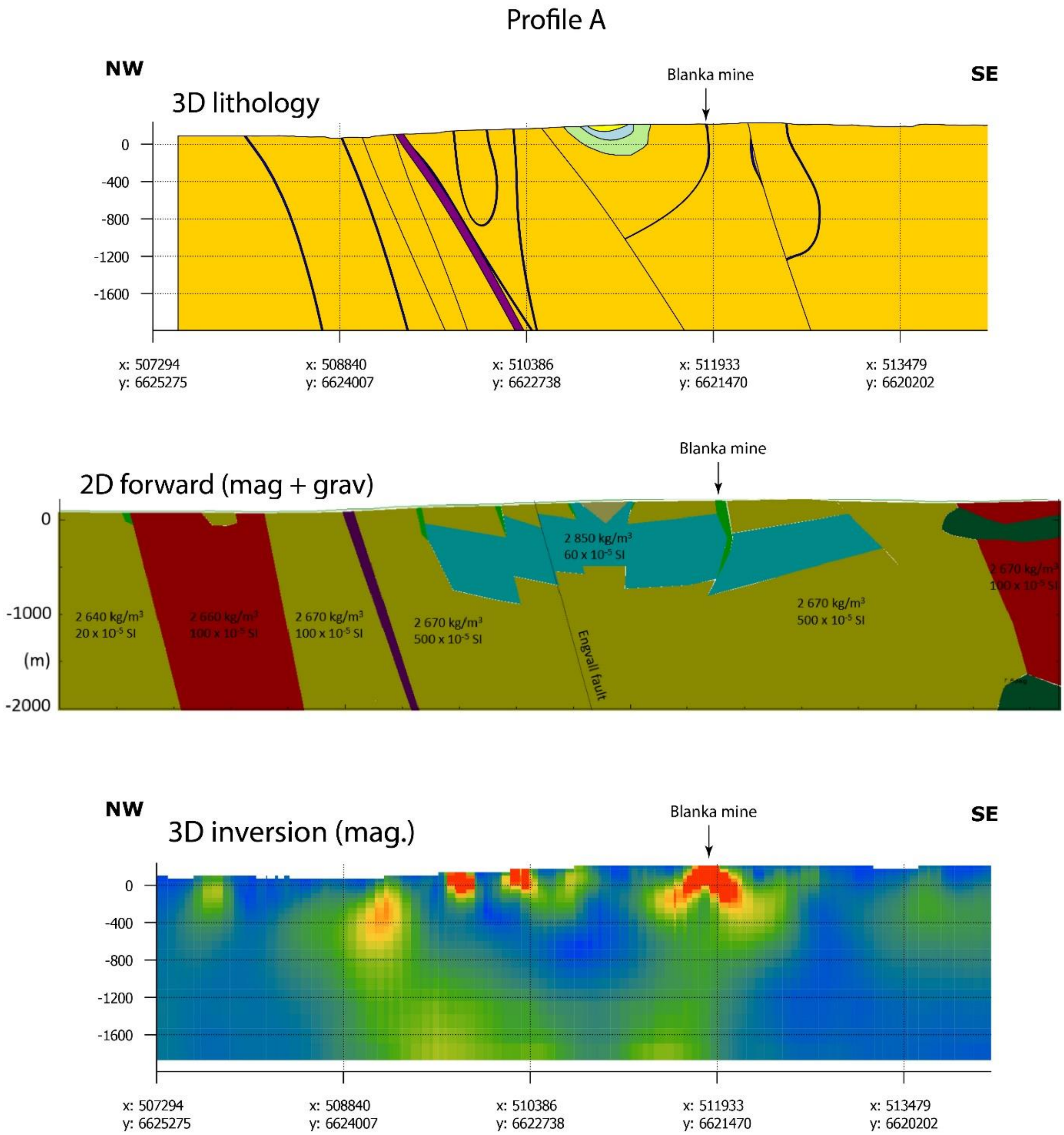

Figure 4.1.15. 2D cross-sections along “A” to compare the results from the geological model (top), forward model (center) and the 3D magnetic inversion (below). The most outstanding difference is the large volume of relatively flat-lying dolomite in the subsurface (center) compared to the minor syncline in the geological model. The 3D inversions show moderate- to steeply plunging high magnetic bodies (red color) near the surface of which the most eastern one coincides with the Blanka deposit appearing as an antiform. A larger synform may be interpreted directly west of Blanka but is highly uncertain. Legend of the geological profile in Fig. 4.1.3. Legend of 2D forward model in figure caption of Fig. 4.1.12. Red and blue colors in the 3D inversion corresponds to relatively high and low magnetic, respectively.

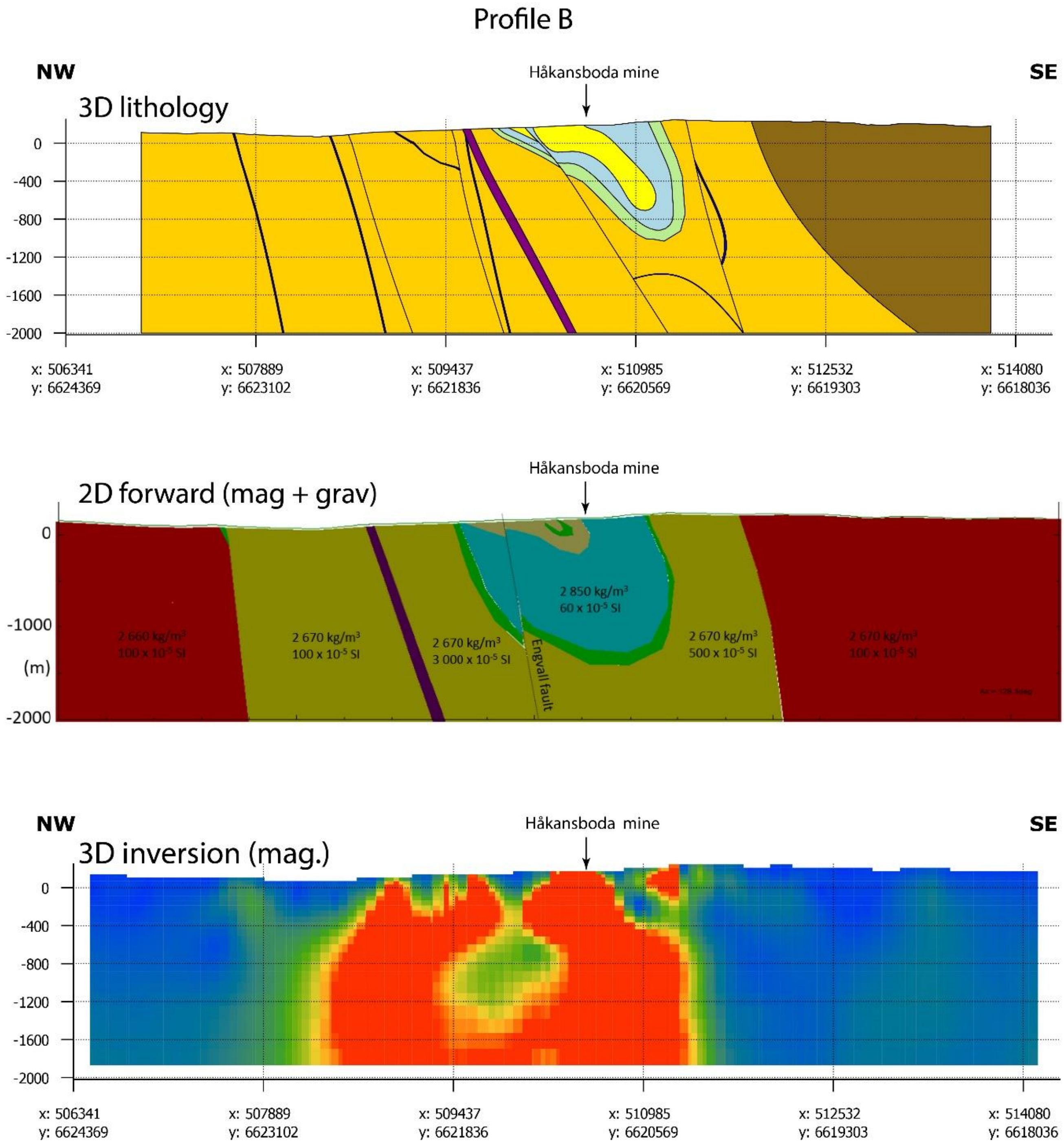

Figure 4.1.16. 2D cross-sections along “B” to compare the results from the geological model (top), forward model (center) and the 3D magnetic inversion (below). Both the geological- and the forward model display a steeply southeast dipping syncline in the center of the area (Guldsmedshyttan syncline). The dolomite is significantly thicker in the forward model with respect to the geological model. The 3D inversion, on the other hand, reveals a large volume of high magnetic material extending far beyond 2 km in depth. Is not clear to which geological unit the high magnetic volume relates to. Legend of the geological profile in Fig. 4.2b. Legend of 2D forward model in figure caption of Fig. 4.12. Red and blue colors in the 3D inversion corresponds to relatively high and low magnetic, respectively.

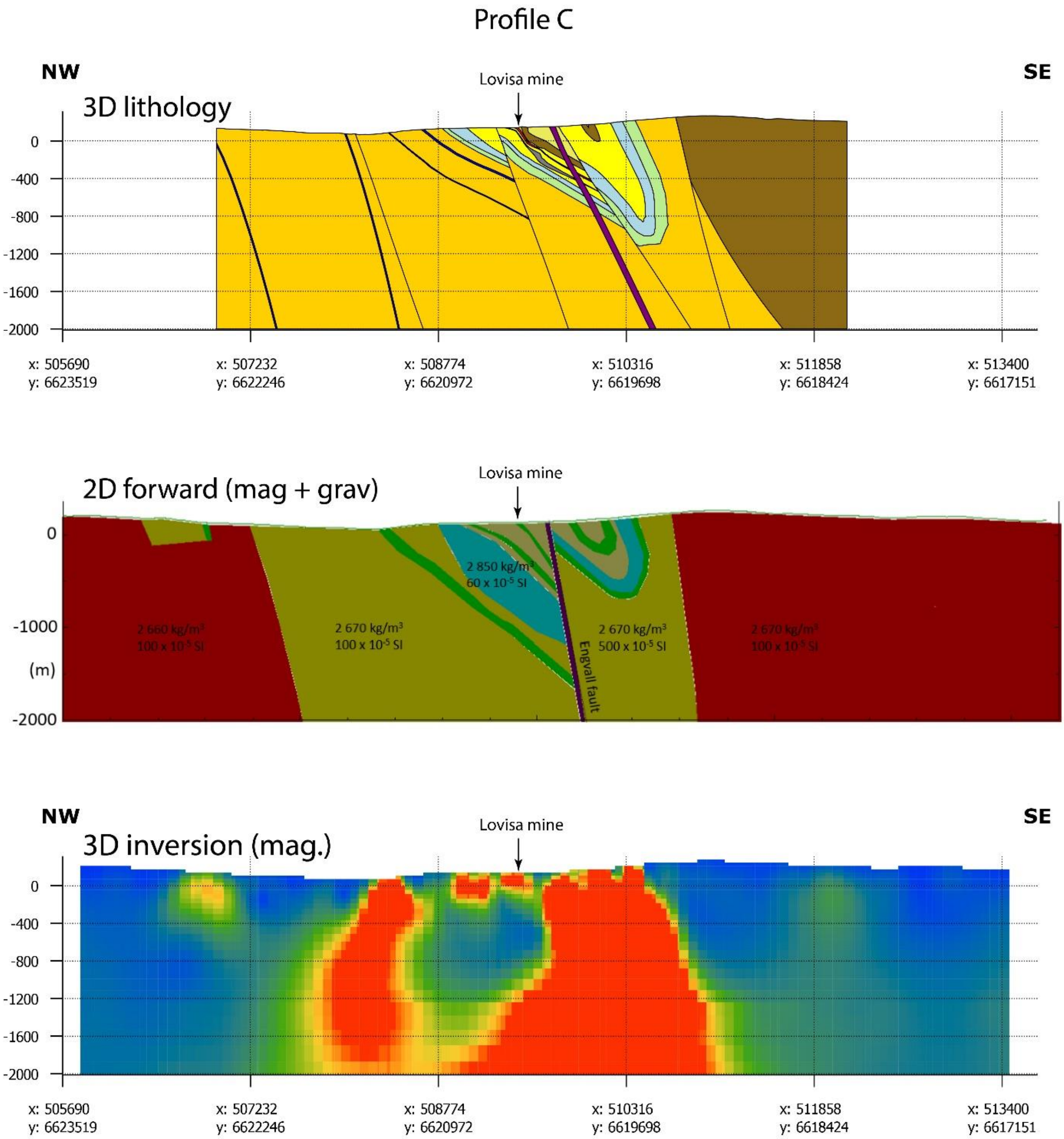

Figure 4.1.17. 2D cross-sections along "C" (see Fig. 4.8) to compare the results from the geological model (top), forward model (center) and the 3D magnetic inversion (below). Both the geological- and the forward model display a steeply southeast dipping syncline (Guldsmedshyttan syncline), of which its northwestern limb has been displaced by the Engvall fault in a reverse-sense. The dolomite unit west of the fault appears at least three times as thick in the forward model compared to the geological model. The 3D magnetic inversion shows a large, steeply westward dipping synform of a volume of high magnetic susceptibility enclosing a low magnetic volume. Providing better constraints to the inversion should help to confirm such an interpretation. Legend of the geological profile in Fig. 4.2b. Legend of 2D forward model in figure caption of Fig. 4.1.14. Red and blue colors in the 3D inversion corresponds to relatively high and low magnetic, respectively.

On a deposit-scale, a combined visualization of the Stråssa and Blanka iron-oxides geological models and highly magnetic volumes obtained from the 3D magnetic inversion is shown in figure 4.1.18. In general, the magnetic domains coincide well with the ore bodies, however, some of the ore bodies at Blanka are not included. At Stråssa, the relatively large volume of highly magnetic material may imply (but not necessarily!) the existence of iron ore further down to a depth of approximately 1 km below the surface. Likewise, the high magnetic body directly northeast of Stråssa may indicate that there is more iron mineralization left than has been mined so far.

4.1.7.2 Structural framework, regional tectonics and comparison with other deposits in Bergslagen

The Guldsmedshyttan syncline is the dominant regional structure, which is mostly NE-SW trending, steeply inclined, isoclinal and doubly plunging and locally overturned. In the Lovisa-Håkansboda mining area the syncline is refolded along its northern tip (hook-shape) and is dismembered by predominantly NE to N trending shear zones and faults. The syncline's western fold limb comprises besides the relatively low magnetic metavolcanics rocks and carbonates, highly magnetic quartz banded iron formations and iron skarn horizons. These iron ore bearing layers stand out on the magnetic anomaly map and are often well traceable over long distances. Due to the high resolution of a recent airborne magnetic survey (100 meters flight line spacing at 60 meters ground clearance) a complex folding pattern has been identified. Additional field observations (e.g. structural measurements and strain indicators in outcrops and thin-sections) reveal that many macroscopic folds are doubly plunging (locally even sheet folds) and fold a pre-exiting penetrative foliation (S1). The F2 folds are sheared and boudinaged vertically as well as elongated in an NE-SW direction parallel to the main trend of the Guldsmedshyttan syncline. The limbs are locally refolded (F3) by open to isoclinal S- or Z-folds along steeply to moderately south to southeast plunging fold axes. In terms of tectonic events, the overprint between F2 and F3 folding may be explained by a stage of reverse-shearing and vertical extrusion during D2 (NW-SE directed shortening) followed up by a wrenching phase (D3) of predominantly sub-horizontal shearing in both a sinistral and dextral sense during regional N-S directed shortening. Despite the variation of the obtained geometries among the deposits, a typical feature of all deposits is their plunge of 50° to 70° towards the south-southeast. A similar structural trend is shown by the measured fold-axes and stretching lineations in the adjacent bedrock within the study area. Steeply plunging, rod-shaped ore bodies have been reported for several sulphide and iron-oxides ore deposits in the Bergslagen lithotectonic unit. (e.g. Kampmann et al. 2016). In line with Kampmann et al. (2016) we suggest that D_2 deformation of predominantly reverse shearing may have produced doubling plunging folds and cone to rod shaped ore bodies, most likely during a single deformation phase. Subsequently, strike-slip and horizontal shearing during D_3 may then have caused locally refolding and thickening of low-viscosity zones, such as carbonate and ore bearing layers.

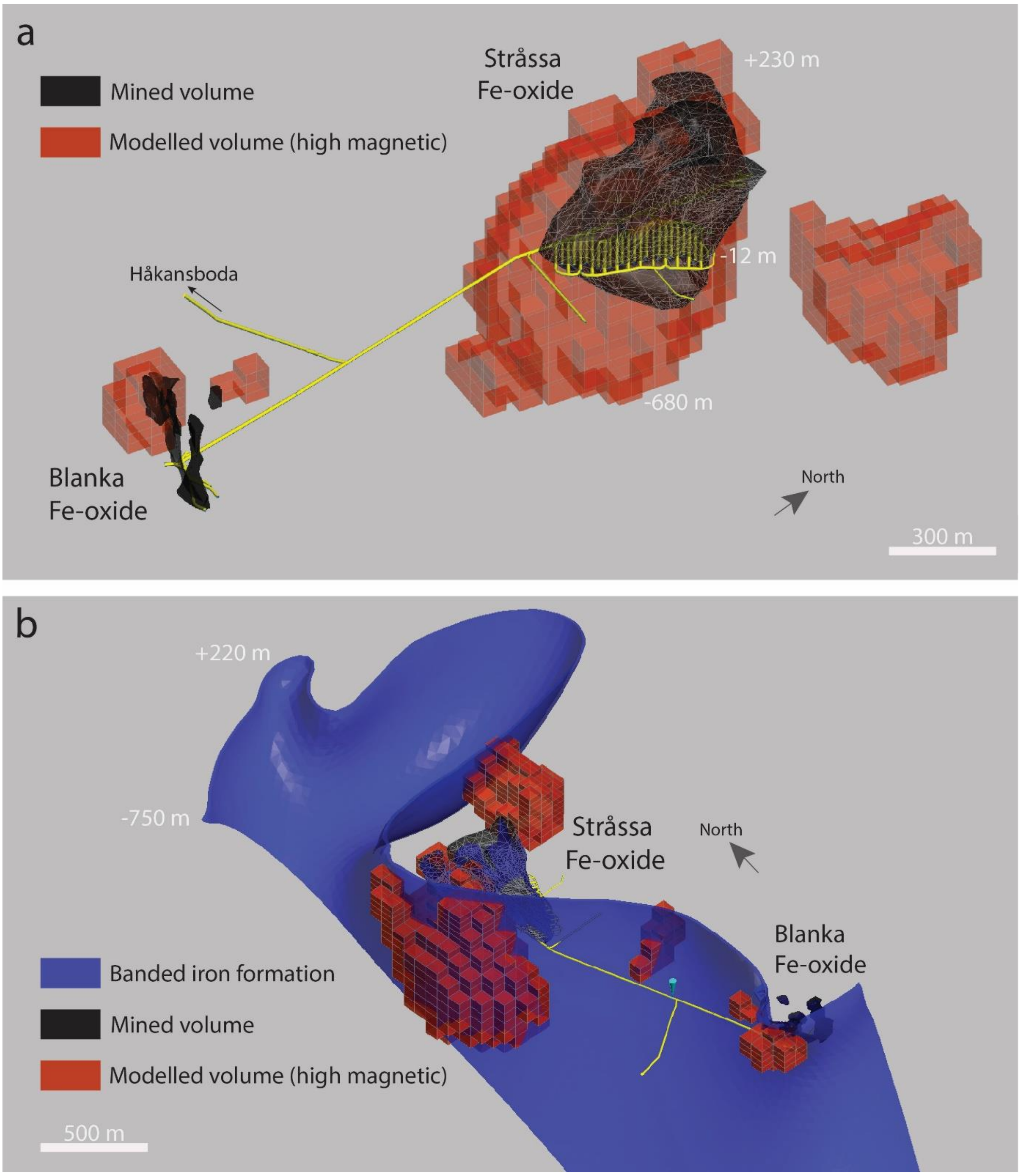

Fig. 4.1.18. Combined visualization of the Stråssa and Blanka iron-oxides deposit models and the high magnetic volumes obtained from the 3D magnetic inversion (red blocks). Notice the general coincidence between the deposits and the magnetic highs. The relatively large high magnetic volume at Stråssa may imply (but not necessarily) the existence of iron ore further down to a depth of approximately 1 km below the surface.

4.1.8 Conclusions and outlook

The presented geological- and geophysical models provide a good three-dimensional understanding on the shape and spatial distribution of the Lovisa, Håkansboda, Stråssa and Blanka ore bodies as well as on their regional geological framework (Guldsmedshyttan syncline). The modelled ore bodies reach between 38 and 1200 meters below the surface, but most bodies are likely to continue to greater depths according to interpretations from geophysical modelling (Stråssa) and drilling (Håkansboda). Despite the variation of the obtained geometries among the deposits, a typical feature of all deposits is their plunge of 50 to 70° towards the south-southeast, which is consistent with the plunge of measured stretching- and intersection lineations in the area. Hence, the shape the modelled ore bodies fit well with the regional D2 folding pattern and it can be inferred that: Regional structures exert a large control on the present shape of the orebodies (valid for both Fe-oxides and polymetallic sulfide mineralization). Mineralizations most likely pre-dates regional deformation during D2. However, deformation during D2 modified any pre-existing mineralization through remobilization, folding and thickening of ore-bearing layers. To continue modelling, more constraints from petrophysical properties are needed enabling a better integration between the geological- and geophysical modelling results and to reduce the non-uniqueness of the inversion process of potential field data (gravity and magnetics). Subsequently, orebody (in-mine) models will then be produced for each test site building heavily on data derived from XRF-XRT scanning on oriented core drilled within the X-Mine project.

References

Bleeker, W., 1984, Geology of the Stråssa-Torrsjöboda area and the Håkansboda-Ingelshyttan area, map sheets 11F 4c, 11F 4d, 11F 4e: Unpublished exploration report for Luossavaara-Kirunavaara Aktiebolag (LKAB) and British Petroleum (BP) AB Joint Venture, B85-12, 97 p., www.resource.sgu.se / dokument / geodigitalia / rapporter/ b_8512.pdf.

Carlon, C., Bleeker, W., 1988: The geology and structural setting of the Håkansboda Cu-Co-As-Sb-Bi-Au deposit and associated Pb- Zn-Cu-Ag-Sb mineralisation, Bergslagen, central Sweden. Geologie en Mijnbouw 67:272–292.

Jansson, N., Sädbom, S., Allen, R., Billström, K., Spry, PG., 2018: The Lovisa stratiform Zn-Pb deposit, Bergslagen, Sweden: structure, stratigraphy, and ore genesis. Economic Geology 113, 699-739.

Kampmann, T., Stephens, M., Weihed, P., 2016: 3D modelling and sheath folding at the Falun pyritic Zn-Pb-Cu (Au-Ag) sulphide deposit and implications for exploration in a 1.9 Ga ore district, Fennoscandian Shield, Sweden. Mineralium Deposita 51, 665–680.

Koark, H.J., 1960: The Geology of the Stråssa, Blanka and Håkansboda Districts. A brief outline on the occasion of the XXI International Geological Congress.

Kopparberg Mineral AB, 2012: The Håkansboda project, 54 pp Lovisagruvan AB annual report 2018. www.lovisagruvan.se.

Lundström, I., 1983: Beskrivning till Bergrundskartan. Lindesberg SV: Geological Survey of Sweden, Af 126, 140 p. (in Swedish).

Luth, S., Sahlström, F., Jansson, N., Jönberger, J., Sädbom, S., Landström, E., Bergqvist, M., Arvanitidis, N., Arvidsson, R. Building 3D geomodels using XRF-XRT-generated drill core data: The Lovisa-Håkansboda base metal- and Stråssa-Blanka iron deposits in Bergslagen, Sweden, SGA-extended Abstracts 2019.

Sahlström, F., Jonsson, E., Luth, S., Höghdahl, K., Landström, E., Sädbom, S., Lynch, E., Ghaderidosst, S., 2019: Textural evolution of the Lovisa Zn-Pb-(Ag) deposit, Bergslagen, Sweden: Insights from microscopy and 3D X-ray tomography, SGA-extended Abstracts 2019.

Stephens, M.B., Andersson, J., 2015: Migmatization related to mafic underplating and intra- or back-arc spreading above a subduction boundary in a 2.0–1.8 Ga accretionary orogen, Sweden. Precambrian Research 264, 235–257.

4.2 Assarel mining area in Bulgaria

4.2.1 Introduction

Three-dimensional (3D) geomodelling of the Assarel test site and surrounding area has been ongoing as part of Work Package 1 (WP1). This task has involved the compilation of relevant open source and mine-related geodata to develop new geological, structural and geochemical 3D models for Assarel. The integration of existing geological information with new data obtained from 3D drill core XRT-XRF analysis using X-Mine pilot scanning technologies is also a critical aspect of this work (see Section 4.2.3 below and additional reporting related to X-Mine Work Packages 4 and 5).

This chapter outlines the status of Assarel test site 3D geomodelling at the “near-mine” or “semi-regional” scale. An overview of the input data used to construct the near-mine model is firstly given. This information partly overlaps with the data compilation previously presented in X-Mine report D1.1 (2018). Subsequently, justification of the chosen model extent and preliminary modelling results are presented. Overall, it is envisaged that near-mine geomodelling will integrate seamlessly with new mine-scale modelling of the Assarel porphyry Cu-Au system. The within-mine or deposit-scale work will be summarised in future X-Mine report D1.3 (due in 2020) and will incorporate geodata acquired from X-Mine 3D drill core XRF-XRT pilot technology analysis on oriented drillcores (Work Packages 4 and 5).

4.2.2 Near-mine (semi-regional) 3D geomodelling

This section summarizes the data used to construct the Assarel 3D near-mine model and presents some preliminary results in the form of a new 3D fault system and lithology model. All geomodelling for this report utilized previous geological mapping (see Table 4.2.1 below) and was performed using a combination of ArcGIS Desktop and Leapfrog Geo (versions 10.5.1 and 4.4.2, respectively). On-going X-Mine-related work aims to refine and validate the preliminary near-mine modelling using new field mapping and drill core scanning results (see Section 4.X.3 below). It is also hoped that regional and within-mine geophysical data (magnetic and gravity field data from the Bulgarian Energy Ministry) will contribute to the future validation of the preliminary near-mine modelling presented here.

4.2.2.1 Input data and model extent

Input data for the Assarel near-mine model mainly comprises open source digital topographic data obtained from several sources (e.g. the USGS), and historical geological maps produced by the Bulgarian government and other academic organisations. Most of the geological mapping is relatively small-scale (> 1:50 000 or regional-scale) and only available in analogue format (i.e. paper maps). This information thus required digitizing (scanning) and georeferencing to the UTM grid system prior to modelling (discussed further below). Open source GIS vector topographic data from ESRI (e.g. town boundaries) were also incorporated to aid scanned image georeferencing, while additional vector data were digitized from the georeferenced geological and/or topographic maps (e.g. regional mineralization locations). A summary of the input data used for the modelling is listed in Table 4.2.1 below.

Table 4.2.1. List of data used for the Assarel near-mine 3D geomodelling
.

Dataset or map	**Format**[1]	**Spatial coverage**	**Reference**
ASTER ASTGTM digital elevation model (2009)	GeoTiff (*.tiff) grid file	Panagyurishte area (UTM 35T North)	NASA/METI (2009), Abrams et al. (2010)
1:100 000-scale topographic map	Georeferenced scanned paper map	Panagyurishte area	Bulgarian topographic mapping agency
Topographic vector data (various scales)	ESRI shapefile format	Bulgaria and Panagyurishte area	ESRI
1: 500 000-scale geological map of Bulgaria	MapInfo TAB format (converted to ESRI shapefile)	Bulgaria	Bulgarian Committee on Geology - Department of Prospecting and Geophysical Mapping (1989)
1:100 000-scale geological map	Georeferenced scanned paper map	Panagyurishte area	Iliev & Katckov (1990)
1:100 000-scale geological cross sections (x3)	Georeferenced scanned paper map	Panagyurishte area	Iliev & Katckov (1990)
Ca. 1:75 000-scale geological map	Georeferenced scanned paper map	Assarel-Medet mine area	Popov et al. (2012)
Ca. 1:75 000-scale geological map	Georeferenced scanned paper map	Krasen-Petelovo area	Popov et al. (2012)
Ca. 1:40 000-scale geological map	Georeferenced scanned paper map	Medet mine area	Strashimirov et al. (2003).

[1]Scanned maps georeferenced to UTM Zone 35T North with WGS 84 spheroid.

A key starting point for 3D geological modelling is access to a high-quality digital elevation model (DEM) derived from relevant elevation information. For the Assarel study area, Bulgarian-sourced digital elevation data with the desired spatial extent were not available (e.g. gridded DEM or contour vector data). Thus, the open source ASTER Global Digital Elevation Model (ASTGTM v.2.0; Abrams et al. 2010) obtained from the USGS *Earth Explorer* website (https://earthexplorer.usgs.gov/) was used as the base elevation layer for the Assarel near-mine 3D modelling (Figs. 4.2.1 and 4.2.2; Table 4.2.1). The ASTER DEM data has a gridded spatial resolution of ca 30 m and an estimated vertical (elevation) accuracy of between 10 and 25 m per pixel. For the Assarel study area, the full DEM scene corresponds to a 1 x 1-degree geographic swath extending from 42°-00' to 43°-00' North, and 24°-00' to 25°-00' East (Fig 4.2.1). This coverage incorporates the mountainous Balkan/Srednogorie belt in the north and the northern part of the Rhodopes range in the south, approximately centred on the town of Chisarja.

Following importation to ArcGIS (via a GeoTIFF file), a subset area that overlaps with the 1:100 000-scale Panagyurishte topographic and geological map sheets was clipped from the ASTER DEM and transformed from geographical coordinates to the UTM Zone 35T North coordinate system (Fig. 4.2.2). This coordinate system allows for the integration of all Assarel-related geodata into a single reference framework so a seamless transition from the near-mine to within-mine scales can be achieved for the test site. The extracted DEM subset covers a ca 60 x 60 km area approximately centred on Panagyurishte, with the Assarel deposit located within the western third of this coverage area (Fig. 4.2.2).

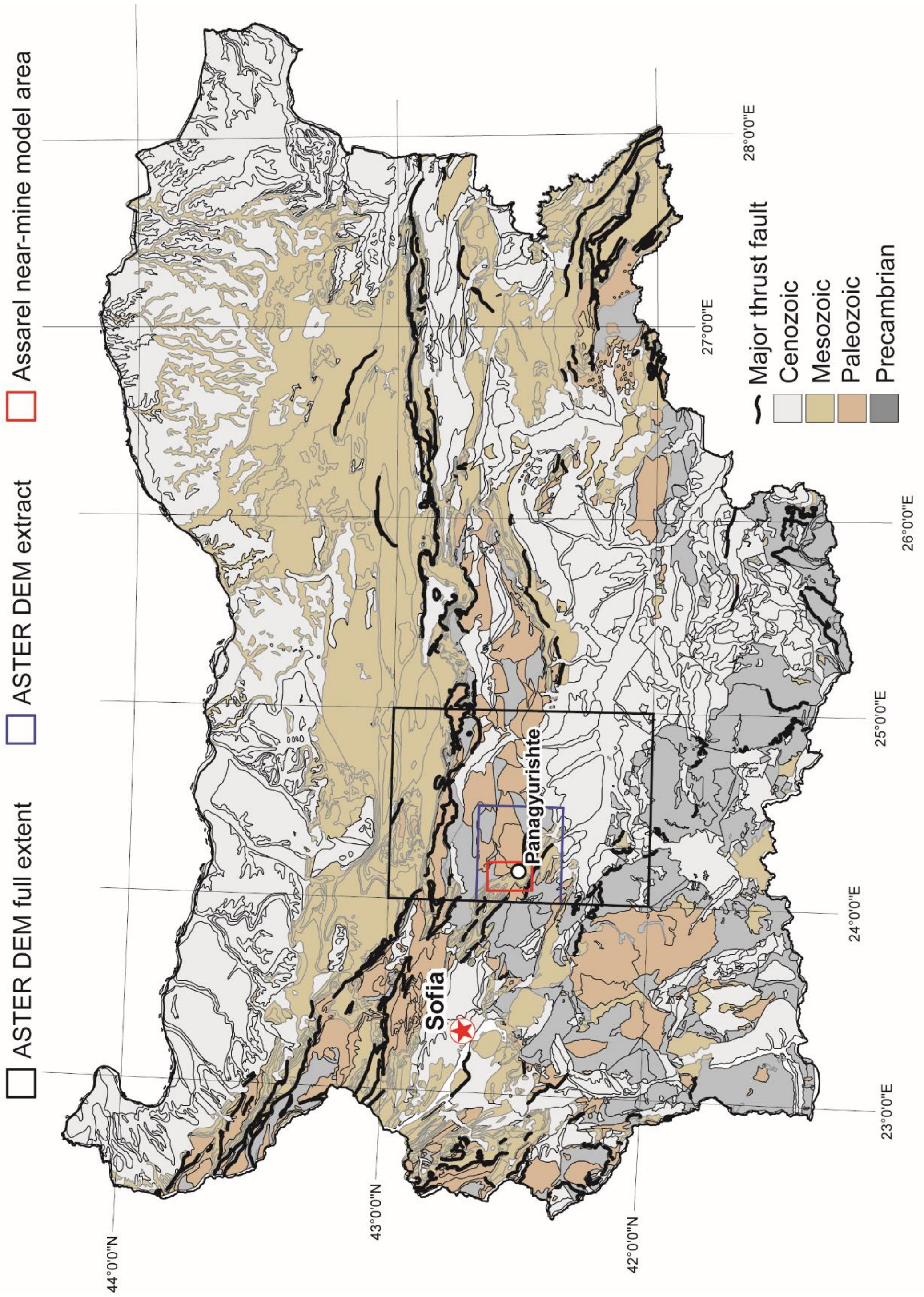

Figure 4.2.1. Geology of Bulgaria showing lithostratigraphic units grouped by major time-scale divisions (based on 1:500 000-scale map from the Bulgarian Committee on Geology - Department of Prospecting and Geophysical Mapping, 1989). The location of Panagyurishte and the extent of the ASTER global digital elevation model (black and blue rectangles) and the Assarel near-mine 3D modelling area (red rectangle) are also shown.

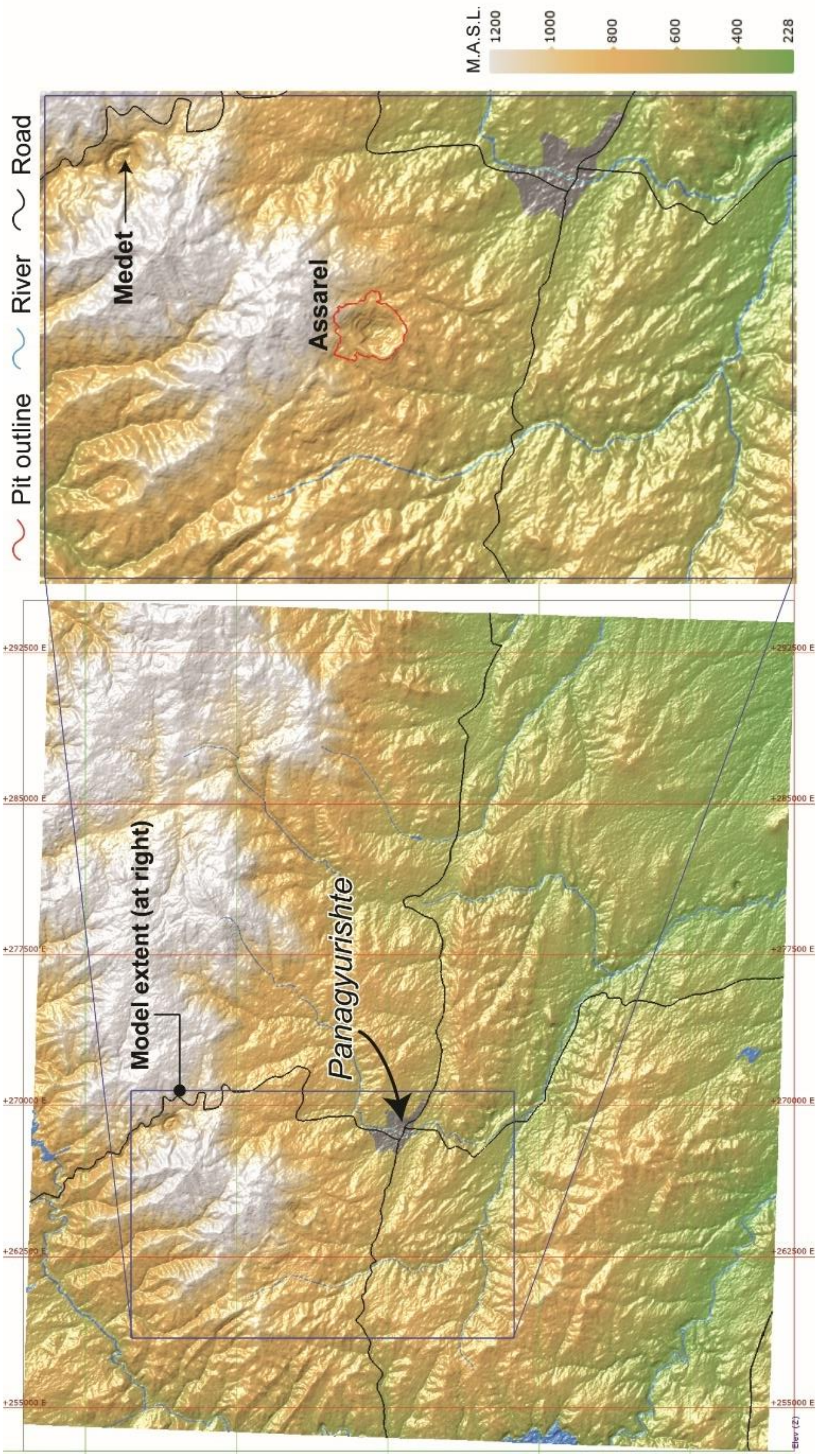

Figure 4.2.2. Base DEM dataset for the Panagyurishte-Assarel area (coordinate system is UTM 35T North with WGS84 spheroid). The extent of the Aster elevation data is shown at left corresponds to that of the Panagyurishte 1:100 000-scale topographic and geological map sheets (see Fig. 4.2.3). Zoomed-in view at right showing Assarel near-mine model extent (blue rectangle) and outline of Assarel open pit (in red). The location of the Medet open pit is also shown. M.A.S.L. = metres above sea level.

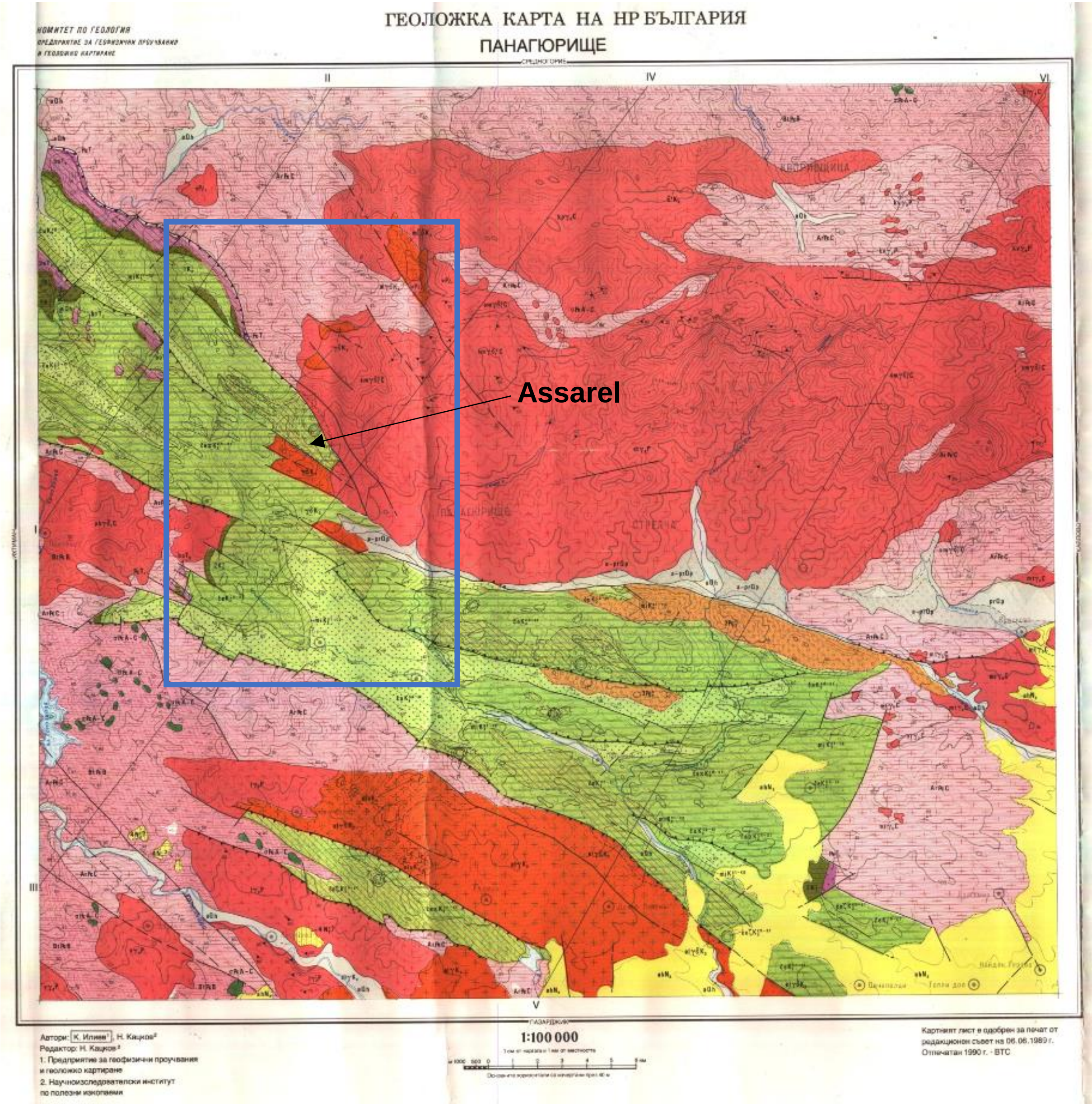

Figure 4.2.3. Scanned geological map of the Panagyurishte area used for 3D geomodelling (1: 100 000-scale; Iliev & Katckov 1990). The extent of the Assarel near-mine modelling area (blue rectangle) and location of the Assarel Cu deposit are also shown.

The extent of the Assarel near-mine model is shown in Figures 4.2.1 – 4.2.3. This c. 12 x 19 km rectangular area extends from the Medet Cu-Mo-Au deposit in the north to the Krasen Au-Cu prospect in the south. From a modelling perspective, this extent was chosen to incorporate the major Cu-Au-(Mo) deposits at both Assarel and Medet which would likely maximise available geological information – particularly structural and/or cross-section information to help constrain geological features at depth. The modelling area also incorporates the NW-SE-aligned Late Cretaceous volcanic-plutonic rocks that includes the Assarel effusive/volcanic formation, porphyry Cu-related hypabyssal intrusions and their associated bounding faults. Additionally, the model area contains Precambrian metamorphic rocks (Arda gneiss group) along its northern and southern limits, which act as a somewhat symmetrical bounding unit for the near-mine model (Figs. 4.2.2 and 4.2.3). In terms of the third dimension, the near-mine model extends to -500 m below sea level giving a maximum vertical extent of c. 2 000 m based on the highest elevation of ca +1 500 m in the north at Bratiya, west of Medet (e.g. Fig. 4.2.2).

Base geology information for the near-mine model relied on previously published government and academic maps from the Panagyurishte ore district (Figs. 4.2.3 and 4.2.4). The main maps used were the 1:100 000 and ca 1:75 000 regional- to camp-scale geology maps shown in Fig. 4.X.4 (see also Table 4.2.1). An additional map of the Medet deposit shown in Popov et al. (2012) helped to further constrain the geology of that area. Although the more detailed camp-scale maps of Assarel-Medet and Krassen-Petelovo taken from Popov et al. (2012) only cover about 60% of the model area (Fig. 4.2.4), their inclusion helps to further constrain the 3D geology of the central, north-eastern and south-eastern parts of the model.

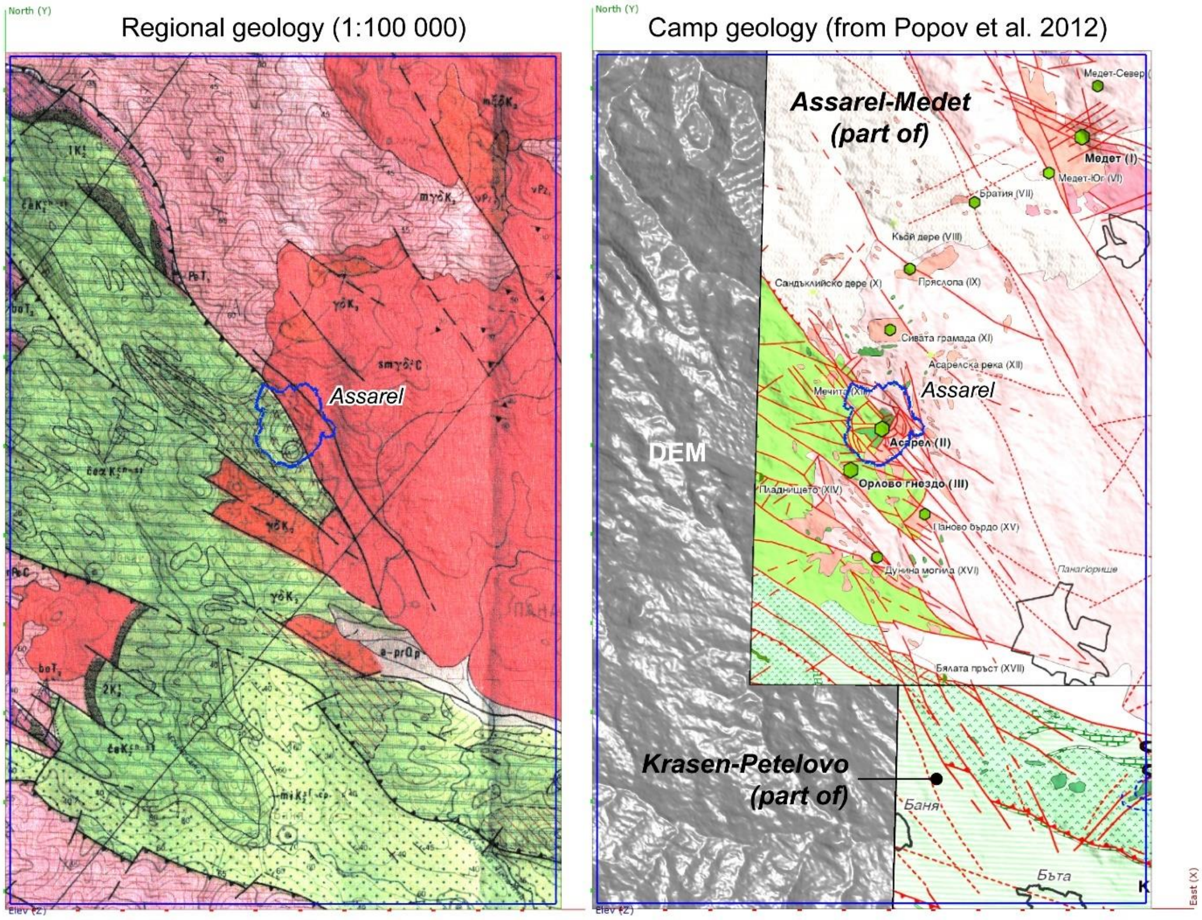

Figure 4.2.4. Near-mine model area showing regional geology (left) and more detailed camp-scale geological maps (right). The latter partly cover the total near mine modelling area (blue rectangle). Green circles at right are known mineralized deposits and prospects.

The published Panagyurishte regional geology map (1:100 000-scale; Iliev & Katckov 1990) contains three approximately NE-SW-aligned cross-sections that highlight the broad 3D form of the main geological units and structures in the Assarel area (Fig. 4.2.5). Cross-sections I-II and III-IV (western and central cross-sections, respectively) both transect the near-mine model area (Fig. 4.2.5) and help constrain and orient lithologies and major faults below the modelled bedrock surface. The central Late Cretaceous volcanic-plutonic sequence displays an overall basinal or graben-like form that is bounded to the north and south by major SW- and/or NE-dipping faults (discussed further in Section 4.2.2.2 below). Several folds with typically c. NW-aligned axes are also observed within this central volcanic sequence (Fig. 4.2.5).

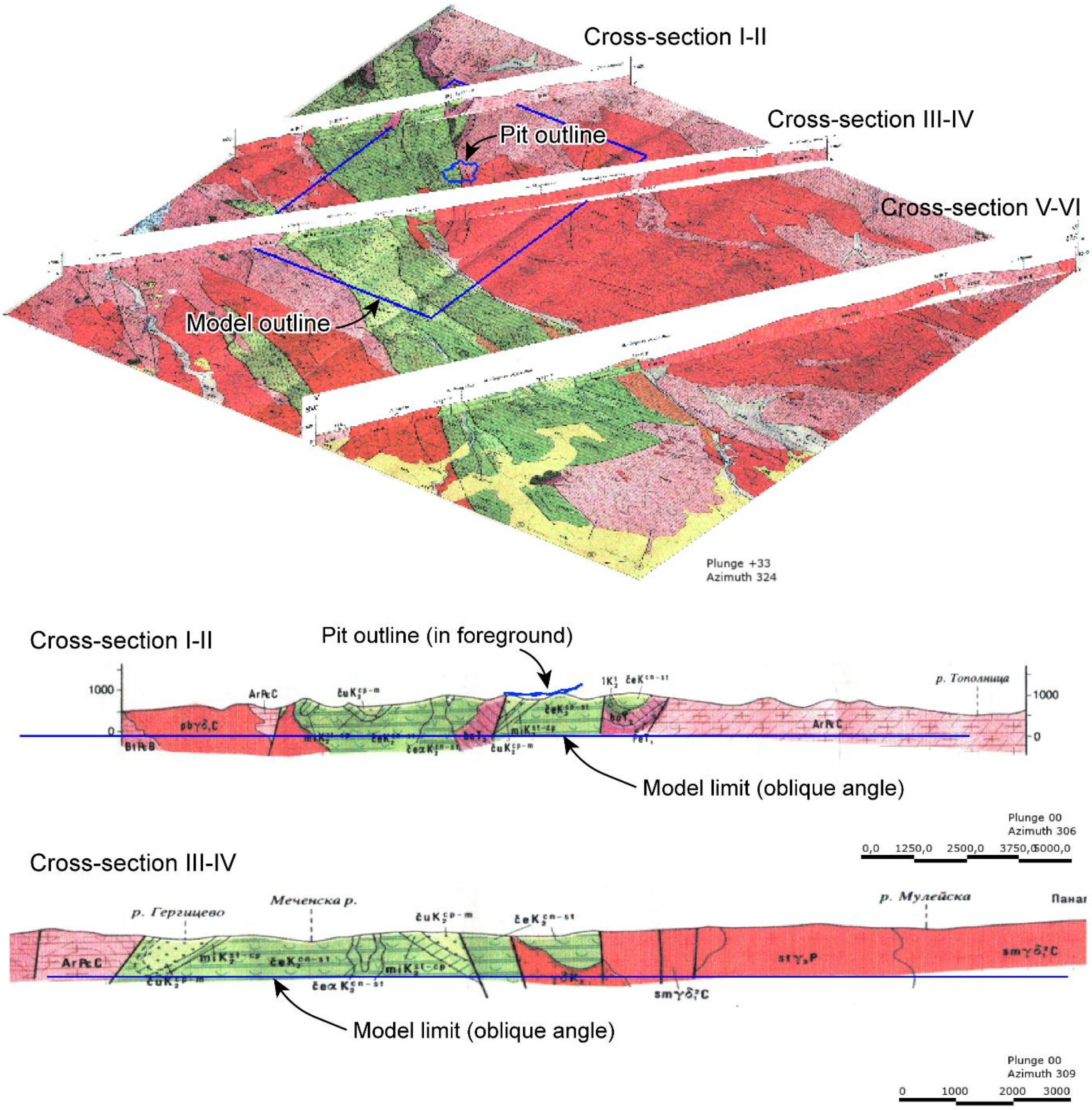

Figure 4.2.5. Geological cross-sections (1) covering the Panagyurishte area (1:100 000-scale, from Iliev & Katckov 1990). Cross-sections I-II and III-IV transect the designated 3D modelling area (see top image). Lower images show cross-sections I-II and III-IV “face on” looking toward the northwest. Both cross-sections illustrate the orientations and dips of major faults and supracrustal rocks in the Panagyurishte area.

4.2.2.2 Modelling approach

A practical requirement for Assarel near-mine modelling was to use a common coordinate system to spatially integrate the various data types derived from open and mine-site sources. As the study area falls within the UTM 35T North grid zone, and this system was used to record the position of field samples collected in October 2018 (see X-Mine report D1.1), the UTM system was chosen as a common reference framework for the near-mine model. Consequently, all mine-related data (e.g. drill hole logs, assay data), typically acquired and held within a local coordinate system, requires transformation to UTM for future modelling work (Section 4.2.4 below). It is envisaged that the use of the UTM coordinate system will enable the seamless integration of both existing and modelling-derived geodata layers from the near-mine (regional) to the within-mine scales (Fig. 4.2.6).

In general, the Assarel near-mine model area comprises an approximately NW-trending, Late Cretaceous volcanic-plutonic centre, bound to the north and south by Precambrian metamorphic rocks, and containing a through-going fault system. The faulted nature of the area and the fact that faults typically act as boundaries to many of the geological units dictated the modelling approach. Specifically, fault surface traces were digitized first, which divided the model area into a series of semi-independent fault blocks (see Section 4.2.2.3 below). This allowed each block to be further modelled by adding lithology contact surfaces and other geological information (e.g. mineralized locations, alteration zones etc.). Fault dip values were derived from map cross-sections (e.g. Fig. 4.2.5), the slope properties of the topographic surface (via a Leapfrog Geo interpretive modelling routine) or were treated as vertical structures in cases where dip information was not known.

Lithotypes were similarly modelled by digitizing contact surface traces and assigning 3D properties using the orientation of previously defined bounding faults or structural point measurements (strike, dip) derived from the geological maps. Numerous intrusions assigned to the Late Cretaceous diorite-granodiorite and Assarel subvolcanic suites lack structural information regarding their subsurface geometries or forms. These examples were generally treated as vertical bodies extending from the surface through the model space, or to depths defined by truncating faults. Geological cross-sections from Assarel and other porphyry deposits in west-central Bulgaria (e.g. Vlaikov Vruh) typically depict Late Cretaceous porphyritic stocks as relatively steep (70 - 90°) cylindrical or pipe-like intrusions (Strashimirov et al. 2003), although shallower-dipping examples with orientations that mimic that of host supracrustal rocks also occur (e.g. Elatsite Cu deposit).

The ability to create a high-quality 3D near-mine model for the Assarel area is somewhat hampered by the limited number of cross-sections and structural orientation measurements available, which help constrain the 3D projection of geological features into the subsurface. This limitation is exacerbated by the present unavailability of near-mine regional geophysical data for the area. Future modelling work aims to incorporate regional magnetic and gravity field data from the Bulgarian Ministry of Energy to help better constrain the subsurface geology of the near-mine area. On-going modelling of regional hydrothermal alteration and mineralization occurrences is based on digitized line and point data derived from published geological maps (e.g. Fig. 4.2.3). The 3D distribution of alteration zones at the deposit-scale will be further conducted as part of X-Mine WP1 using drill core logging information from Assarel (see Section 4.2.2.4 below).

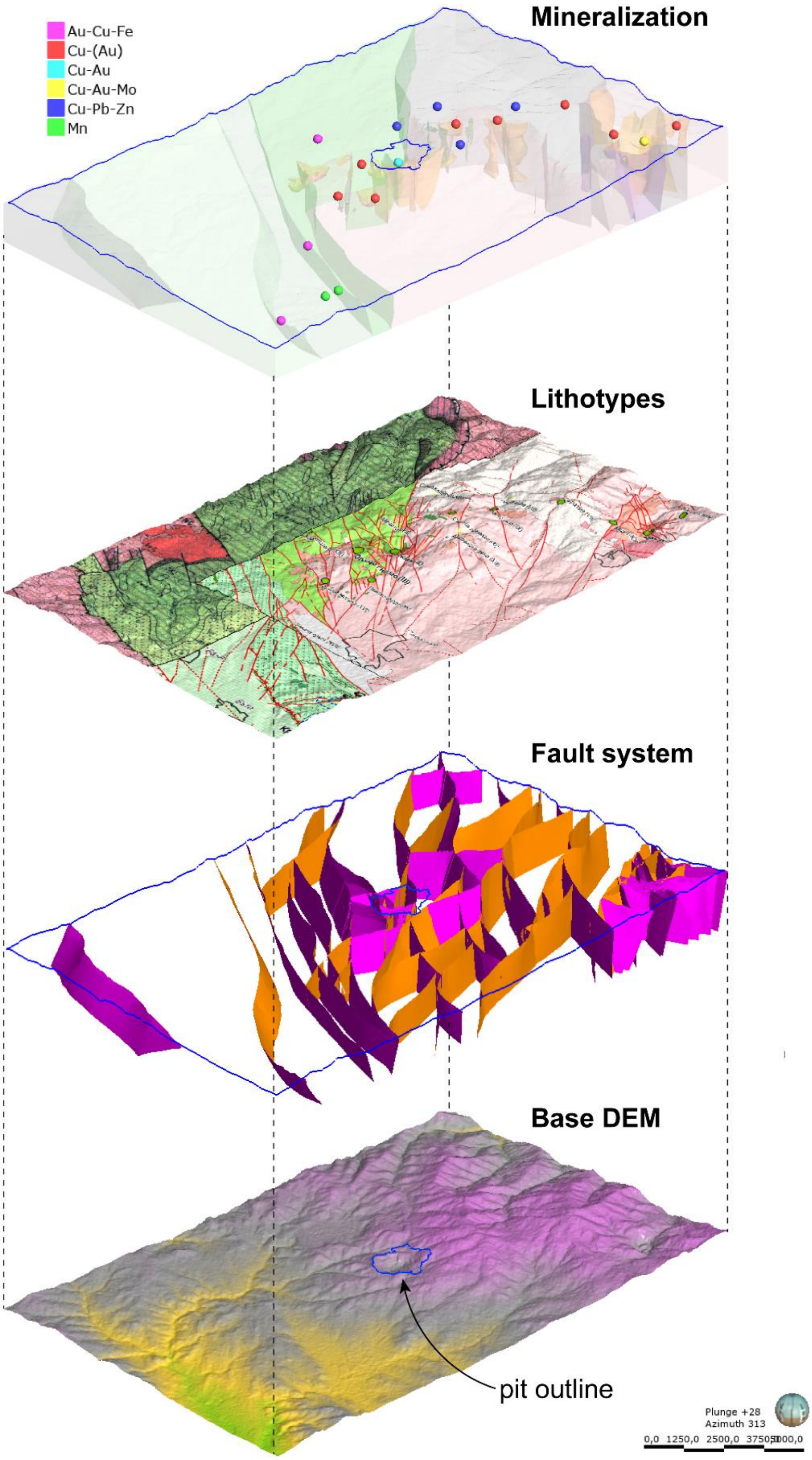

Figure 4.2.6. Examples of various data layers in 3D space used to produce Assarel 3D near-mine geomodelling outputs (e.g. fault system at top). The modelling area corresponds to that shown in Fig. 4.2.4.

4.2.2.3 Modelling results I: Fault network model

The structural character of the Assarel-Panagyurishte area is dominated by a network of c. NW- to NE-aligned, moderately to steeply dipping faults which form part of a major NW-trending deformation zone called the Iskar-Yavoritsa shear zone (Gallhoffer et al. 2015). This deformation zone, in turn, forms the central part of the larger Maritsa shear zone, a crustal-scale suture separating the northern Srednogorie and southern Rhodope terranes in the south-central sector of the Balkan orogen (e.g. Burchfiel et al. 2011, Naydenov et al. 2013). From a metallogenic perspective, Late Cretaceous tectonothermal events focused within and adjacent to the Iskar-Yavoritsa (Maritsa) shear zone facilitated porphyry- and epithermal-style Cu-Au mineralization along this composite structure (Drew 2005, Richards 2015).

Although specific details about the kinematic and displacement characteristics of most faults in the study area are generally lacking, previous regional mapping has identified several major normal- and reverse-type faults that generally dip to the NE and SW (see cross-sections I-II and III-IV in Fig 4.2.5). Taken together, the fault network at Assarel bears the hallmarks of a duplex system formed during right-lateral (dextral) strike-slip deformation. This structural configuration likely had an important influence on the siting of porphyry Cu-Au mineralization in the area (see below; cf. Drew 2005).

Preliminary results of 3D structural modelling of the Assarel near-mine area are shown in Fig. 4.2.7. In general, fault densities and characteristics (orientations, lengths) vary across the area, although c. NW-, NNW- and NE-trending faults predominate. Fault dips are moderate to steep (c. 65 - 88°) and generally steepen towards the northeast (Fig. 4.2.7A). Several faults or deformation zones have longer, curvilinear surface traces and typically strike c. NW-SE. These structures, which include the Medet, Miala and Panagyurishte fault zones (MFZ, MiFZ and PFZ in Fig. 4.2.7A, respectively), are interpreted as primary (first-order) faults or shear zones that control the distribution of relatively shorter, second- and possibly third-order splay faults with mainly NNW- to NE orientations. NNE- to NE-trending faults tend to form faulted segments between the c. NW-aligned first-order structures and locally exhibit a stepped pattern, with some locally displaced by the NW-aligned faults. These segments may have formed during the lateral transfer of displacements via releasing-type stepover zones within the larger strike-slip fault system (e.g. Berger 2007). Additional structural mapping across the near-mine study are should be performed to fully characterise the nature of the wider deformation zone hosting the Assarel deposit.

Based on the modelled fault network, a total of 122 fault blocks subdivide the near-mine model area (Fig. 4.2.7B). In general, a higher concentration of smaller blocks occurs near the Assarel and Medet deposits, while the Chugovitsa, Petolovo and Assarel volcanic formations form larger fault blocks south of Assarel. This spatial variation may reflect the greater number of NE-aligned “cross-faults” at the deposit sites, and/or the greater number of mapped faults for these areas (due to the deposit locations). Cross-faulting at both Assarel and Medet comprises c. NE-trending faults that are either bound or cross-cut by WNW- to NNW-oriented faults (Fig. 4.2.7C). These structural intersection zones represent areas of higher secondary permeability and likely formed focused zones of increased hydraulic conductivity and fluid flow, which may have promoted Cu ± Au ± Mo mineralization (cf. Tosdal & Richards 2001). More detailed structural mapping is required to further test this idea however. Within the Assarel pit, extensional faulting in the main pit is visible as planar to somewhat listric fault surfaces with dark grey to black, fine-grained, clayey fault gouge (Fig. 4.2.7D).

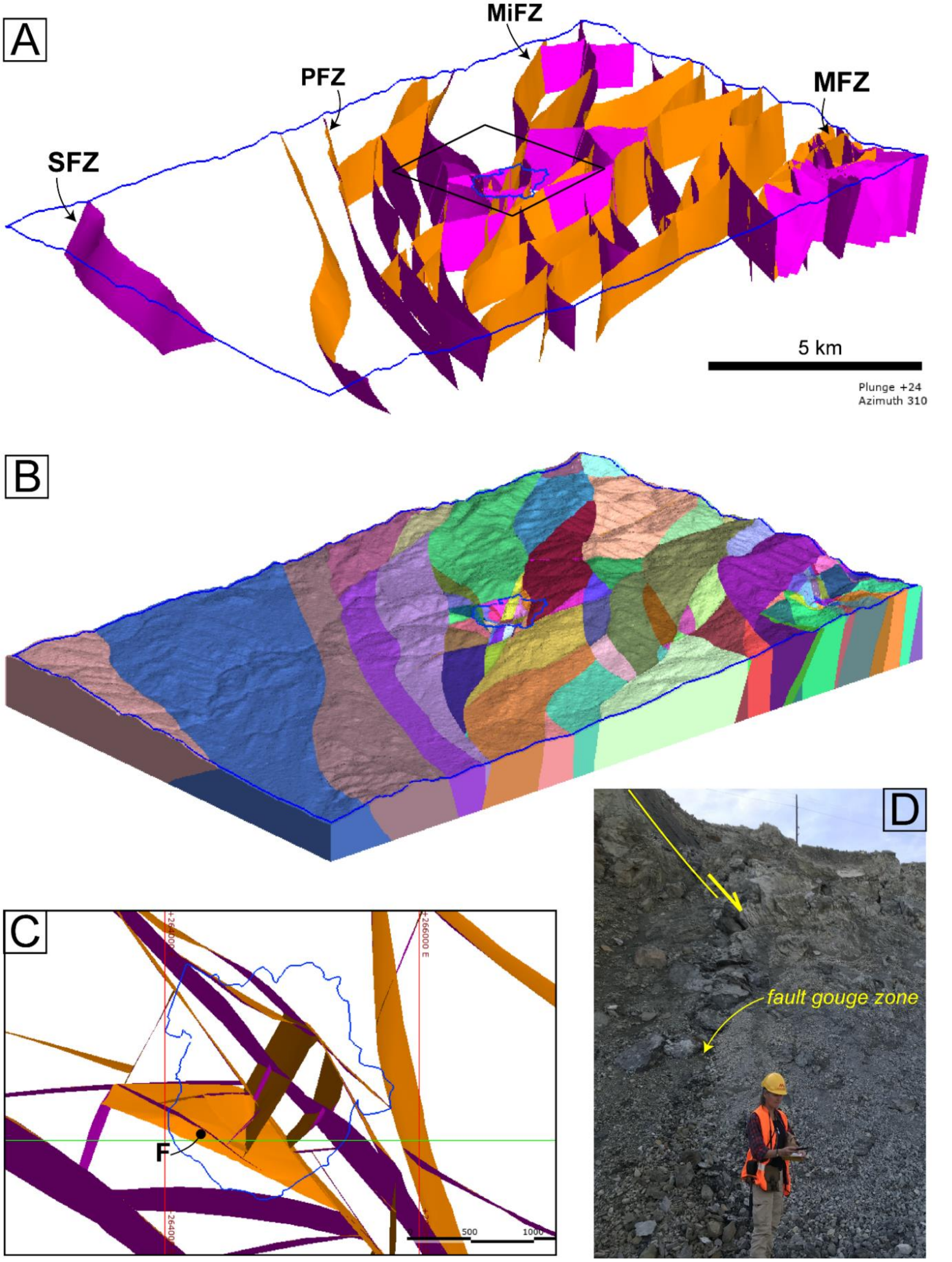

Figure 4.2.7. Modelled fault system at Assarel and surrounding area. A. Fault geometries as seen looking to the northwest. Orange = northern side of fault plane, purple = southern side of fault plane. Major fault zone abbreviations: MFZ = Medet fault zone, MiFZ = Miala fault zone, PFZ = Panagyurishte fault zone, SFZ = Stefanco fault zone. Black rectangle at Assarel corresponds to outline of area shown in C. B. Modelled fault blocks (n = 122) for the Assarel near-mine area based on the fault system shown in A. C. Map view of faults close to and within the Assarel open pit (blue polyline). D. Example of dip-slip fault within the Assarel open pit and corresponding to the location marked “F” in C. View to the west-northwest.

On-going near-mine modelling aims to refine the geometry of the Assarel-Panagyurishte fault network and further constrain its structural properties. Verification of the orientation, 3D depth extension and kinematics of individual fault surfaces is strongly dependent on additional data inputs such as geophysical data and structural field measurements. Without additional constraints such as these, the near-mine model is limited to the basic structural picture provided by the input maps (e.g. Fig. 4.4.4). Improvements to the near-mine fault model will help establish structural continuities and links to the Assarel within-mine (deposit) model and thus constrain the structural character of the deposit at multiple scales. Modelling of fold structures within the Late Cretaceous volcanic-sedimentary sequence is also ongoing as part of the Assarel near-mine modelling work (see below also).

4.2.2.4 Modelling results II: Lithology model

Preliminary results of lithological modelling for the Assarel near-mine area are shown in figure 4.4.8. Overall, the new lithology model directly reflects the input regional geology maps used in its construction (Fig. 4.4.4 and Table 4.2.2). The area is dominated by five major rocks units; (1) the *Arda gneiss group (AGG)*, which forms two northern and southern basement blocks that bound the other rock units, (2) the eastern *Palaeozoic granitoid* which intrudes the AGG and is in tectonic contact with younger (Late Cretaceous) volcanic-sedimentary units, (3) the c. NW-aligned *Assarel effusive/volcanic formation* in the north-central part of the model area, (4) the similarly c. NW-aligned *Petolovo formation* to the south, comprising andesitic volcanic rocks, and (5) the wedged-shaped *Chugovitsa formation* in the south-central model area, comprising shallow-marine sedimentary rocks. The latter three units together define a c. NW-aligned package of mainly Late Cretaceous volcanic-sedimentary rocks inferred to have formed within an intra- or back-arc (suprasubduction) depositional basin (e.g. von Quadt et al. 2005).

Late Cretaceous intrusive rocks mainly form a c. N- to NNE-aligned, c. 12 km-long zone from south of Assarel to Medet, and comprise relatively small, sub-volcanic stocks and plugs. This orientation trend mimics the approximate NNW to NNE distribution of Cu-Au mineralization in the area – a spatial correlation which reflects the genetic link with dioritic to granodioritic porphyritic intrusive bodies (see uppermost model in Fig. 4.2.6). A correlative c. N-S to NNW-SSE alignment of coeval porphyry- and epithermal-style Cu-Au mineralization in the broader Srednogorie-Panagyurishte region has also been noted (Drew 2005). The Late Cretaceous intrusions are assigned to the Assarel subvolcanic porphyry and diorite-granodiorite suite and are broadly comagmatic with andesitic rocks of the Assarel volcanic and Petolovo formations (Table 4.2.2). The c. 90 Ma gabbro-diorite intrusion at Medet located in the northeast of the model area (Fig. 4.2.8), provides evidence for bimodal mafic-intermediate magmatism in the area at that time (von Quadt et al. 2005).

Overall, the 3D lithostratigraphy of the Assarel area (Fig. 4.2.8) reflects the combined effects of superimposed Palaeozoic and Mesozoic tectonothermal events, with Late Cretaceous volcanic-sedimentary and plutonic rocks forming a dominant central basinal sequence in the study area (Table 4.2.2; cf. von Quadt et al. 2005, Gallhofer et al. 2015). For the supracrustal rocks, on-going near-mine modelling aims to refine their distribution, geometries and contact surfaces, and will focus on modelling the synclinal character of the Chugovitsa and Mirkovo formations (see cross-sections in Fig. 4.2.5). The modelling of other geological features including the surficial distribution of regional propylitic (chlorite-epidote) alteration affecting andesitic volcanic rocks will also be incorporated in the near-mine model.

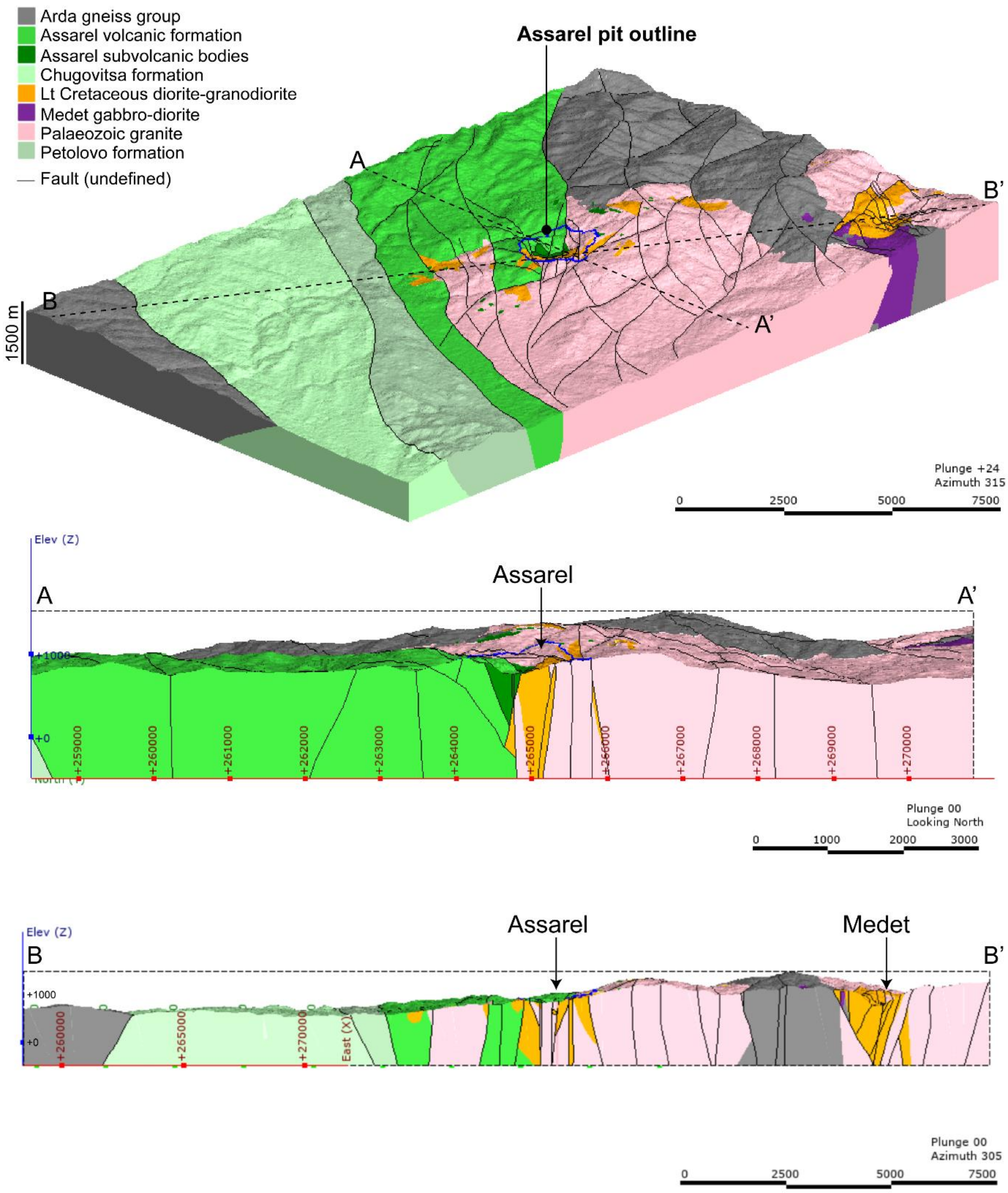

Figure 4.2.8. Preliminary 3D geomodel and interpreted cross-sections of the Assarel near-mine model area (corresponding to the area in Fig. 4.2.4). The outline of the Assarel open pit is also shown (blue polygon). The addition of both the Bosnek and Mirkovo formations as shown in Figure 4.2.3 and 4.2.4 is required as part of the on-going modelling work. Note the scale difference between cross-sections A-A' and B-B' to fit both within the page width margin.

Table 4.2.2. Geological units comprising the Assarel near-mine 3D model (listed youngest to oldest). Red text = volcanic-sedimentary units to be modelled.

Unit	Age	Brief description	Distribution in model and status
Alluvium-fluvial deposits	*Quaternary*	*Alluvial gravel, sand*	*SE of Panagyurishte town, extending eastward (to be modelled)*
Chugovitsa formation	Late Cretaceous	Marl, limestone, calcareous sandstone	Southernmost supracrustal block (preliminarily modelled)
Mirkovo formation	*Late Cretaceous*	*Clayey limestone*	*Minor supracrustal horizons in the NW and SE parts of the model area (to be modelled)*
Diorite-granodiorite bodies	Late Cretaceous	Diorite, granodiorite intrusions	Central Assarel and north-eastern Medet areas, forming an approximate SW-NE cluster of intrusive bodies (preliminarily modelled)
Assarel subvolcanic porphyries	Late Cretaceous	Andesitic porphyry stocks and dykes	Central Assarel area (preliminarily modelled)
Assarel formation	Late Cretaceous	Andesitic volcanic-volcaniclastic deposits	Central Assarel area and extending westward (preliminary modelled
Petelovo formation	Late Cretaceous	Andesitic volcanic rocks	NW-SE-aligned supracrustal block in contact with the Chugovitsa formation to the south and Assarel volcanic formation to the north (preliminarily modelled)
Chelopech formation	*Late Cretaceous*	*Volcanic rocks and related subvolcanic bodies*	*Minor supracrustal horizons in the SW and SE of the model area (to be modelled).*
Medet gabbro-diorite	Late Cretaceous	Gabbro, diorite, peridotite intrusions	NE model area, adjacent to Medet open pit (preliminarily modelled)
Bosnek formation	*Middle Triassic*	*Dolomite*	*NW model area (to be modelled)*
Srednogorie (Palaeozoic) granite	Carboniferous - Permian	Granite, granodiorite	Eastern and northeast model area (preliminarily modelled)
Arda Gneiss Group	Early Palaeozoic	Pre-Rhodopean gneiss, amphibolite	Northern and southern bounding blocks (preliminarily modelled)

4.2.3 On-going 3D modelling and XRT-XRF scanning for X-Mine report D1.3

On-going X-Mine WP1 geomodelling work for the Assarel test site aims to complete the near-mine model and progress to the full construction of the Assarel within-mine model. The integration of these two scales and their respective datasets should provide a comprehensive assessment of the 3D setting and character of the Assarel porphyry Cu-Au system. Importantly, within-mine modelling will incorporate oriented 3D drill core XRT-XRF results using X-Mine pilot scanning technologies (e.g. X-Mine Work Package 5). This information will provide further constraints on the character of the Cu-Au mineralization in 3D space.

Within-mine (deposit-scale) modelling work for Assarel has been on-going concurrently with near-mine modelling and some preliminary results are shown in Figure 4.2.9. The within-mine model incorporates a detailed open pit DEM (Fig. 4.2.9A), ground magnetic field data covering the pit (Fig. 4.2.9B), and lithological, structural and mineralogical (alteration-mineralization) information primarily based on drill core logging and complementary field sampling. Additionally, drill core information provided by Assarel-Medet JSC includes down-hole Cu and Au assay data, and other geochemical data. Combined, this information will help constrain the

3D geometry of the Assarel ore body along with other deposit information including 3D distributions of lithotypes, alteration assemblages and elements (Fig. 4.2.9C-D), and the orientations of within-pit structures to correlate with those at the near-mine-scale.

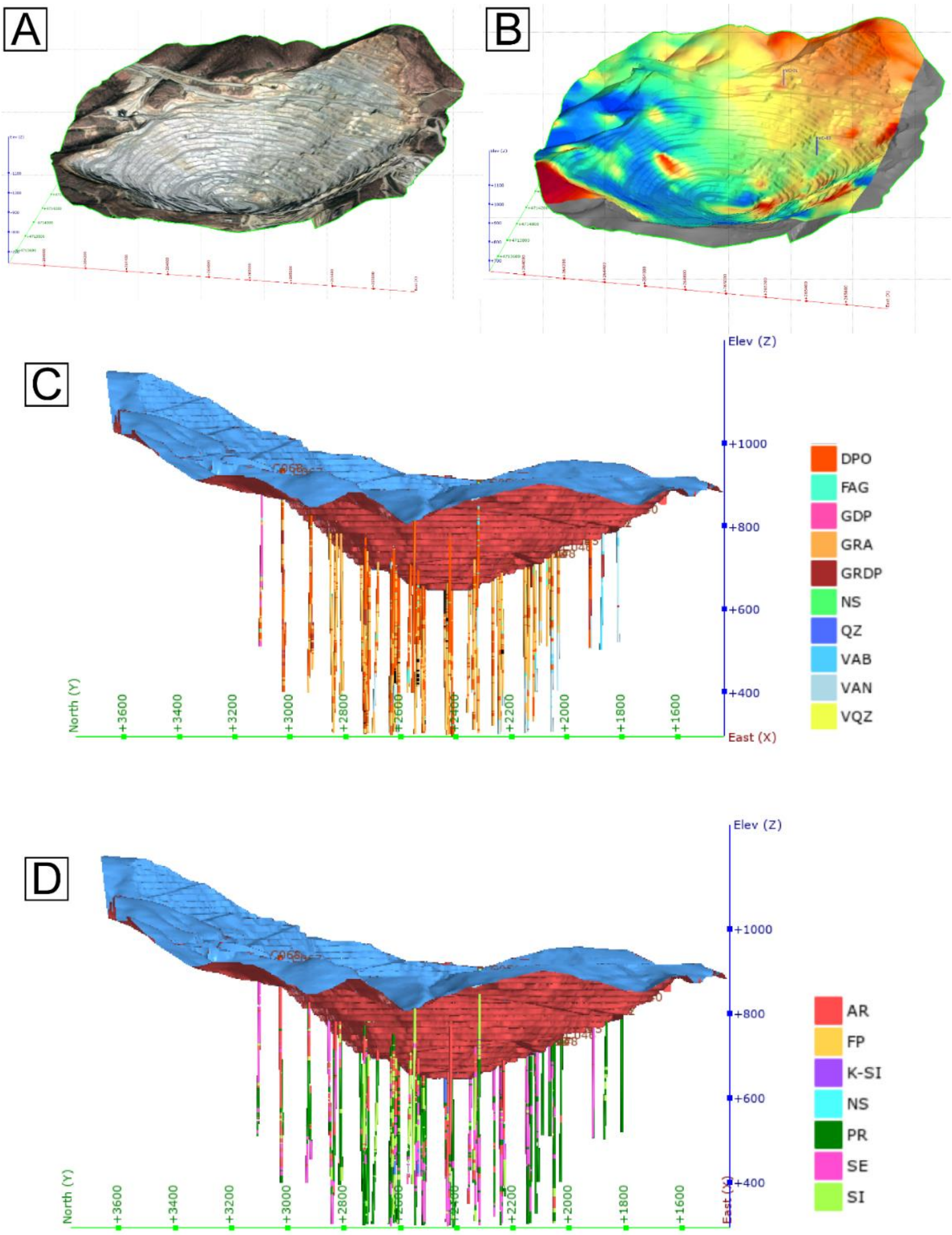

Figure 4.2.9. Assarel within-mine 3D modelling (coordinates shown are in local mine grid). A. Open pit oblique view (to the north west) showing draped aerial photograph. B. Open pit oblique view (to the north west) showing draped magnetic field data. C. View to the east showing C001 – C070 drill holes with lithology information. Abbreviations: DPO = diorite porphyry, FAG = fault gauge/zone, GDP = granodiorite porphyry, GRA = granite, GRDP = granodiorite porphyry, NS = no sample, QZ = quartz-rich zone, VAB = volcanic breccia, VAN = volcanic tuff, VQZ = quartz veins. D. View to the east showing C001 – C070 drill holes with alteration information. Abbreviations: AR = argillite, FP = feldspar, K-SI = potassium-silicate (K-feldspar), NS = no sample, PR = propylitic, SE = sericite, SI = silica (quartz).

Geological information derived from existing and new drill core at Assarel will provide the main geological constraints for the within-mine 3D model. Critically, a planned campaign of oriented drilling by Assarel-Medet JSC within X-Mine WP1 will help further constrain the structural and lithological character of the ore body and will offer oriented drill core material for XRT-XRF scanning and pilot technology calibration (see below). A refined assessment of the 3D distribution of argillic-, propylitic- and phyllic (sericite)-type alteration shells at Assarel based on the existing and new drilling will form part of the within-mine modelling and should complement and refine the currently mapped alteration zones at the deposit (Fig. 4.2.10).

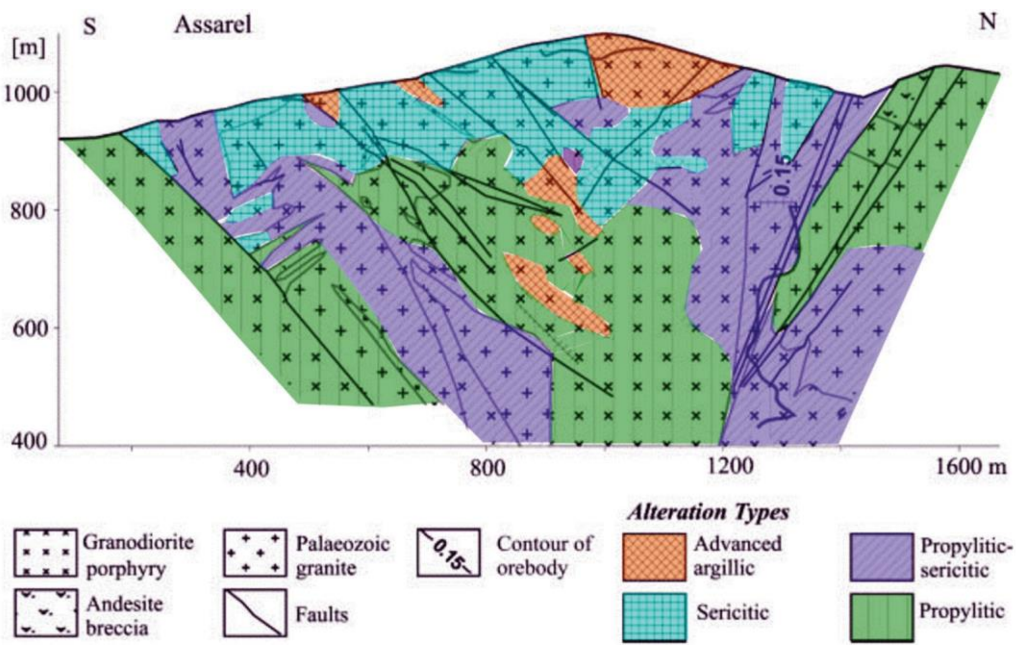

Figure 4.2.10. North-south cross-section through the Assarel open pit showing the pre-mining spatial distribution of the main geological units and alteration zones. Modified after Strashimirov et al. (2003).

A key task of X-Mine WP1 activities is to provide the geological context for XRT-XRF drill core scanning and offer a sound platform for calibration of the pilot scanning technology. Assarel within-mine modelling thus provides the necessary space-time framework for drill core intervals used for scanning and instrument assessment (see Delivery Report D1.1). Mineralogical and geochemical investigations of scanned Assarel samples is on-going to constrain the 3D distributions of Cu and related key elements within the porphyry system (e.g. Au, Ag, Bi). Preliminary results of this work were reported in X-Mine Delivery Report D1.1, Cioacă et al. (2018) and Munteanu et al. (2019). New results are shown in Figures 4.2.11 and 4.2.12.

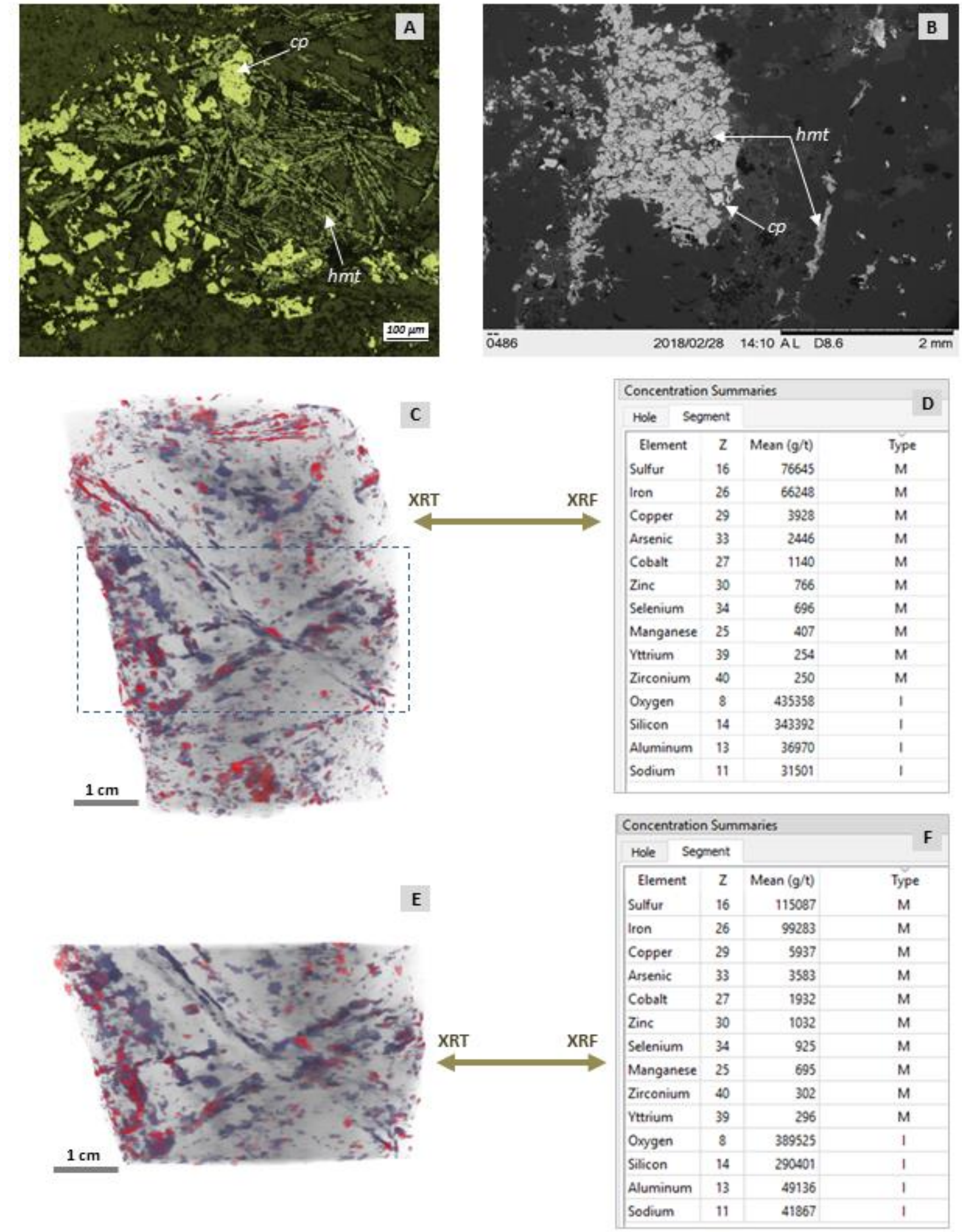

Element	Z	Mean (g/t)	Type
Sulfur	16	76645	M
Iron	26	66248	M
Copper	29	3928	M
Arsenic	33	2446	M
Cobalt	27	1140	M
Zinc	30	766	M
Selenium	34	696	M
Manganese	25	407	M
Yttrium	39	254	M
Zirconium	40	250	M
Oxygen	8	435358	I
Silicon	14	343392	I
Aluminum	13	36970	I
Sodium	11	31501	I

Element	Z	Mean (g/t)	Type
Sulfur	16	115087	M
Iron	26	99283	M
Copper	29	5937	M
Arsenic	33	3583	M
Cobalt	27	1932	M
Zinc	30	1032	M
Selenium	34	925	M
Manganese	25	695	M
Zirconium	40	302	M
Yttrium	39	296	M
Oxygen	8	389525	I
Silicon	14	290401	I
Aluminum	13	49136	I
Sodium	11	41867	I

Figure 4.2.11. XRT-XRF scanning results for sample AS22 from Drill hole C021 (depth in hole: 40.43 m). **A)** Photomicrograph in reflected light of chalcopyrite – hematite assemblage in intensely mineralized diorite porphyry; **B)** Back-scattered electron image of hematite and chalcopyrite forming clusters and veinlets; **C)** XRT scanning image (obtained using Orexplore XRF-XRT scanner) showing mineralization on veinlets and as fine-disseminated minerals; **D)** XRF data presenting the concentrations in elements (mean values); **E)** XRT scanning image of the segment delimited on figure 1C; **F)** XRF concentration data on the segment from figure 1E, showing that in the segment richer in veinlets, the mean values of concentration in measured elements as Cu, Fe, S, As, Co etc. are higher. Abbreviations: cp – chalcopyrite, hmt – hematite; I – inferred content; M – measured content.

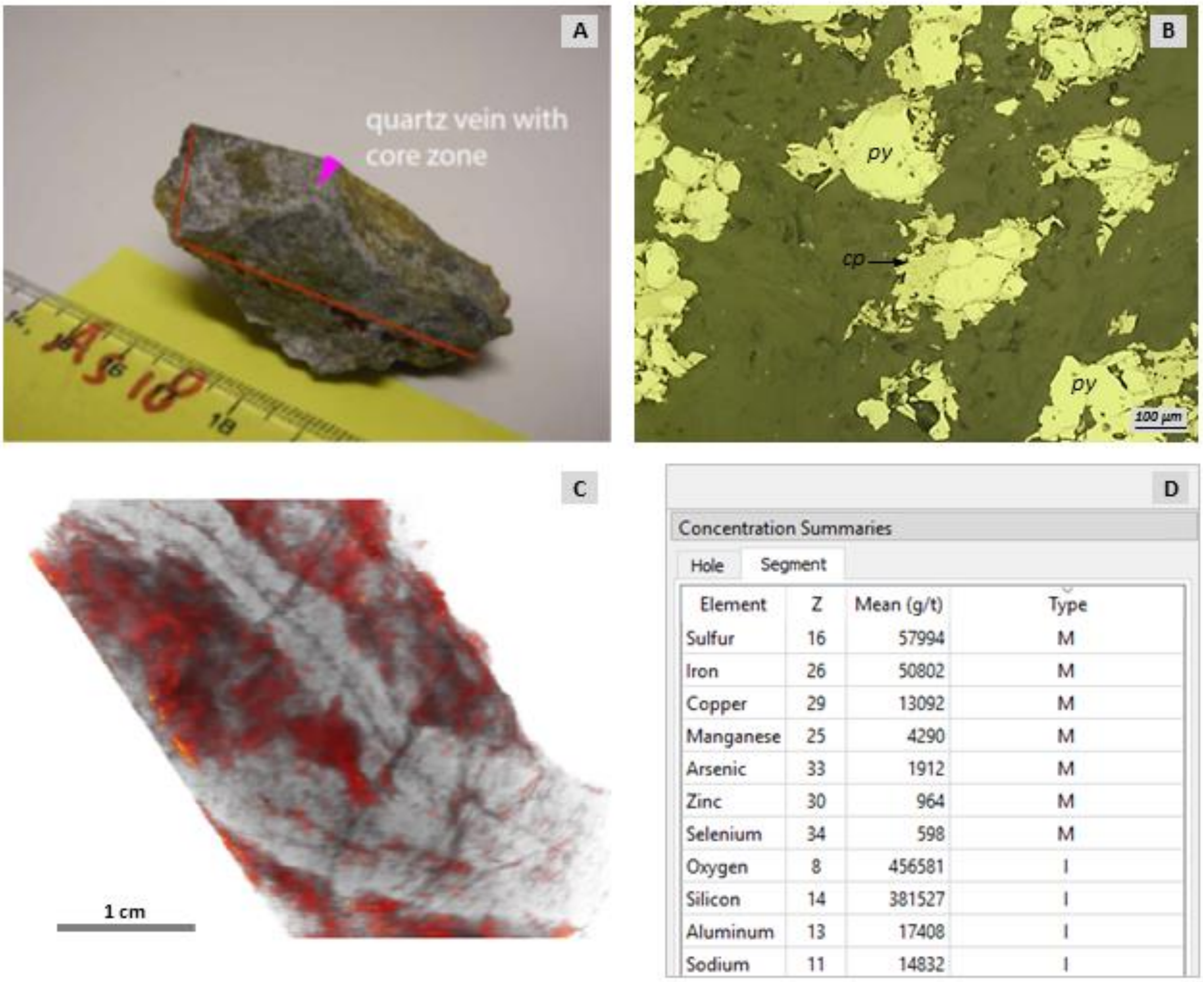

Element	Z	Mean (g/t)	Type
Sulfur	16	57994	M
Iron	26	50802	M
Copper	29	13092	M
Manganese	25	4290	M
Arsenic	33	1912	M
Zinc	30	964	M
Selenium	34	598	M
Oxygen	8	456581	I
Silicon	14	381527	I
Aluminum	13	17408	I
Sodium	11	14832	I

Figure 4.2.12. XRT-XRF scanning results for sample AS18 from Drill hole C021 (depth in hole: 74.10 m). **A)** Macrophotography showing a vein of quartz and metallic minerals in diorite porphyry; **B)** Photomicrograph in reflected light showing pyrite – chalcopyrite assemblage; **B)** XRT scanning image of the sample AS18, obtained using Orexplore XRF-XRT scanner, showing quartz (light gray) vein and the core zone from figure 2A. Fine-veinlets are also present; **D)** XRF concentration summaries data (mean values) on the segment shown in figure 2C. It is to note the high content in Cu (13092 g/t). Abbreviations: cp – chalcopyrite, py – pyrite; I – inferred content, M – measured content.

References

Abrams M, Bailey B, Tsu H, Hato M (2010). The ASTER global DEM. Photogrammetric Engineering and Remote Sensing, 76, 344-348.

Berger BR (2007). The 3D fault and vein architecture of strike-slip releasing- and restraining bends: evidence from volcanic-centre-related mineral deposits. Geological Society, London, Special Publications, 290, 447 – 471.

Burchfiel BC, Nakov R (2015). The multiply deformed foreland fold-thrust belt of the Balkan orogen, northern Bulgaria. Geosphere, 11, 463 – 490.

Cioacă M-E, Ivanov D, Iorga-Pavel A, Stoilov V, Milu V, Barbu O, Bîrgăoanu D, Costin G, Lynch EP, Högdahl K, Munteanu M (2018). Au-Ag-Bi mineralization at the Assarel porphyry copper deposit (Srednogorie metallogenic zone, Bulgaria). Geologica Balcanica, Abs. Vol., p. 276, XXI Congress of Carpathian Balkan Geological Association – CBGA 2018, Salzburg.

Drew LJ (2005). A Tectonic Model for the Spatial Occurrence of Porphyry Copper and Polymetallic Veining Deposits – Applications to Central Europe, USGS Scientific Investigations Report 2005-5287, US Department of Interior, US Geological Survey.

Gallhofer D, von Quadt A, Peytcheva I, Schmid SM, Heinrich CA (2015). Tectonic, magmatic, and metallogenic evolution of the Late Cretaceous arc in the Carpathian-Balkan orogen. Tectonics, 34, 1813 – 1836.

Iliev K, Katckov N (1990). Geological Map of Bulgaria – Panagyurishte. 1: 100 000-scale, Bulgarian Committee on Geology, Enterprise for Geophysical Studies and Geological Mapping.

Munteanu M, Cioacă M-E, Ivanov D, Milu V, Stoilov V, Costin G, Iorga-Pavel A, Lynch E, Hogdahl K (2019). Exploratory investigation of precious metals-bearing mineral assemblages from Assarel porphyry copper deposit (Srednogorie zone, Bulgaria). Goldschmidt Abstracts, Barcelona, 2019.

NASA/METI/AIST/Japan Spacesystems, and U.S./Japan ASTER Science Team. ASTER Global Digital Elevation Model (2009), distributed by NASA EOSDIS Land Processes DAAC, https://doi.org/10.5067/ASTER/ASTGTM.002

Naydenov K, Peytcheva I, von Quadt A, Sarov S, Kolcheva K, Dimov D (2013). The Maritsa strike-slip shear zone between Kostenets and Krichim towns, South Bulgaria—Structural, petrographic and isotope geochronology study. Tectonophysics, 595, 69–89.

Popov P, Strashimirov S, Popov K, Kanazirski M, Bogdanov K, Radichev R, Dimovski S, Stoykov S (2012). Geology and metallogeny of the Panagyurishte ore region, Publ. House of St. Ivan Rilski University of Mining and Geology, 228 pp (in Bulgarian, with extended resumé in English).

Richards JP (2015). Tectonic, magmatic, and metallogenic evolution of the Tethyan orogen: From subduction to collision. Ore Geology Reviews, 70, 323 – 345.

Strashimirov S, Bogdanova K, Popov K, Kehayov R (2003). Porphyry systems of the Panagyurishte ore region. Society of Economic Geologists Guidebook Series, 36, 47 – 77.

Tosdal RM, Richards JP (2001). Magmatic and structural controls on the development of porphyry Cu-Mo-Au deposits. Reviews in Economic Geology, 14, 157– 181.

Von Quadt A, Moritz R, Peytcheva I, Heinrich CA (2005). Geochronology and geodynamics of Late Cretaceous magmatism and Cu–Au mineralization in the Panagyurishte region of the Apuseni–Banat–Timok–Srednogorie belt, Bulgaria. Ore Geology Reviews, 27, 95 – 126.

4.3 Mavres Petres-Piavitsa mining area in Greece

4.3.1 Modelled volumes

Geological and geophysical modelling has been carried out on a semi-regional- to deposit scale (Fig. 4.3.1). Along the Stratoni Fault Zone (SFZ), a semi-regional scale model is presented for the Piavitsa prospect together with two deposit-scale models for the Mavres Petres (MP) and Madem Lakkos (ML) deposits. The geological model of the Piavitsa prospect measures (7 x 2.5 x 1.5 km) and was created by SGU using surface- and drill data. The geological models of the Mavres Petres (2 x 1 x 1.2 km) and Madem Lakkos (3 x 2 x 1 km) deposits are based on drill- and in-mine data only and were created by Hellas Gold and SGU. The geophysical models, all produced by SGU, cover the same areas as the geological models but with a differing depth extent.

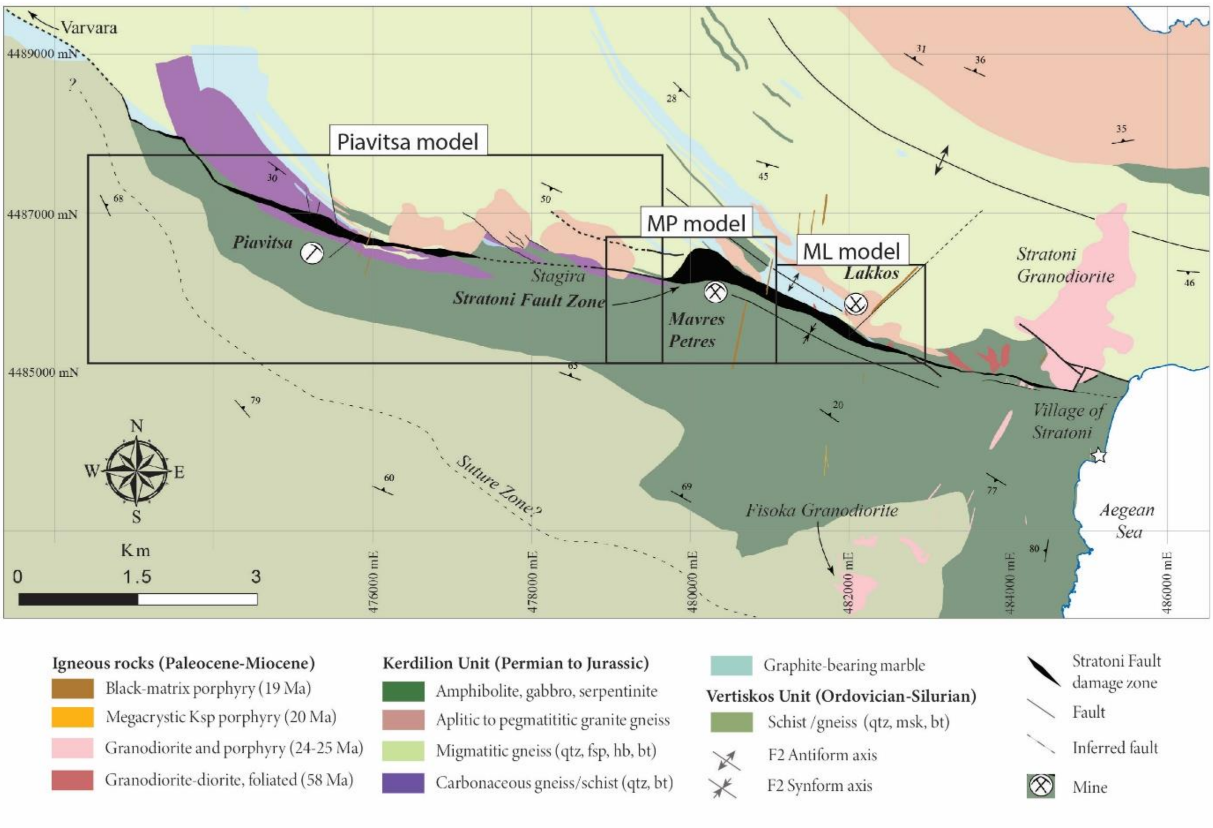

Figure 4.3.1. Geological map of the Stratoni Fault Zone outlining the modelled areas of the Piavitsa prospect, the Mavres Petres (MP) and the Madem Lakkos (ML) deposits (black polygons). Geological map modified after Siron et al. (2018).

4.3.2 Geological setting of the Stratoni fault zone

The Stratoni fault zone (SFZ) in the Kassandra mining district of northern Greece developed as a normal to trans-tensional fault during post-collisional, regional extensional tectonics since the middle Eocene (Siron et al. 2018). The south dipping fault zone extends for more than 12 km from the Aegean cost at Stratoni to the village of Varvara in the west. A continuous range of mylonitic zones to brittle faults define the fabrics of the SFZ. The SFZ is an economically important structure since it hosts and controls carbonate replacement sulfide deposits at Mavres Petres, Madem Lakkos and the prospect at Piavitsa (Au-bearing quartz-rhodochrosite vein breccia) (e.g. Arvanitidis et al. 2015b). Ore formation was most likely a response to the multiple extensional episodes triggering several pulses of magmatism and hydrothermal fluid flow. On a semi-regional scale, orebody location and morphology were governed by the intersections of pre-existing ductile fabrics with extensional mylonites and semi-brittle shear zones as well as the presence of marble lenses (Siron et al. 2018).

In the literature, the SFZ has previously been interpreted as the tectonic boundary between the Kerdillion unit (Rhodope metamorphic complex) to the north and the Vertiskos unit (Serbo-Macedonian massif) to the south (e.g. Kockel et al. 1971). More recently, however, Siron et al. (2018) interpret this boundary as an older structure and not a detachment. According to Siron et al. (2018), the Stratoni fault zone postdates regional contractional deformation (D1 to D3) and peak metamorphic conditions, which produced the penetrative tectonic fabrics and folding patterns observed in most rocks in the region. For a detailed description on the deformation events and mineralizations throughout the region the reader is referred to Siron et al. (2018) and references therein as well as to X-Mine delivery report D1-1. A short summary on the geology of the Stratoni fault zone and its direct surrounding is provided below and largely based on Siron et al. (2018).

4.3.2.1 The footwall of the Stratoni fault zone

The footwall of the Stratoni fault zone is dominated by gneisses, marbles and mafic rocks of the Kerdillion unit (Fig. 4.3.1). A compositional banding is often well preserved and transposed into a penetrative S1 gneissosity consisting of peak amphibolite-facies minerals (hornblende-biotite-plagioclase) and feldspathic mineral segregations. In marble, the S1 foliation is often defined by aligned graphite flakes. Shear sense indicators show predominantly top-to-the-northeast sense of shear of S1 foliation (Kilias et al. 1999). Directly north of the Stratoni fault zone, the S1 foliation is folded along upright WNW-ESE trending F2 folds with a gentle plunge towards the east-southeast. F2 folds in outcrop verge either northeast or southwest and are associated with an S2 ductile foliation dipping gently towards the south-southeast. The S2 fabric is composed of realigned or newly grown phyllosilicate minerals during upper greenschist to lower amphibolite facies metamorphism. Deformation during D3 is observed in the marbles as a pressure solution cleavage and as a spaced cleavage in the mica-poor granitic gneiss. Haines (1998) described from underground observations in the Madem Lakkos mine a south dipping mylonite zone (1.5 m thick) located in the footwall 200 meters below the

Stratoni fault zone. The mylonite zone postdate peak metamorphic fabrics (S1, S2) and has been interpreted as a reverse shear accommodating top-to-the-north-northeast movements. Reverse faulting was probably imbricating marble and granite gneiss towards the north-northeast and outlasted S2 folding. Several semi-brittle to brittle faults occur in the footwall that merge into or intersect the Stratoni fault zone. The largest one in the study area is the NW-dipping Vathilakkos fault, which intersects the Stratoni fault zone at, and probably partly postdates, the Madem Lakkos deposit (Haines 1998).

4.3.2.2 The Stratoni fault zone

The internal structure of the Stratoni fault zone includes slivers of all adjacent rock types. Structurally, the SFZ represents a damage zone containing multiple anastomosing mylonitic shear zones and faults of various width and length. The individual deformation zones exploit particularly the graphitic quartz-biotite gneiss and schist layers. The SSW-dipping mylonitic shear zones (1-2 meters in width) define the earliest stages of extension and formed at lower amphibolite metamorphic conditions (Haines, 1998). The pre-existing S1 and S2 foliations are commonly dragged into near parallelism with the shear zones, whereas fracturing and brecciation is more common between the shear zones. Semi-brittle faults overprint the ductile shear zones and typically consist of a foliated gouge enriched with carbonaceous material. Mineralized semi-brittle faults are generally altered into hydrothermal muscovite, Fe- and Mg-rich carbonate and fine-grained pyrite ± galena-sphalerite-arsenopyrite. The semi-brittle faults are in turn overprinted by veins and cataclastic fault breccias cemented by hydrothermal rhodochrosite ± rhodonite. These post mineral faults typically strike oblique to the earlier shear fabric, but in general do not displace principal fault strands. In terms of fault kinematics, the mylonitic shear zones, semi-brittle and brittle faults are all displaying normal top-to-the-south-southwest sense of shear.

4.2.2.2 The hanging-wall of the Stratoni fault zone

Directly south of the Stratoni fault zone, the hanging-wall is composed of middle Jurassic amphibolites of ophiolitic origin. The southwestern part of the study area is dominated by schists and gneisses of the Vertiskos unit. The mafic hanging-wall rocks contain a penetrative S1 foliation striking west-northwest and dipping mainly to the north-northeast, which is discordant to the S-dipping Stratoni fault zone. The rocks are well foliated and boudins of pyroxenite within amphibolite record a high degree of D1 strain. South of the study area, S1 becomes south to southwest dipping before entering into the Skouries area, defining a large anticlinorium. D2 deformation is best developed in the metapelitic layers of the Vertiskos unit as a penetrative crenulation cleavage that dips moderately to the south. There is no evidence for post-D2 folding in the hanging-wall except for some kink-style folds in the Skouries area, associated with D3 deformation.

4.3.3 Used datasets for model building

Input data for the geological 3D semi-regional model of the Piavitsa prospect included the geological map, structural measurements (*c.* 150) and drill data from 155 holes. The used geological map of the Stratoni fault zone has been published by Siron et al. (2018) and is a modification from an earlier version by Kockel et al. (1971) (Fig. 4.3.2). Structural measurements were collected by Chris Siron and a few more were collected during the X-Mine project (see also X-Mine deliverable D1-1) (Fig. 4.3.3). The measurements used for the modelling represent strike-dip orientations of S1, S2 and fault planes. The orientations of fault planes located within the mapped Stratoni fault zone have been used to constrain the dip of the main fault zone (see following section). Subsurface constraints from drilling were derived from several exploration drilling campaigns by Hellas Gold Exploration (Fig. 4.3.4), which resulted in initial resource estimation of 1.9 Moz at 5.7 g/t Au (https://www.eldoradogold.com). Approximately half of the modelled area has been drilled with a strong clustering along the Stratoni fault zone. Most drill holes plunge towards the north-northeast reaching a maximum depth of 600 meters below the surface level. The deposit-scale models are primarily based on subsurface data from excessive drilling (1256 holes for MP, 1834 holes for ML) and in-mine observations by Hellas Gold (Fig. 4.3.5).

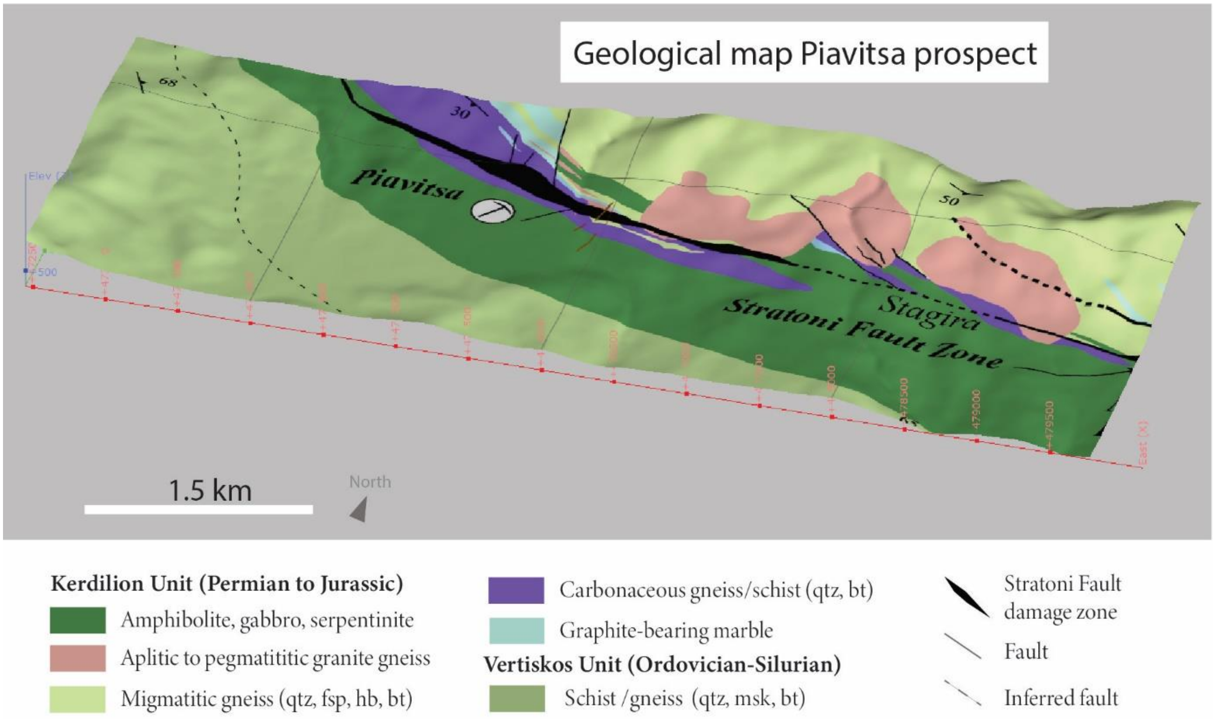

Figure 4.3.2. The geological map of the Piavitsa prospect provided surface constraints to the semi-regional 3D geological model of the same area (modified after Siron et al. 2018).

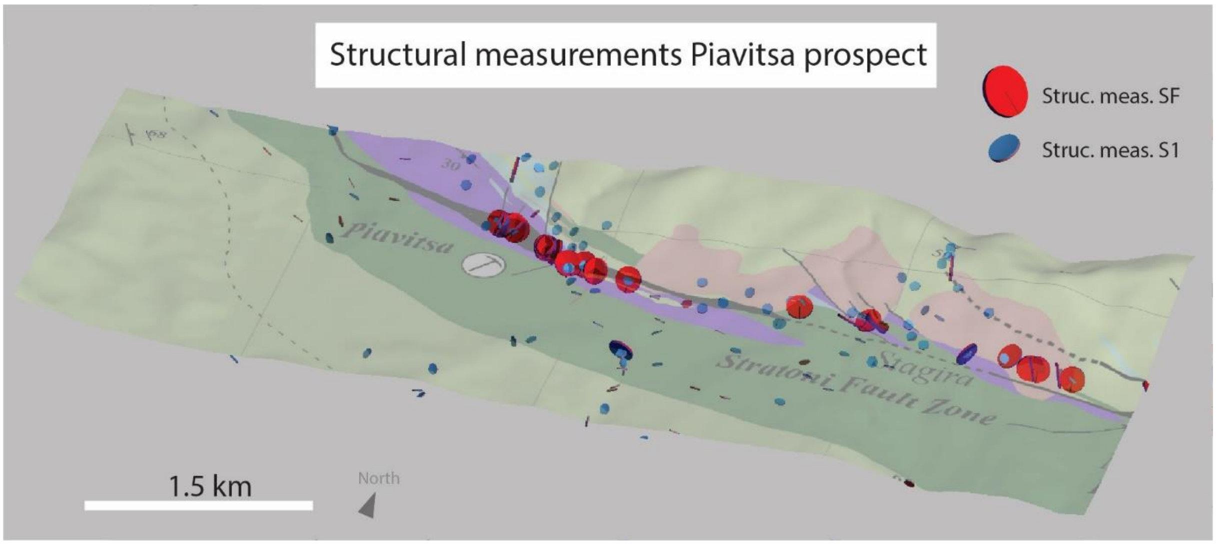

Fig. 4.3.3. Structural data used as input for the semi-regional geological model of the Piavitsa prospect.

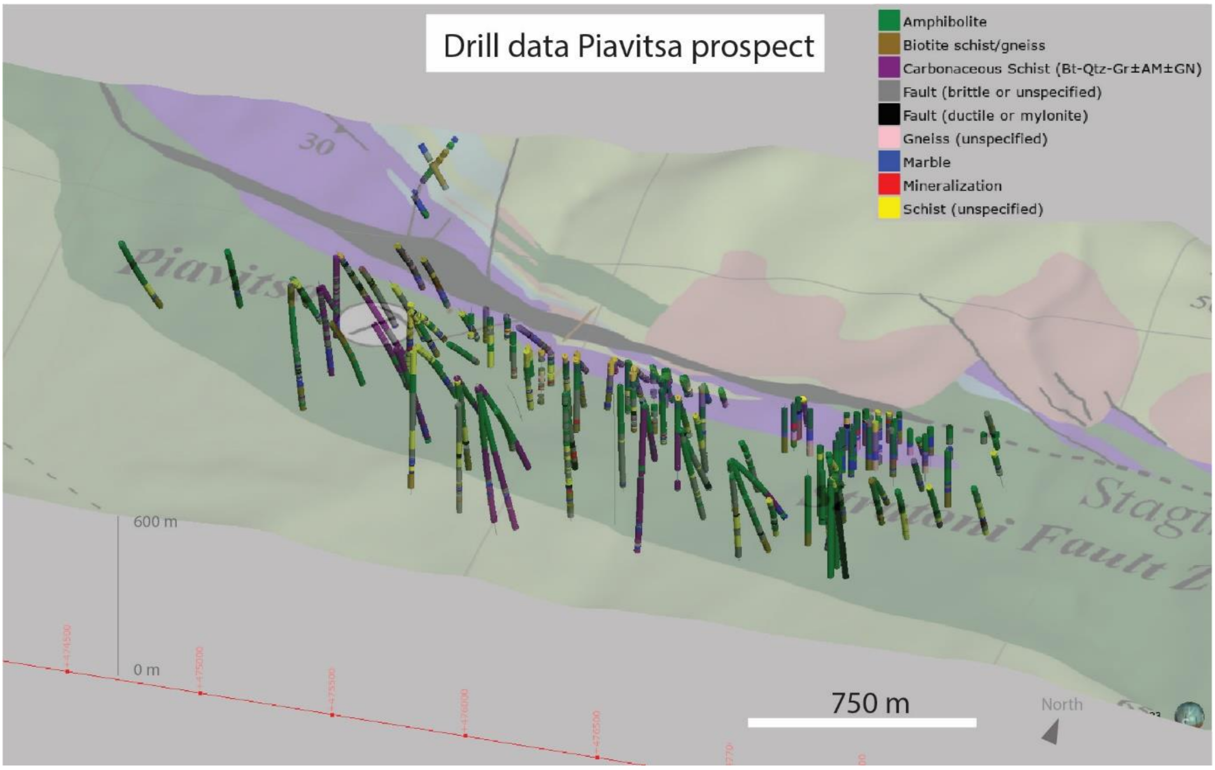

Figure 4.3.4. Drill data from Hellas Gold has been used as subsurface constraints in the semi-regional geological model of the Piavitsa prospect. The displayed lithology is based on a simplified composite drill log.

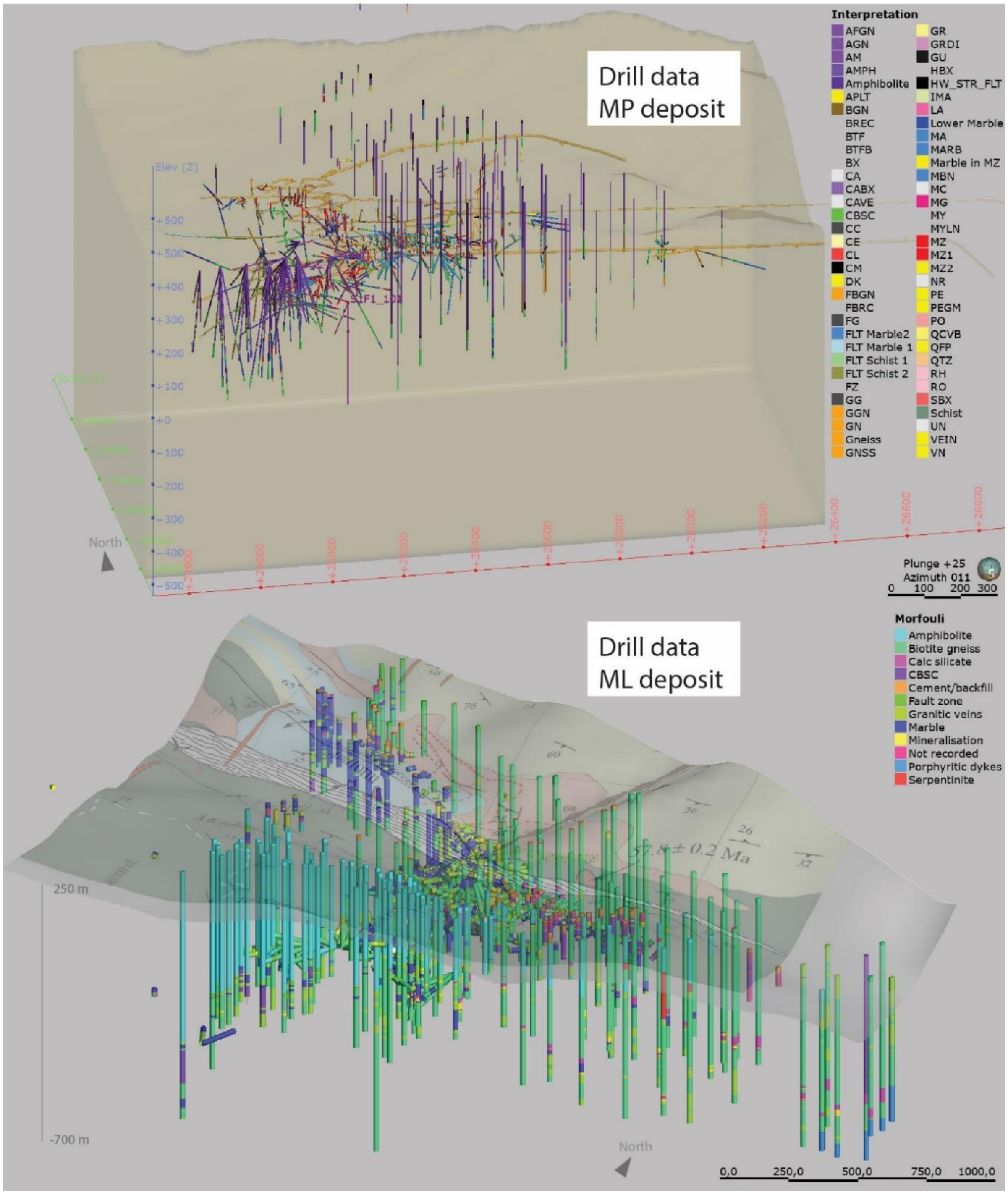

Figure 4.3.5. Drill data from the Mavres Petres (MP, top) and Madem Lakkos (ML, below) deposits and in-mine observations were used as input for the deposit-scale models. The logging codes displayed in the legends are from Hellas Gold. Additional displayed features are the in-mine infrastructure of the MP deposit in yellow and the local geological map from Siron et al. (2018) for the ML deposit.

4.3.3.1 Geophysical and petrophysical data

Geophysics provides a set of tools to aid mapping of geological structures and lithological variations reasonably dense across an area and through a volume, and to gain valuable information of the physical properties of rocks at the surface as well as in deeper parts of the earth that cannot be reached directly. Petrophysical measurements provide the vital link between the measured geophysical response and the actual bedrock material and helps to increase the precision and accuracy in modeling and interpretation of geophysical data.

A helicopter-borne geophysical survey was conducted by Fugro Airborne Surveys Limited over the Stratoni fault region, including the mineralized regions at Madem Lakkos, Mavres Petres and Piavitsa. High-quality electromagnetic and magnetic data were acquired using a towed-bird system, and a spectrometer mounted in the helicopter simultaneously provided radiometric data, all with a sampling frequency of 10 Hz (c. 3.3 m at 120 km/h) along N-S oriented flight lines at 100 m separation. For a more detailed summary of the geophysical survey, the reader is referred to Deliverable D1-1.

As part of the X-Mine project, 17 drill core samples from the Mavres Petres deposit and Piavitsa prospect and 11 bedrock samples from outcrops along the Stratoni Fault Zone were collected during 2018. An additional 10 samples were obtained during spring 2019 from drill core targeting the mineralized zone specifically, that had been scanned using the core scanner. The density, magnetic volume susceptibility and natural remanent magnetization (NRM) of these 38 samples were measured at the petrophysical laboratory of SGU (Appendix table 4.3.1). An additional 19 samples are currently awaiting petrophysical analysis at SGU. The electrical properties (including resistance and resistivity) were measured on 97 drill core samples from Mavres Petres by Hellas Gold (Appendix table 4.3.2).

Results show that the mineralization stands out clearly in its much higher density (4399 kg/m^3, averaged on 10 samples) and lower electrical resistivity (509 Ωm, averaged on 12 samples) as compared with rock outside of the mineralized zones which is dominated by gneiss, schist, marble and amphibolite (mean density of 2693 kg/m^3 on 18 samples and mean resistivity of 3714 Ωm on 40 samples) (Fig. 4.3.6). In terms of magnetic susceptibility, the samples indicate little or no contrast between the mineralization and surrounding rocks of gneiss, schist and amphibolite (Fig. 4.3.7). The marble on the other hand appears to have anomalously low magnetic susceptibilities, with all four samples falling in the range from c. -16 to -7 µSI. The sampled fault gauge material has a lower resistivity than the surrounding rock (72.34 Ωm, averaged on 8 samples), possibly due to higher content of water or clay minerals. Note that the number of samples are few and may be indicative to a certain degree, but that more observations are needed before concrete conclusions are drawn.

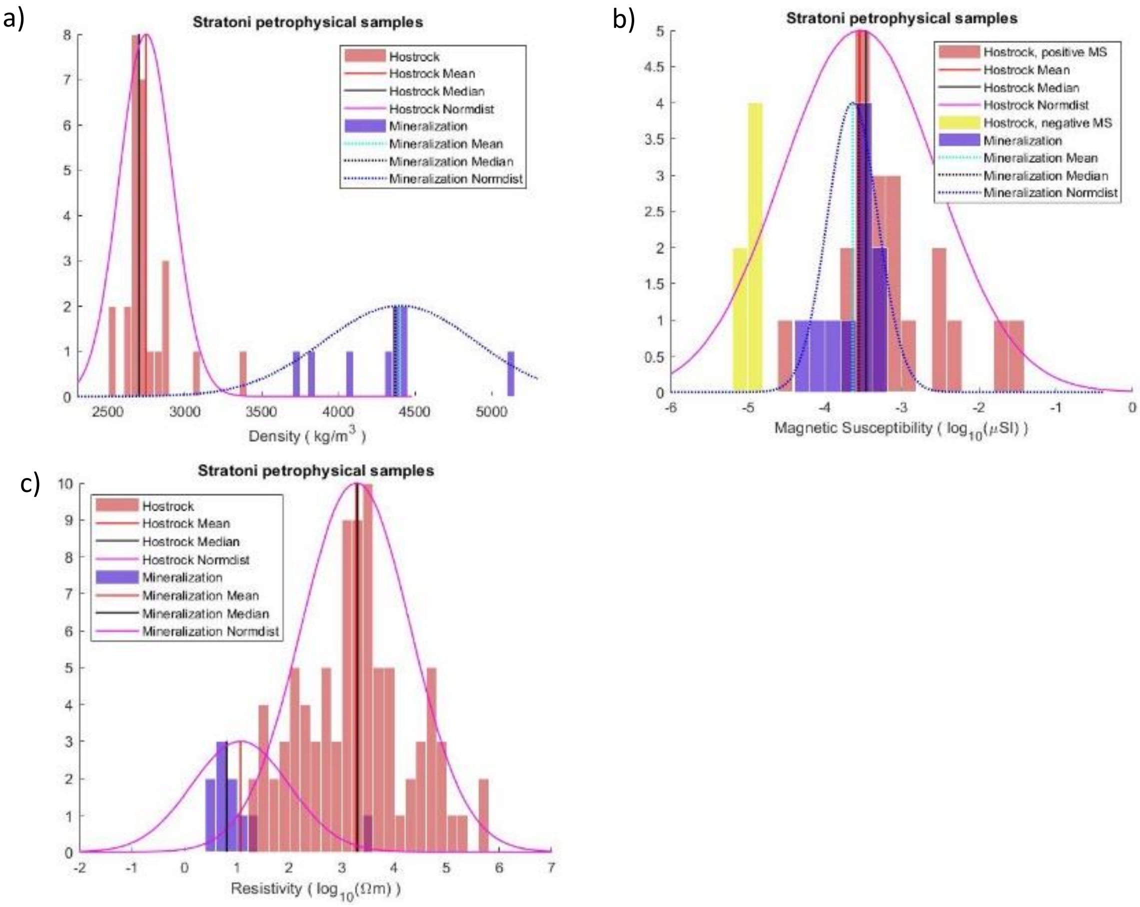

Figure 4.3.6. Histograms showing the distribution of (a) density, (b) magnetic susceptibility and (c) electrical resistivity measured on samples from the Stratoni Fault area. “Host-rock” comprise the full suite of lithologies adjacent to the mineralization, including gneiss, amphibolite, carbonate-schist and marble. All samples of marble have negative magnetic susceptibility; only one sample with negative magnetic susceptibility is not marble.

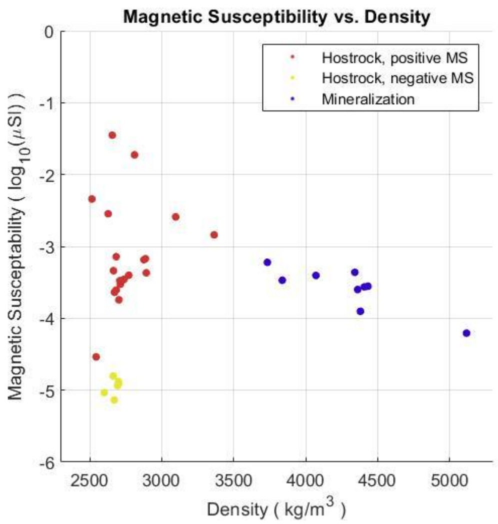

Figure 4.3.7. Cross-plot distribution of density versus magnetic susceptibility measured on samples from the Stratoni Fault area. Host-rock comprise the full suite of lithologies, including gneiss, amphibolite, carbonate-schist and marble. All samples of marble have negative magnetic susceptibility; only one sample with negative magnetic susceptibility is not marble. The mineralization is distinct in density and the marble is distinct in terms of magnetic susceptibility.

4.3.4 Modelling Methodology

4.3.4.1 Semi-regional scale: Piavitsa prospect

Modelling on a semi-regional scale focused on the Piavitsa polymetallic structural controlled carbonate replacement prospect located along the western segment of the Stratoni fault zone. The northern and southern map traces defining the SFZ damage zone were digitized to define the model's main fault blocks (Fig. 4.3.8). As such, three main fault blocks were created from north to south: the footwall-, the SFZ- and the hanging-wall block. The SFZ-block represents the fault damage zone, which has been extrapolated to depth using constraints from drill data and structural measurements from the surface. Depth traces were created by 2D correlation between drill hole markers representing semi-brittle zones and brittle faults. This procedure has been executed manually along seven profiles oriented perpendicular to the SFZ. (Fig. 4.3.8a). In order to produce a general and consistent outline of the SFZ at depth, not all the individual shear zones or faults were included in the 2D correlations. As faults and shear zones do occur within both the footwall and hanging wall, the real extent of the SFZ remains uncertain based on the available data (see also section 4.3.2). Our interpretation should therefore be considered as a "more or less" model guided mainly by mapped surface trace, structural measurements, drill hole markers and by the assumption of a rather constant fault thickness in areas with sparse data. At increasing depths, outside the drilling area, the SFZ has been interpreted with a high uncertainty as a listric fault zone dipping shallowly to the south-southeast. Subsequently, the depth traces in combination with the surface map traces formed a frame to the modelled surfaces along the contacts with the footwall and hanging-wall fault blocks (Fig. 4.3.8b-c, Fig. 4.3.9). The lithology in each fault block was modelled separately according to drill- and surface data. Within the hanging-wall- and footwall blocks, the map traces of lithological contacts were digitized from the geological map and extrapolated downwards at dips constrained by nearby structural measurements. The produced surfaces were then modified by subsurface constraints derived from drill data. Within the SFZ-block, the main lithologies have been modelled as "veins" with pinch outs to allow for complex shapes and lenses enveloped by other lithologies, faults or shear zones. Subsurface interpretations derived from geophysical modelling 3D inversion were not implemented in the geological modelling at this stage.

4.3.4.2 Deposit scale: Mavres Petres and Madem Lakkos

Modelling on a deposit scale was conducted for the polymetallic Au-Ag-Pb-Zn structural controlled carbonate replacement deposits of Mavres Petres (MP) and Madem Lakkos deposits (ML). The MP deposit model is based on a large number of drill holes (exploration and resource conversion) and in-mine observations and was produced by Hellas Gold Exploration. The model is regularly updated and modified as mining and near-mine exploration is ongoing at the time of writing. Like the semi-regional scale model of Piavitsa, the MP model is intersected by the mineralized Stratoni fault zone dividing the model space from north to south into a footwall-, fault zone-, and hanging-wall block. Lenses of massive sulfide mineralization and marble are hosted mainly by the fault zone block and were modeled in Leapfrog Geo as veins with the option to pinch out. To the east-southeast along strike, the ML deposit model has been modelled using a large number of mainly vertically oriented drillholes intersecting the footwall-, fault zone- and hanging wall blocks to a depth of 950 meters below the surface. Drilling revealed several clusters of massive sulfide located in the SFZ-block as well as in the footwall block. The clusters located in the footwall block were modelled separately as closed surfaces in SKUA-GOCAD using multiple grip-frames for each cluster. As such, outliers of mineralization between the clusters were excluded and surface intersections were avoided by adapting a simple geometry. Subsequently, the produced ore shells were imported into Leapfrog Geo as meshes and a geological model, including the marble unit, was created. Well zones of intersected mineralization located in the SFZ-block have been modelled as a single vein with pinch outs.

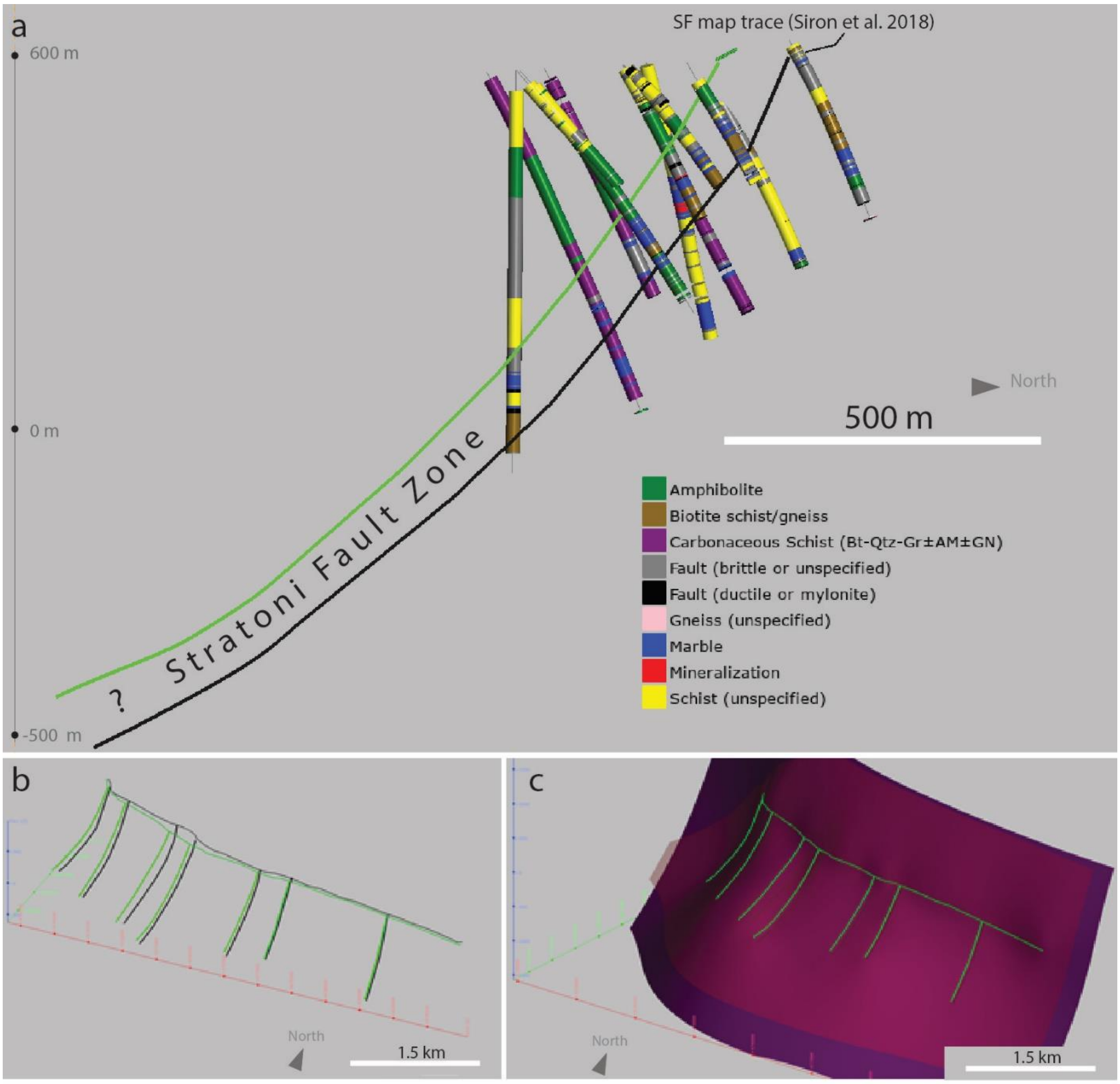

Figure 4.3.8. a) The outline of the Stratoni fault zone at depth was modelled by roughly correlating drill markers corresponding to fault/shear zones (see text for more detail). b) Depth traces were extracted from seven profiles perpendicular to the SFZ. c) Contact surfaces with the hanging-wall and footwall were modelled using the map traces and depth traces as a frame.

4.3.4.3 Geophysical models

Inverse modelling of geophysical data is a numerically iterative procedure of finding a subsurface model that satisfies the measured geophysical data to within a certain error-threshold. The inherent limitations in the resolution of geophysical data, however, results in a non-uniqueness issue where an infinite number of subsurface models exist that can satisfy observed data. Therefore, aside from high-quality data, inversion also requires various regularizations, some of which are mathematical in nature (e.g. model geometry and resolution, smoothness, required accuracy etc.), to be able to resolve a geologically viable model. Moreover, a-priori information mainly connected to the geology (e.g. the geometry of known surface and structures, maximum and minimum bounds of physical properties etc.) may be utilized to limit the number of possible solutions. With respect to the latter, high-quality and statistically sound petrophysical data is vital. An additional challenge lies in the highly detailed lithological information from boreholes that must be simplified to match the resolution of the geophysical inversion (on the order of meters to 10's of meters) and to a smaller number of representative lithological groups without losing vital geological information.

The magnetic and electromagnetic data acquired by helicopter are both suitable for inverse modelling in the area along the fault that encompasses the Mavres Petres and Madem Lakkos deposits and the Piavitsa prospect and may allow correlation between the mining areas. In terms of magnetic susceptibility, petrophysics show that the mineralization, as found at Mavres Petres and Piavitsa, will most likely not stand out in in an inversion of magnetic data (see also section 4.3.3.1). The marble, on the other hand, which in many cases is associated with the mineralization, has distinctly lower magnetic susceptibility than other lithologies and may give rise to negative magnetic anomalies. Additionally, the amphibolite unit in the hanging-wall is known to locally host pyroxenite and serpentinite of higher magnetic susceptibility. Inversion of magnetic data could thus possibly indicate the location of such bodies of interest for its resource potential. Inversion of magnetic data has been performed using VOXI extension of the Geosoft Oasis Montaj™ software.

The VOXI extension for inverting Electromagnetic data is currently under development. A test license for VOXI EM inversion was obtained for the sake of inverse modeling within the X-Mine project. It is a 1D inversion followed by 3D interpolation and has limited resolution and accuracy as compared to a full 3D inversion algorithm. Nevertheless, reasonable inverse models of electrical conductivity were obtained that may be useful in aiding 3D geological modeling on the mining to regional scale. Anomalies indicating high conductivity in the shallow EM models may be linked to mineralization, as seen in the petrophysical results above, but also to water and/or clay content in the near surface sediments or fractures.

Petrophysical measurements on lithologies not yet represented in the data, as well as geological and geometric constraints from boreholes and validated formations in the geological models, could be incorporated to potentially improve the accuracy of the inverse modelling.

4.3.5 Modelling results

4.2.5.1 Semi-regional scale: Piavitsa prospect

The 3D geological model of the Piavitsa prospect consists of three main fault blocks: The footwall block, the SFZ-block and the hanging-wall block (Figs. 4.3.9, 4.3.10). The footwall in the north largely consists of gneisses and schists from the Kerdillion Unit, which were modelled as the “background lithology” (Fig. 4.3.11). As such, the map-scale folding pattern as portrayed on the geological maps from Siron et al (2018) and Kockel et al. (1971) has not been modelled here in detail. However, the southern limb of an upright to inclined anticline is represented in the model by the northward deflection of the marble unit with respect to the SFZ. Two parallel layers of marble separated by gneisses and schists are dipping towards the south in the eastern part of the model but transitioning toward a southeast dip further towards the west. Here, the marble layers strike oblique to the SFZ and deflect from the fault zone towards the north-northwest. The carbonaceous gneiss/schist unit and the granitic gneiss unit were modelled as “intrusions-type” bodies. The latter was only constrained by surface map traces. At depth, the granitic gneisses have been interpreted as ellipsoids plunging approximately 50° towards the southeast subparallel to the SFZ. Their depth extend is limited to 250 meters below the surface, but this is highly uncertain. The modelled bodies enclosing the carbonaceous schists do include constraints from drill data and have a somewhat more complex shape. Several lenses of schist occur along the contact with the SFZ-block and their pancake-like geometries may reflect an increase in strain along the contact. A single lens of mineralization occurs in the footwall, which is an extension of a larger lens located in the SFZ-block.

The SFZ-block represents the damage zone of the Stratoni fault zone and includes besides fault rocks also lenses of marble, amphibolite, mineralization, gneiss/schist or a composite of those (Fig. 4.3.11). Near the surface, the block dips 70 to 80° towards the south-southeast, but dips shallow to 45-50° at around 200-300 meters below surface level. The thickness of the SFZ-block varies along strike and with depth. Directly west of the village of Stagira, the thickness is only 60 m at the surface but increasing towards 110 meters at depth. The maximum thickness, however, occurs around Piavitsa where the SFZ-blocks measures 250 meters in width at the surface as well as at depth. This is also the region were single gouge zones reach a thickness up to 150 meters hosting lenses of mineralization with a thickness of 30 meters and a diameter of 200 meters. The largest continuous lens of mineralization occurs in the eastern part of Piavitsa and measurers 900 meters along dip, 310 meters along strike and reaches a thickness up to 7 meters. The marble unit appears mostly as a rather continuous layer with thicknesses varying between 60 and 100 meters, but with a maximum thickness of 200 meters at Piavitsa. Combining the SFZ-block with the results of the 3D inversion of the magnetic susceptibility in 2D sections (Fig. 4.3.12) shows that the SFZ-block has no significant magnetic characteristics associated with the fault zone. Similarly, overlying the geologically modelled SFZ block on the EM profile reveals that the SFZ-block does not stand out in the EM-model as a distinctive feature (Fig. 4.3.13). A southward dipping trend can be interpreted from the EM-model albeit with a gentle dip of 30°. It may well be that this dipping trend reflects the architecture of the SFZ at depth, but further investigation and an integrated modelling approach between geological- and geophysical modelling are needed to support this.

The modelled hanging wall block consists mainly of schists of the Vertiskos Unit, amphibolite and some carbonaceous schist mainly along the contact with the SFZ block (Fig. 4.3.11). The boundary between the Vertiskos unit and the amphibolites is highly uncertain at depth and is only based on sparse structural measurements at the surface. Opposing dips suggest a gently east-southeast plunging synform within the amphibolites trending parallel to the SFZ. Results from the magnetic inversion reveal a hanging wall block characterized by regions of relatively high magnetic susceptibility located both in the schists of the Vertiskos Unit and amphibolite unit. The high anomaly zones reveal a predominant plunge towards the south and a folding pattern may be apparent from profiles 1 and 4. However, the poor constraints of the magnetic inversions should be bared in mind and no solid lines should be inferred based on solely this model.

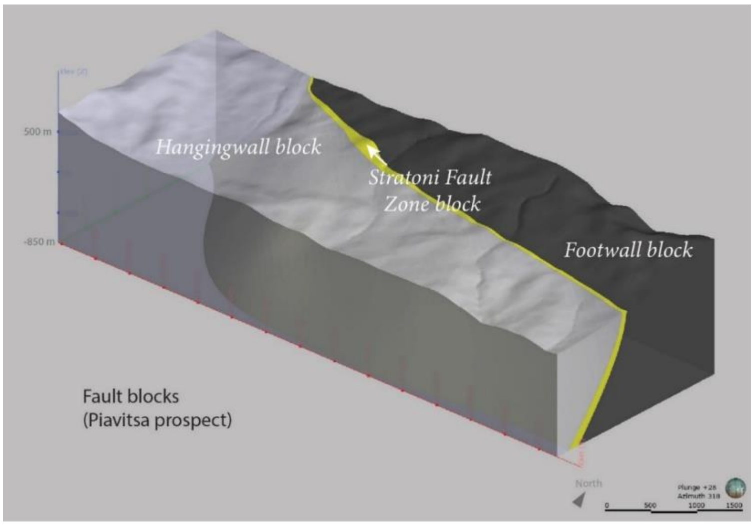

Fig. 4.3.9. Fault block model of the Piavitsa prospect.

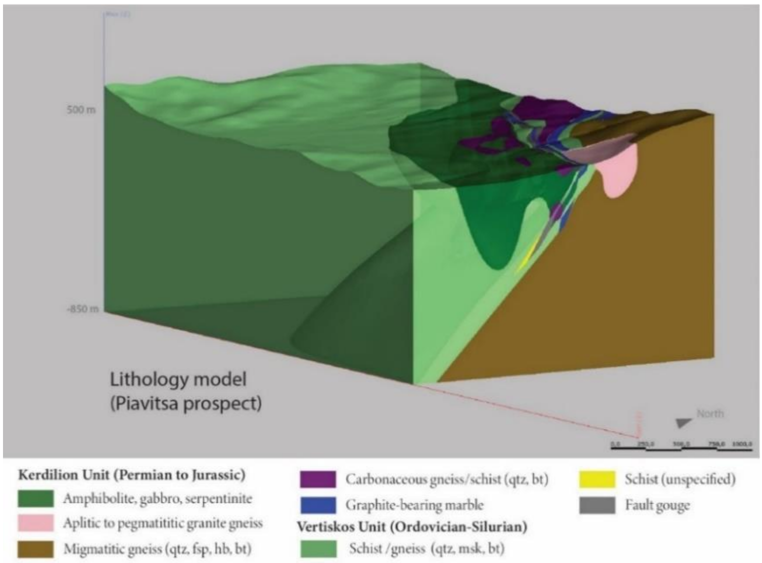

Fig. 4.3.10. Semi-regional 3D lithology model of the Piavitsa prospect.

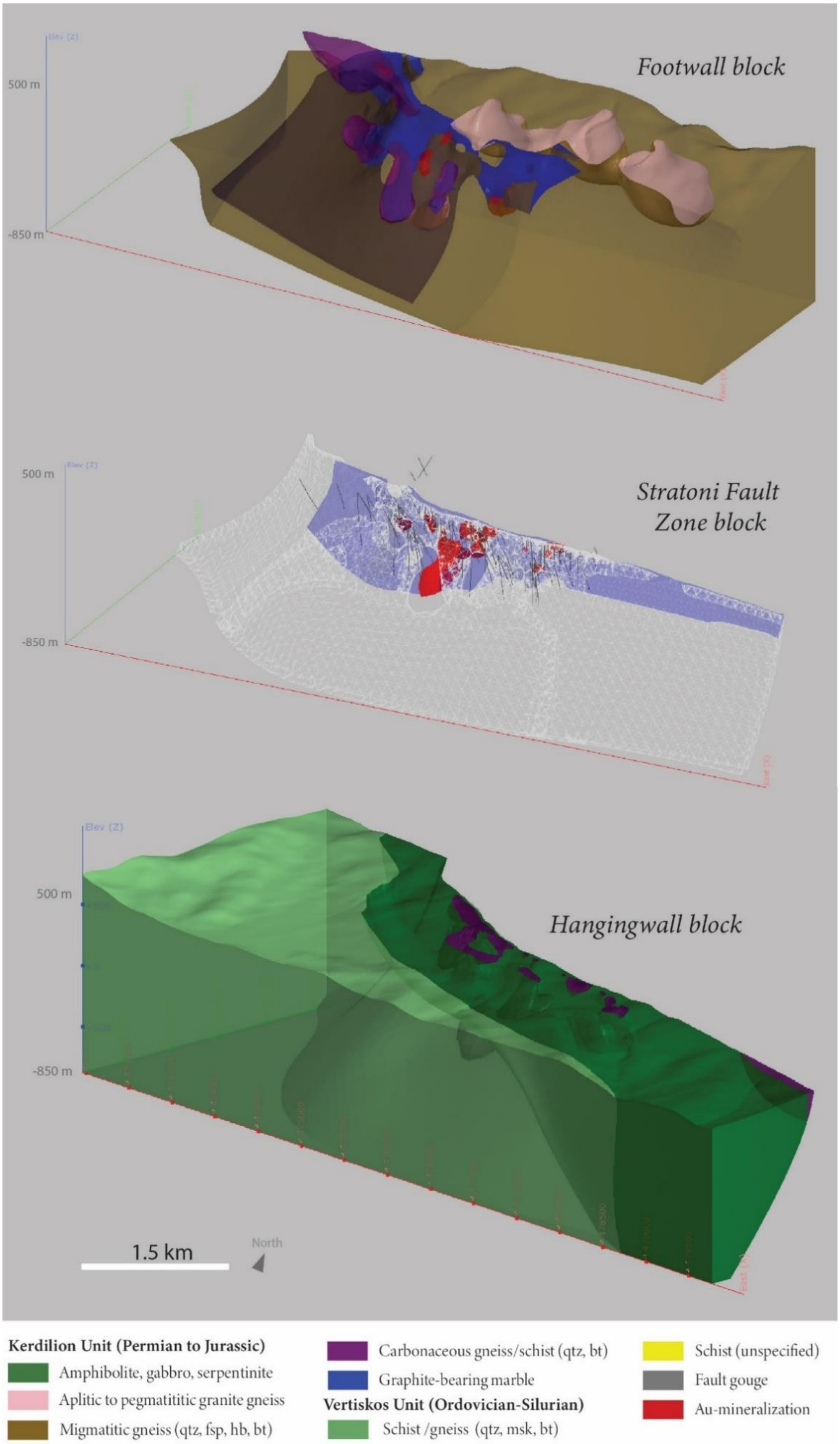

Fig. 4.3.11. Lithological units modelled within each fault block (Piavitsa prospect).

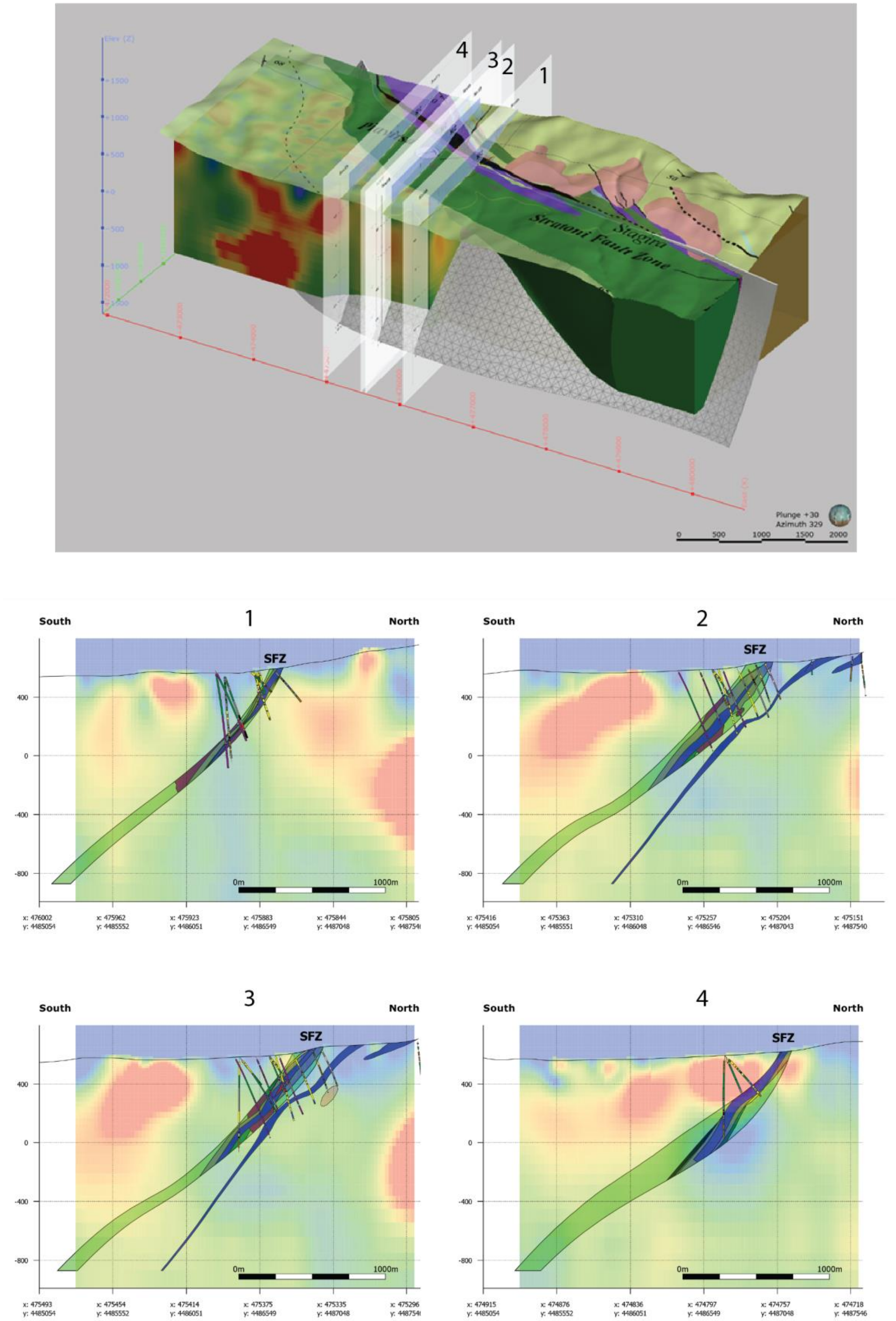

Fig. 4.3.12. Magnetic inversion model of the Piavitsa prospect on a semi-regional scale complemented by the geological model to the east (top view) Gray mesh corresponds to SFZ. The lower pictures show cross-sections combination with the modelled lithology within the SFZ fault block. See previous figures for legend on lithology. Geophysics: red and blue colors refer to high and low magnetic susceptibility, respectively.

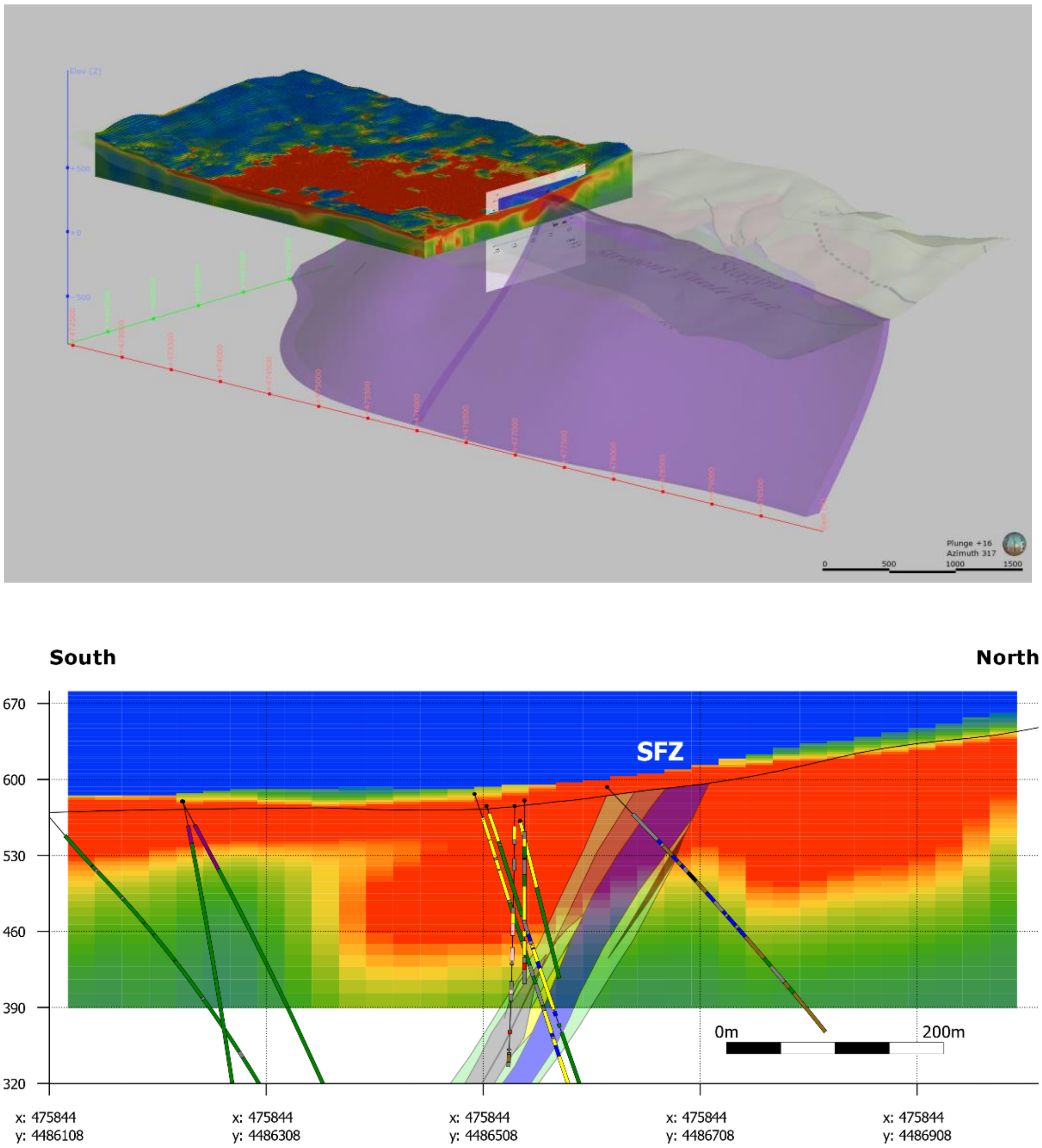

Fig. 4.3.13. Results of the EM inversion in the Piavitsa prospect area. Top view: The EM model covers the same area as the magnetic inversion model but has a limited depth extend to ±200 meters. Purple surface corresponds to the Stratoni fault zone. Lower view: Cross-section along the central part of section 1 (see Fig. 4.13) and location 1 (see previous figure) showing conductivity (rainbow colors), drilled lithology and the interpreted lithology within the SFZ fault block. Notice the gentle dip to south of the highly conductive region in the center (red color) relative to the steeply dipping SFZ (constrained by drilling and surface geology). Red and green colors correspond to high- and low conductivity, respectively.

4.3.5.2 Deposit scale: Mavres Petres

The 3D geological model of the Mavres Petres deposit reveals a similar architecture as the Piavitsa prospect model with a footwall comprised of gneiss/schist, an amphibolite dominated hanging-wall and the SFZ-block including fault rocks, marbles and massive sulfide mineralization (Fig. 4.3.14). In contrast to the semi-regional model to the west, the Mavres Petres models displays a stratification of the SFZ-block with carbonaceous schist at the base, structurally overlain by marble, mineralization and fault gouge at the top. As such, the SFZ may be interpreted as a wide semi-brittle shear zone, which is partly overprinted by a more discrete, mineralized, semi-brittle to brittle fault zone. The 3D inversions of the magnetic and EM data show a southward-dipping trend of high- and low anomaly zones. Similarly, to the west, the amphibolite is characterized by 100 to 500-meter-sized areas of high magnetic susceptibility with various geometries. In addition, the EM model reveals two parallel zones of highly conductive material dipping steeply towards the south. These zones may well coincide with late stage “epithermal” looking veins or fault gouge (see also section 4.3.3.1).

4.3.5.3 Deposit scale: Madem Lakkos

The 3D geological model of the Madem Lakkos deposit portrays a gentle east-southeast plunging anticline of marble in the footwall oriented oblique to - and partly intersected by - the SFZ to the south (Fig. 4.3.15). Like the previous models, the hanging-wall consists mainly of mafic rocks (amphibolite and serpentinites) with a large range of magnetic susceptibilities. Mineralization occurs both in the footwall, where it is localized as massive sulfide lenses in the hinge zone of the main anticline, as well as in the SFZ. The ore lenses in the fold hinge zone may be bounded by N-S striking faults which caused the down-stepping pattern between the lenses in a down plunge direction. The 3D inversion of airborne magnetic data shows that some of the ore lenses hosted by the fold coincide well with areas of high magnetic susceptibility (Fig. 4.3.15). It is known from historic drilling data that the lenses of massive sulphide mineralization hosted within the east plunging marble often contain halos of strong calc-silicate alteration (magnetite-epidote-actinolite-pyrite). These alteration zones are typically domains of relatively high magnetic susceptibility.

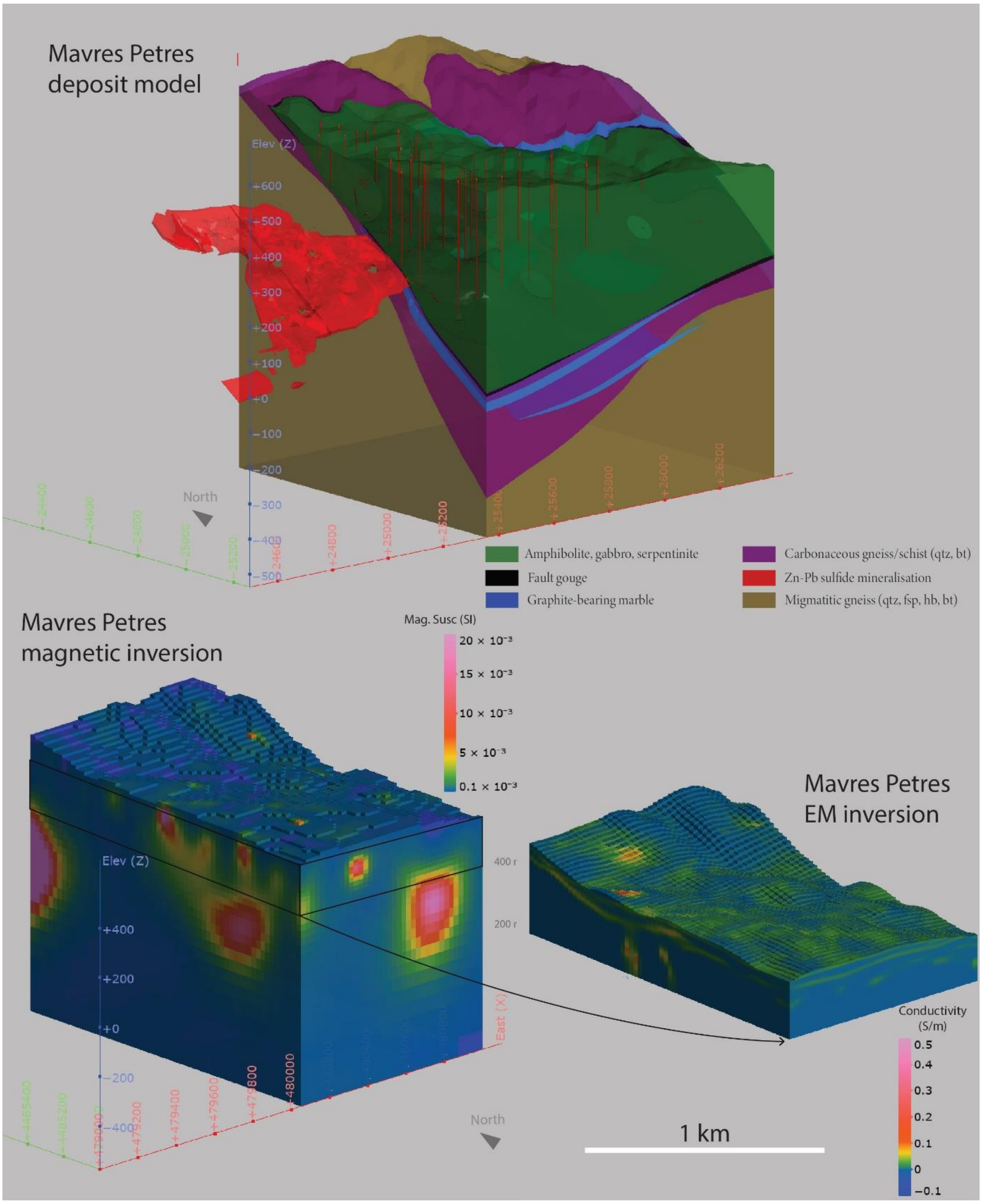

Fig. 4.3.14. Lithology model of the Mavres Petres model (top view). The ore body colored in red is unsliced. The lower figure shows the 3D magnetic inversion as a sliced block and the overlapping 3D EM inversion viewed from a similar angle.

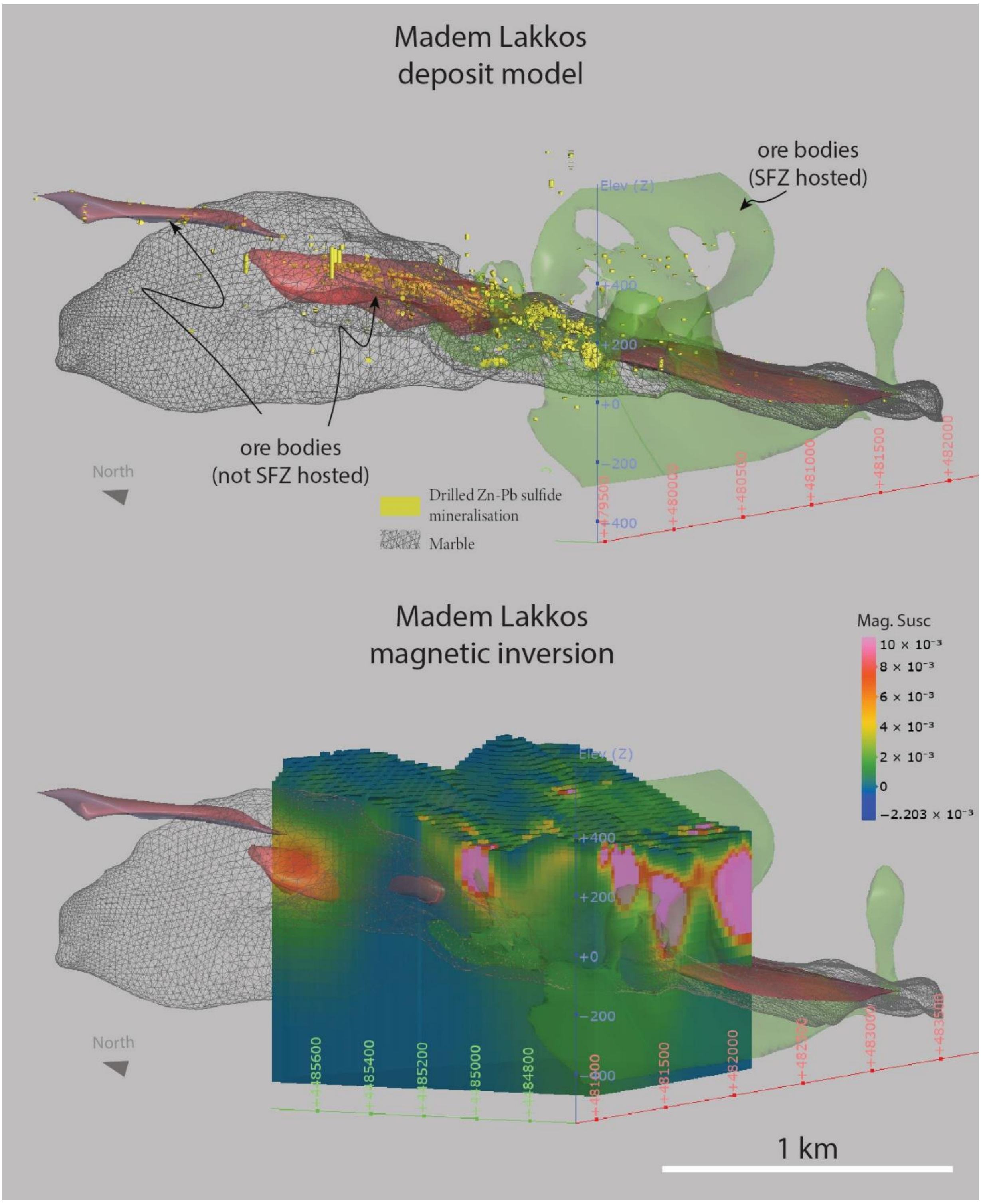

Fig. 4.3.15. Ore deposit model of Madem Lakkos based on drill- and in-mine data only. The ore bodies located in the footwall (red) were modelled separately in SKUA-GOCAD. The lower figure shows a cut-out part of the 3D magnetic inversion model (semi-transparent block model) visualized in combination with the modelled ore bodies (semi-transparent red) and marble unit (semi-transparent mesh) based on drill- and in-mine data. Magnetic susceptibility is in SI-units.

4.3.6 Geological implications and conclusions

The modelling results presented in this chapter should be treated as work in progress. Investigations and modelling are a continuous process, in particular during the remaining stage of the X-Mine project (Task 1.3), allowing for constant updates, refinements and modifications. Some concluding remarks from the current state are:

- The presented models provide a good three-dimensional overview on the spatial distribution of mineralization and their hosting lithological units along and within the Stratoni fault zone.
- The combined visualization of geological and geophysical models at various scales contributed to the characterization of the lithological units and the definition and extrapolation of lithological- and tectonic boundaries at depth.
- A real integration between geological- and geophysical models should be aimed for as well as constraining the inversion process, reducing the non-uniqueness and enhancing cross-validation between the models. To make this possible, we recommend increasing the number of measured physical rock properties and to conduct forward models enabling validation of the geological models.

4.3.7 Appendix

Appendix table 4.3.1. Density, Magnetic Susceptibility and Natural remanent magnetization (NMR) of rock samples from Mavres Petres (MP), Piavitsa (PV) and out crops long the Stratoni corridor (ELH). Measured at SGU during winter–spring 2019.

Sample code	Z above mean sea level (m)	Lithology	Density (kg/m^3)	Magnetic Susceptibility (µSI)	NRM (mA/m)
MP0777_143	106.07	Marble / carbonate in footwall	2700.22	-12.13	26.35
MP0779_112	125.17	Amphibolite	2738.96	348.72	31.09
MP0786_90	165.65	Amphibolite	2712.7	297.66	10.7
MP0787_149	104.07	Carbonaceous Schist (Bt-Qtz-Gr±AM±GN)	2672.23	230.27	45.22
MP0787_28	210.86	Amphibolite	2709.11	333.87	8.43
MP0789_76	160.29	Amphibolite	2771.77	397.24	11.27
MP0800_82	153.36	Amphibolite	2730.69	338.87	7.21
PVD124_108_45	498.14	Carbonate-altered bt schist within fault zone	2665.44	459.55	237.87
PVD124_139_00	474.08	Intense MnOx alteration affecting bt schist (giving stripped/banded or mylonitic? texture)	2684.12	246.70	79.41
PVD124_142_45	471.33	Pink rhodochrosite vein (40 cm) in rubbly fault zone w/ intense Mn-altered rock adjacent	3097.19	2580.08	122.67
PVD124_152_55	463.28	Carbonate-silica-altered bt schist	2703.07	180.75	93.58
PVD124_192_75	430.92	Foliated amphibolitic unit. Weakly carbonate +/- silica altered	2892.96	429.41	41.89
PVD124_41_42	549.95	Foliated/banded bt schist	2877.2	652.93	236.6
PVD124_50_35	543.13	Foliated amphibolite	2683.86	719.50	426.32
MP0787_69	174.96	Amphibolite	2729.86	338.69	36.06
MP0787_89	157.28	Amphibolite	2607.56	288.42	19.03
MP0780_60	207.97	Amphibolite	2704.22	285.12	14
ELH180001C	323.41	Foliated bt gneiss in SFZ footwall	2627.93	2847.68	197.2
ELH180002C	511.94	Gneissic meta-granite in SFZ footwall	2600.48	-9.26	63.72
ELH180005D	217.69	Felsic quartz porphyry dyke	2515.86	4568.27	123.36
ELH180005C	217.69	Amphibolite. Minor pyrite	2887.33	675.12	30.56
ELH180008C	0	Foliated amphibolite	2811.75	18 795 .00	1619.51
ELH180009C	330.44	Marble, north limb of Stratoni anticline	2694.18	-11.55	28.8
ELH180010B	324.77	Calc-silicate breccia (jasperoid) in NE-striking fault zone	2544.99	29.02	24.01

ELH180011D	498.37	Mn-oxide-rich gossan rock (adj to marble)	3364.39	1449.72	50.31
ELH180012C	266.59	Graphitic marble	2663.65	-15.73	15.89
ELH180014D	49.06	Stratoni granodiorite	2657.33	35 306 .66	178.84
ELH180011B	498.37	Marble	2670.75	-7.31	12.73
MP0779-167	167	Mineralization	4407.71	273.95	75.88
MP0779-163	163	Mineralization	4361.13	251.61	81.11
MP0779-178	178	Mineralization	3733.95	600.79	190.49
MP0816-139	139	Mineralization	5309.29	79.16	73.91
MP0816-135	135	Mineralization	4432.51	279.57	116.8
MP0826-209	209	Mineralization	3837.73	338.65	110.52
PV87-435	435	Mineralization	4341.44	436.07	117.57
PV87-436	436	Mineralization	4380.35	125.06	123.44
MP0794-138	138	Mineralization	5117.38	62.17	59.18
MP0794-147	147	Mineralization	4071.66	394.44	215.1

Appendix table 4.3.2. Contact resistance and resistivity of core samples from Mavres Petres. Measured at Hellas Gold in Mavres Petres during the winter of 2018–2019.

Id	Hole	Sample Depth (m)	Description	Base metals mineralization/Rodochrosite/ Graphite/Silica/Barren	Contact resistance (kΩ)	Resistivity (Ωm)
1	MP0881	18	Carbonaceous Schist (Bt-Qtz-Gr±AM±GN)	barren	6.918	411.174
2	MP0881	18.6	Carbonaceous Schist (Bt-Qtz-Gr±AM±GN)	sulphides - graphite	8.329	164.166
3	MP0881	59.9	QCVB	sulphides - graphite	192.923	4374.804
4	MP0881	44.4	mineralized MARBLE	sulphides - graphite	58.058	1995.375
5	MP0881	69.8	mineralized MARBLE/sf	sulphides	2.534	105.119
6	MP0881	73.9	mg/sf	sulphides	1.573	62.725
7	MP0881	74.8	mg/sf	sulphides	4.225	111.772
8	MP0879	18.6	amphibolite	barren	84.647	2355.462
9	MP0879	26	MARBLE	barren	12190.341	196949.917
10	MP0879	41.1	MARBLE	graphite	13.437	303.352
11	MP0879	44.4	MARBLE	minor sulphides	8.915	236.64
12	MP0879	57.3	MG	sulphides	2.109	67.588
13	MP0879	60.5	MG	graphite	0.412	23.922
14	MP0879	88.5	mineralized MARBLE	sulphides	0.273	22.836
15	MP0880	53.6	amphibolite	barren	60.848	2802.369
16	MP0880	59.8	fault gouge/ amphibolite	barren	1.182	35.342
17	MP0880	97.8	fault gouge/ amphibolite	barren	0.903	29.6
18	MP0847	37.2	amphibolite	barren	3.534	412.318
19	MP0847	88.4	amphibolite	barren	10.137	281.865
20	MP0847	126.4	amphibolite	barren	39.389	2412.681
21	MP0847	172.6	amphibolite	barren	21.37	974.934
22	MP0847	210.1	amphibolite	strong CHS alteration, very fine sulphides	211.772	3715.855

23	MP0847	239	mineralization	massive sulphides	0.475	10.586
24	MP0847	246.5	mineralization	massive sulphides	0.36	3.382
25	MP0847	274	MARBLE	barren	17144.656	398180.233
26	MP0847	311	mineralization	massive sulphides	0.212	4.305
27	MP0847	311.9	mineralization	massive sulphides	0.449	6.276
28	MP0847	313.7	Carbonaceous Schist (Bt-Qtz-Gr±AM±GN)	folliated cc	7924.65	40442.648
29	MP0847	321.5	Carbonaceous Schist (Bt-Qtz-Gr±AM±GN)		13.021	223.543
30	MP0863	42.5	amphibolite	barren	7.621	693.999
31	MP0863	129.6	amphibolite	py veining	64.209	2219.674
32	MP0863	152	amphibolite	py veining	5.762	250.455
33	MP0863	246.4	amphibolite	barren	3141.872	38018.495
34	MP0863	259.9	mineralization	rich in pyrite	0.486	6.385
35	MP0863	272.3	mineralization	rich in pyrite	0.3	2.691
36	MP0863	274.9	mineralization	rich in galena	0.703	6.615
37	MP0863	281.9	MARBLE	graphite	10912.086	143552.248
38	MP0863	299.7	MARBLE	graphite	2994.521	59578.644
39	MP0882	159.2	amphibolite		565.461	42223.784
40	MP0882	194.6	amphibolite-gouge		1.507	71.491
41	MP0882	225.2	fault gouge	sulphides	0.549	19.449
42	MP0882	247.4	Carbonaceous Schist (Bt-Qtz-Gr±AM±GN)	folliated cataclasite	3.917	141.968
43	MP0882	275.1	marble		3641.568	84802.966
44	MP0882	282.8	marble	rhodochrosite vein	164.599	3575.551
45	MP0882	310.8	marble	folliated cataclasite	3102.751	79314.851
46	MP0887	14.8	MG	sulphides	0.643	37.731
47	MP0887	16.7	impure marble	green illite + sulphides	61.77	1730.746
48	MP0887	17.6	marble	sulphides	230.186	3624.394
49	MP0887	24.9	mineralization	massive sulphides	0.124	4.558
50	MP0887	36.7	mineralization marble	sulphides	98.757	3934.274
51	MP0887	55.6	Carbonaceous Schist (Bt-Qtz-Gr±AM±GN)	folliated cataclasite	96.268	4132.794
52	MP0887	112.1	marble	folliated cataclasite	206.95	7051.507
53	MP0887	154.1	mg	black mz gouge	2.478	33.266
54	MP0861	22.5	amphibolite		116.211	2305.666
55	MP0861	62.2	fault gouge		4.532	151.44
56	MP0861	78.2	QCVB		63.075	2336.275
57	MP0861	85.2	amphibolite		230.588	6341.735
58	MP0861	296	Porphyry		107.47	1327.232
59	MP0861	299	Porphyry		891.667	6426.95
60	MP0861	303.6	Porphyry		65.683	459.342
61	MP0861	306.5	GGN	sulphides veins	883.249	6360.39
62	MP0861	307.9	GGN - breccia	sulphides veins	863.101	3724.047
63	MP0861	320.5	Carbonaceous Schist (Bt-Qtz-Gr±AM±GN)	folliated cataclasite	415.874	4376.95
64	MP0867	42.8	Carbonaceous Schist (Bt-Qtz-Gr±AM±GN)		150.828	6398.599
65	MP0867	180.8	amphibolite	py veinlets	145.406	4378.918

66	MP0867	214.6	amphibolite		170.385	2702.174
67	MP0867	244.3	marble		1714.781	37385.807
68	MP0867	247	marble	strong ser alteration	63.405	473.032
69	MP0867	311.3	marble	folliated cataclasite - graphite	3969.046	62417.175
70	MP0867	312	Carbonaceous Schist (Bt-Qtz-Gr±AM±GN)	folliated cataclasite	85.907	1455.739
71	MP0867	314.3	Carbonaceous Schist (Bt-Qtz-Gr±AM±GN)	strong ser alteration	14.868	268.357
72	MP0849	46.5	amphibolite		77.909	2674.207
73	MP0849	160.5	hydrothermal breccia		865.743	19977.213
74	MP0849	164.2	Carbonaceous Schist (Bt-Qtz-Gr±AM±GN)	strong illite alteration + py veinlets	33.131	1174.301
75	MP0849	218.5	marble		18503.962	522520.711
76	MP0849	232.6	marble	folliated cataclasite - graphite	1649.599	36716.268
77	MP0849	316.2	Carbonaceous Schist (Bt-Qtz-Gr±AM±GN)	strong ankerite alteration	219.282	2996.185
78	MP0849	327.5	breccia		344.823	1991.014
79	MP0849	343.8	FBGN		17656.025	93494.078
80	MP0849	345.6	GGN		181.161	1473.823
81	MP0849	357.2	GGN		136.723	1016.154
82	MP0885	12.2	amphibolite		103.97	5879.251
83	MP0885	178.6	fault gouge	probably minor sulphides	7.117	141.521
84	MP0885	198.6	fault gouge	black gouge, probably sulphides	9.321	89.997
85	MP0885	199.8	fault gouge	black gouge, probably sulphides	5.386	39.854
86	MP0885	209.8	Carbonaceous Schist (Bt-Qtz-Gr±AM±GN)	strong ankerite alteration	108.705	1277.299
87	MP0885	214.8	marble	folliated cataclasite	103.717	594.865
88	MP0885	244	marble		940.581	24508.312
89	MP0870	15.3	QCVB		1302.05	15817.584
90	MP0870	17.3	QCVB		38.772	738.102
91	MP0870	37.4	GGN	chlorite alteration	225.45	3658.698
92	MP0870	59.5	GGN	chlorite alteration + py veinlets	51.47	1119.795
93	MP0870	71.3	FBGN		1060.746	40520.586
94	MP0870	80.9	GGN	strong arg + ser alteration	126.534	1434.502
95	MP0870	173	GGN		46.304	1887.634
96	MP0870	230.7	GGN	sulphides	191.952	3245.517
97	MP0870	233.6	GGN	sulphides	60.086	1291.454

References

Arvanitidis N.D., Michael C., Christidis C., Weihed P., Gaál G., Royer J.J., Perantonis G., Bakalis V., Ballas D., 2015b. Using 3D/4D modelling tools in exploration for porphyry and manto-polymetallic potential areas in Eastern Halkidiki peninsula, N. Greece. 3D, 4D and Predictive Modelling of Major Mineral Belts in Europe, Mineral Resource Reviews, Springer Int. Pub.

Haines, H.S., 1998, A structural synthesis for sector Vb of the Madem Lakkos polymetallic sulfide deposit—northeast Greece: Unpublished M.Sc. thesis, London, University of London, 81 p.

Kilias, A., Falalakis, G., and Mountrakis, D., 1999, Cretaceous-Tertiary structures and kinematics of the Serbo-Macedonian metamorphic rocks and their relation to the exhumation of the Hellenic hinterland (Macedonia, Greece): International Journal of Earth Sciences, v. 88, p. 513–531.

Kockel F., Mollat H., Walter H.W., 1971. Geologie des Serbo-Mazedonischen Massive und seines mesozoichen Racmens (Nord-Grecheland). Geol. Jb., 89; 529-551.

Siron C.R., Rhys D., Thompson J.F.H., Baker T., Veligrakis T., Camacho A, Dalampiras L., 2018. Structural Controls on Porphyry Au-Cu and Au-Rich Polymetallic Carbonate-Hosted Replacement Deposits of the Kassandra Mining District, Northern Greece. Economic Geology, v. 113, no. 2, pp. 309–345.

X-Mine project, 2018: Data collection and evaluation report. Work package 1/Ore deposit modelling. Deliverable 1.1- Grant agreement number 730270.

4.4 Skouriotissa-Apliki mining area in Cyprus

4.4.1 Primary sources of data HCM

Initial data provided by HCM to the X-Mine project included several databases, both from primary and secondary resources and both from exploration and from historic mines (Tab. 4.4.1, D1.1 Data Collection and Evaluation Report). Data was provided from the secondary gold resources in the stock pile at Skouriotissa. Historic data was provided for the primary gold exploration target of Tourountzia. And primary geological data in the form of maps, drill logs and assays were provided for the Apliki historic copper mine and the west Apliki copper exploration target.

Table 4.4.1: Overview of the data from HCM available for the project.

Database	Drill holes	Cu/Au assays	3D Model files (Surpac)
Skouriotissa Au stockpiles	-	632	Yes
Tourountzia historic Au exploration	65	410	No
Apliki Main	100	5837	Yes
Apliki West	96	8082	yes

The dataset for Apliki is the most extensive and the area offers the best possibilities of acquiring further data in the scope of the X-Mine project. Thus, the near-mine modelling focuses on the Apliki area.

The database from the Apliki area includes the surface topography, and 100 drill holes from the Apliki mine and Apliki East and 96 drill holes from West Apliki including Cu assay results, geological, mineralogical, and alteration information. 3D block models and files including fault planes were exported from Surpac by HCM and provided to SGU as a reference point for 3D modelling. In addition to the geological data, additional geophysical data was provided.

The following subchapters describe the data sources and processes relevant for the 3D modelling of the Apliki mine and exploration area.

4.4.1.1 Geological maps

Cyprus-type volcanic-associated copper deposits such as Apliki consist of massive sulfide lenses and associated disseminated sulfides in a stockwork zone set in basaltic host rocks.
The stratigraphy of the Apliki area consists of Diabase and Basal Group basaltic complex, Lower Pillow Lavas and Upper Pillow Lavas, which can be distinguished based on their mineralogy and field characteristic. These four mafic volcanic units have been mapped on the surface by HCM employees (Fig. 4.4.1).

The mineralization's at Apliki are associated with complex fault structures. Files with surface traces of some fault structures and fault planes were provided and used as a base for the 3D structural model of Apliki West. Structural measurements from geological maps were also used in the model (Fig. 4.4.2).

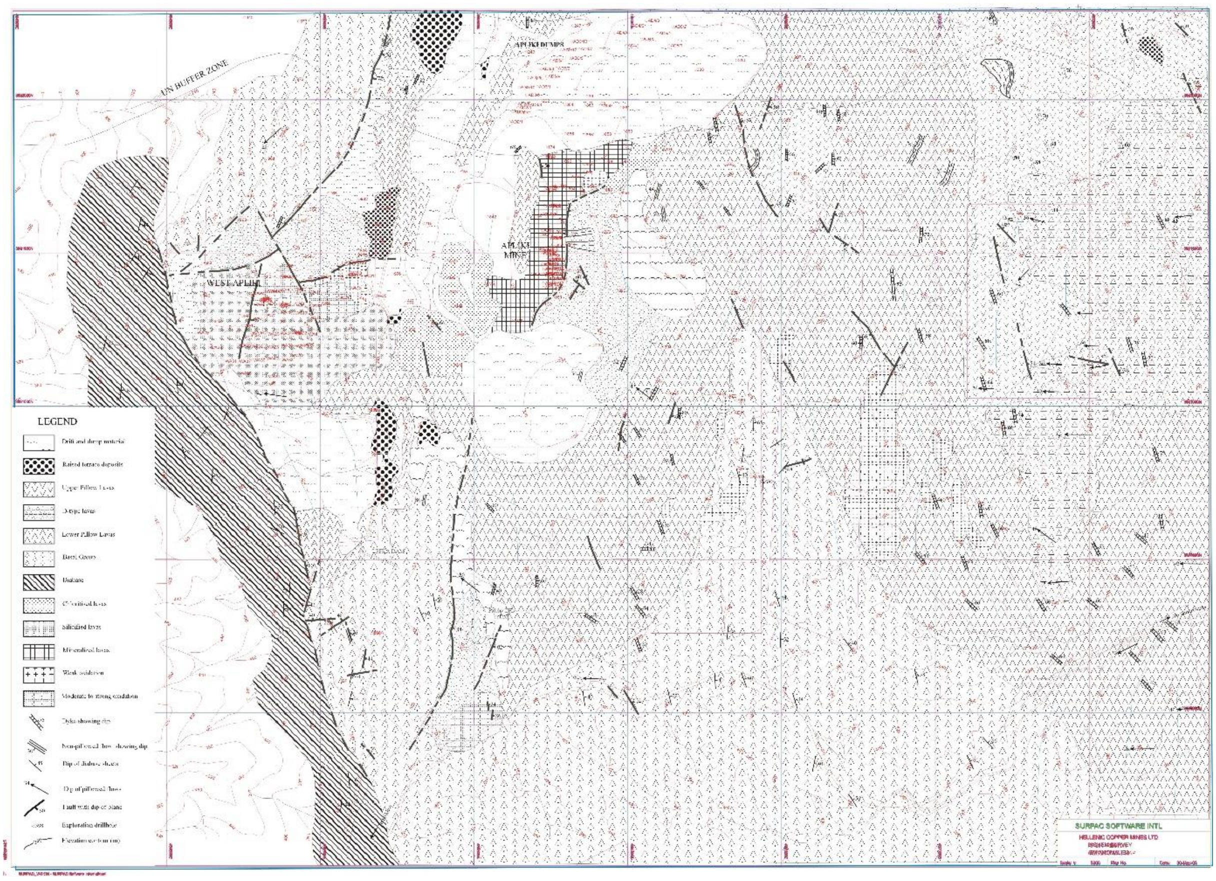

Figure 4.4.1: Geological map of the Apliki area including alterations and structures.

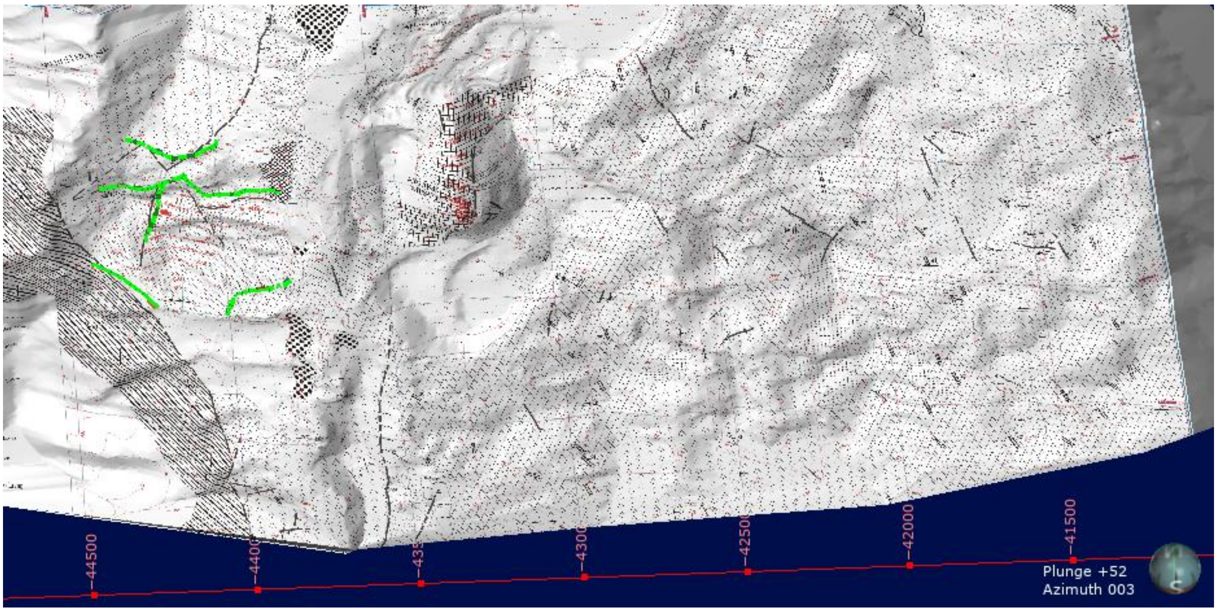

Figure 4.4.2: Geological map of the Apliki area and fault traces draped on topography that served as a base for the modelling.

Different styles of alteration are also indicated on the map and in drillcore logs, including silicification, chloritization, and oxidation, which are all characteristic of the volcanogenic massive sulfide deposits on Cyprus and were used in the modelling.

4.4.1.2 Geophysics and petrophysics

Interpretation and 3D modelling of available geophysical data and collected petrophysical measurements will be completed with additional measurements to be integrated into in-mine 3D ore model as part of deliverable D1.3.

4.4.1.3 Drillcore logs and assays

Drill logs from drill chips from reverse circulation drilling were provided for Apliki and Apliki West. Geological units were not distinguished in drill chips, except for Lower Pillow Lavas, where epidote was present. It is assumed that all lavas that are logged are Lower Pillow Lavas that display several styles of alteration. An overview of the units that were logged can be found in table 4.4.2.

Table 4.4.2: Overview of geological data available from borehole logs for both Apliki and West Apliki.

CODE	Description	Category	Lithology	Mineralization	Alteration	Relative Age
DUM	Dump	Surface material	Dump			Young
DRI	Drift or surface material		Drift			
FILL	Alluvium transported material					
FAU	Fault	Fault	Fault			
DYK	Dyke	Late intrusion	Dyke			
LWE	Weathered lava	Later processes	Lava		Weathering	
GOS	Gossan		Lava		Oxidation	
LOX	Oxidised lava		Lava		Oxidation	
PYR	Massive Pyrite	Mineralization	Massive Pyrite	Pyrite		
UMB	Umber	Sediments	Umber			
SED	Sediment		Sediment			
SHA	Shale		Shale			
TUF	Volcanic tuff	Tuffs	Tuff			
TUF-PYR	Volcanic tuff with pyrite cubes		Tuff	Pyrite		
TUF-SHA	Volcanic tuff with shale		Tuff			
LMI	Mineralised lava	Lavas	Lava	Mineralization		
SIL-PYR	Sillicified lava with pyrite		Lava	Pyrite	Silicification	
LCH	Chloritised lava		Lava		Chloritization	
SIL	Silicified lava or silica		Lava		Silicification	
LEP	Lower pillow lavas with Epidote		Lower Pillow Lava			
LFR	Fresh lava		Lava			Old

Main Apliki Only
West Apliki Only

Assays are only available for Cu and values range between 0 and 10,02%. The assay data served as a base for the modelling of the mineralization.

4.4.1.4 XRT-XRF-generated drillcore data

There is no drillcore available from HCM, but hand samples from a field campaign were cut to fit the drillcore scanner and analysed. Initial results showed unrealistically elevated levels of light elements like lithium that were caused by the high porosity of the rocks. This was adjusted for in a recalculation of the scanning results (Fig. 4.4.3). However, some discrepancies continued to exist, probably due to the sharp edges of the samples and relatively small sample size unlike when scanning drillcore, something that was brought back as input to the further development of the drill core scanning system in WP4. Therefore, to make a reliable assessment of the quality of the scanning results, full core will be scanned in the future if obtainable. The scanning results were not included in the 3D modelling.

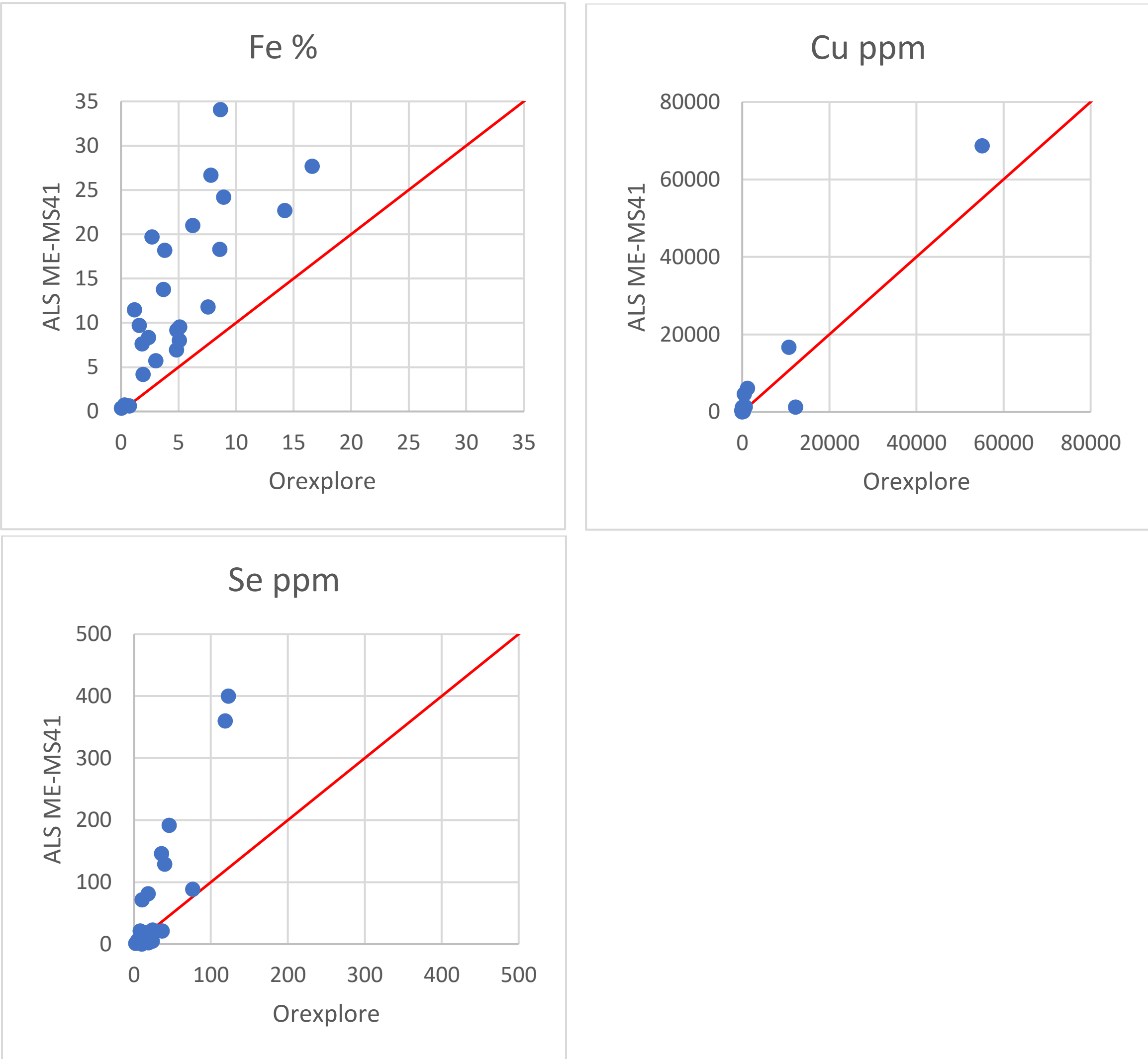

Figure 4.4.3. Example of scanning results for the initial calculation for a main, ore, and trace element.

4.4.2 Integrated 3D ore modelling

The 3D models for the Apliki area were created in Leapfrog Geo Version 4.4.2.

4.4.2.1 Near-mine 3D ore models

The mineralization was created as a numerical model based on assay data for Cu (Fig. 4.4.4 and 4.4.5) and the model is defined by the parameters agreed upon by HCM and SGU outlined in table 4.4.3.

The Cu grade was capped at 1% and subdivided into 4 intervals of <0.05 (non-mineralized), 0.05-0.13 (mineralized), 0.13-0.275 (low grade ore), and <0.275 (high grade ore).

Table 4.4.3: Parameters used for the 3D model of the mineralization at Apliki.

Parameter	**Value**
Compositing length	3 meter
Transform type	Logarithmic
Trend Apliki Main	333,5/15º
Trend Apliki West	63,5/15º
Interpolant	Spheroidal
Total Sill	0,065
Nugget	0
Base range	60
Drift	Constant

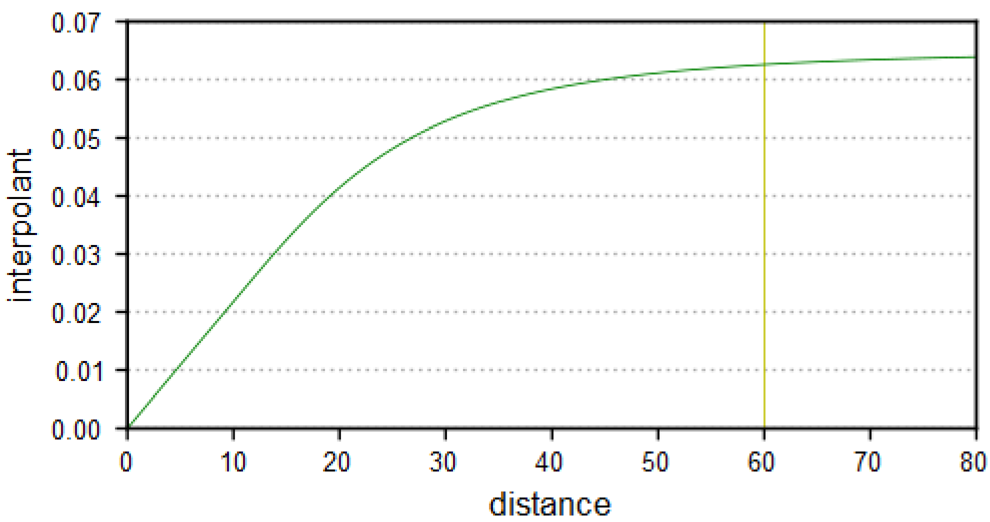

Figure 4.4.4. Variogram for the Apliki numerical Cu mineralization models.

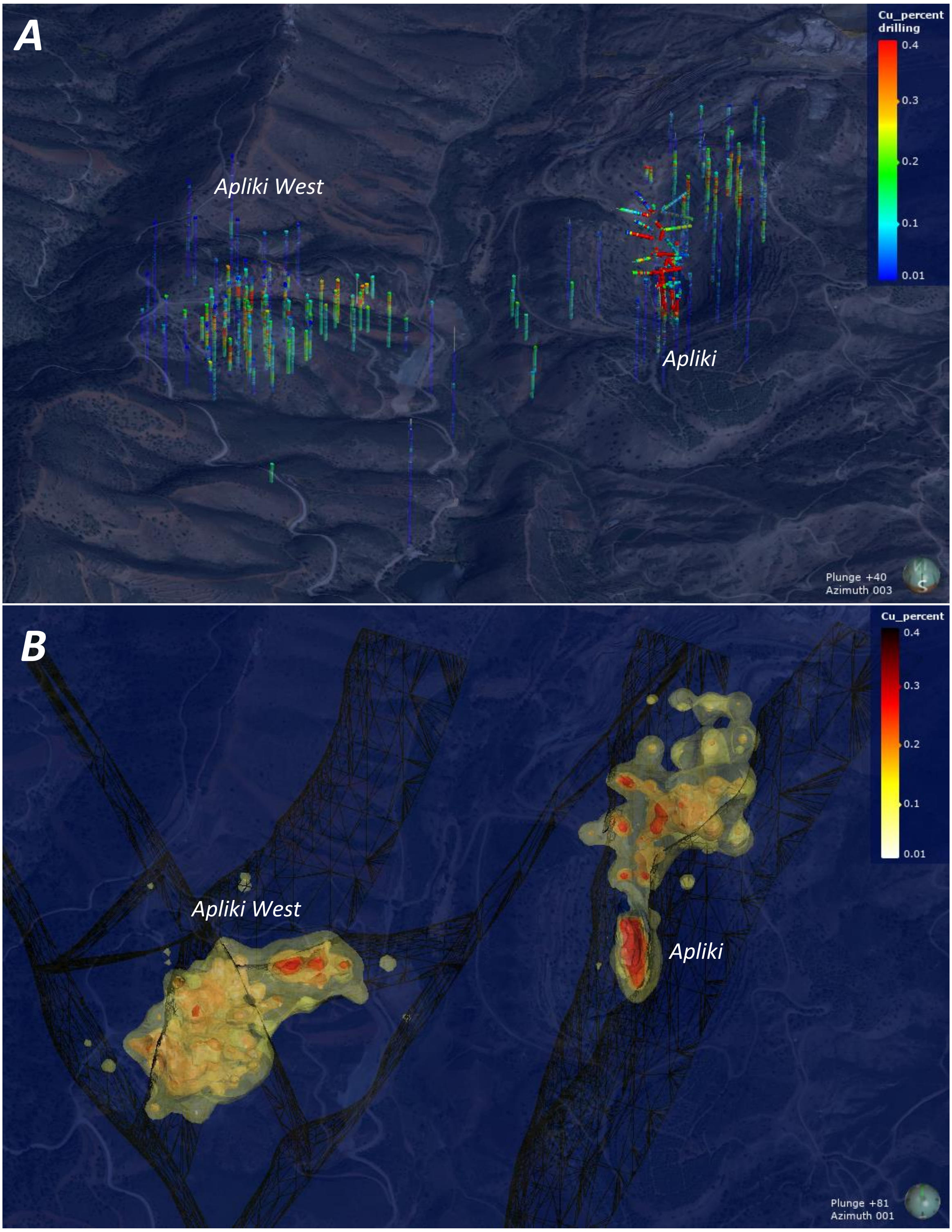

Figure 4.4.5. A: Drill hole assay data for Cu visualized in 3D space. This data constrained the ore deposit model (B). Black meshes in B are fault traces.

4.4.2.2 Near-mine 3D geological model

For the 3D geological model, first the 10 major fault structures were modelled based on their position and structural orientation from the geological map (Fig. 4.4.1) and the files from Surpac (Fig. 4.4.2), resulting in the creation of 11 fault blocks in Leapfrog (Fig. 4.4.6).

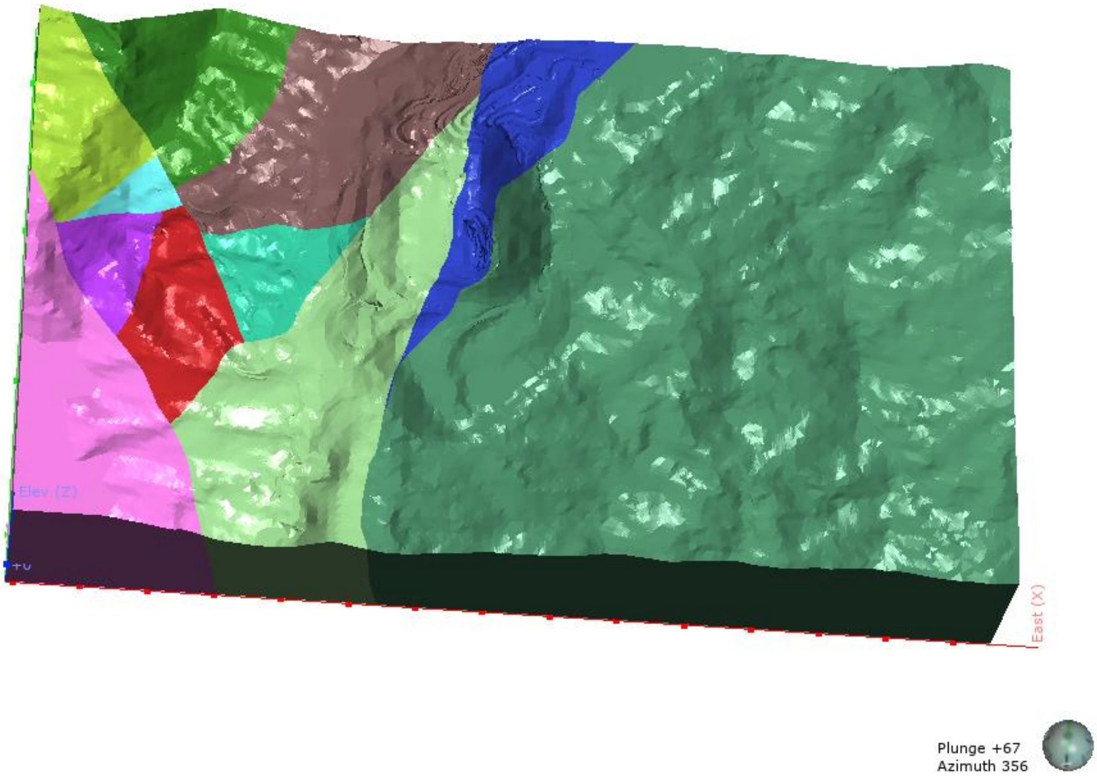

Figure 4.4.6. The geological model was divided into 11 fault blocks by activating 10 faults.

The next step outlined the lithological contacts between the different stratigraphic units based on the geological map (Fig. 4.4.7), resulting in the near-mine 3D geological model (Appendix Leapfrog Viewer file – Fig. 4.4.8). Structural information about the direction of the diabase sheets was also used in the model to better define the orientation of the geological units at depth. A section of the model at 200m elevation level can be seen in figure 6 with the location of several cross sections through the model (Fig. 4.4.9) as indicated.

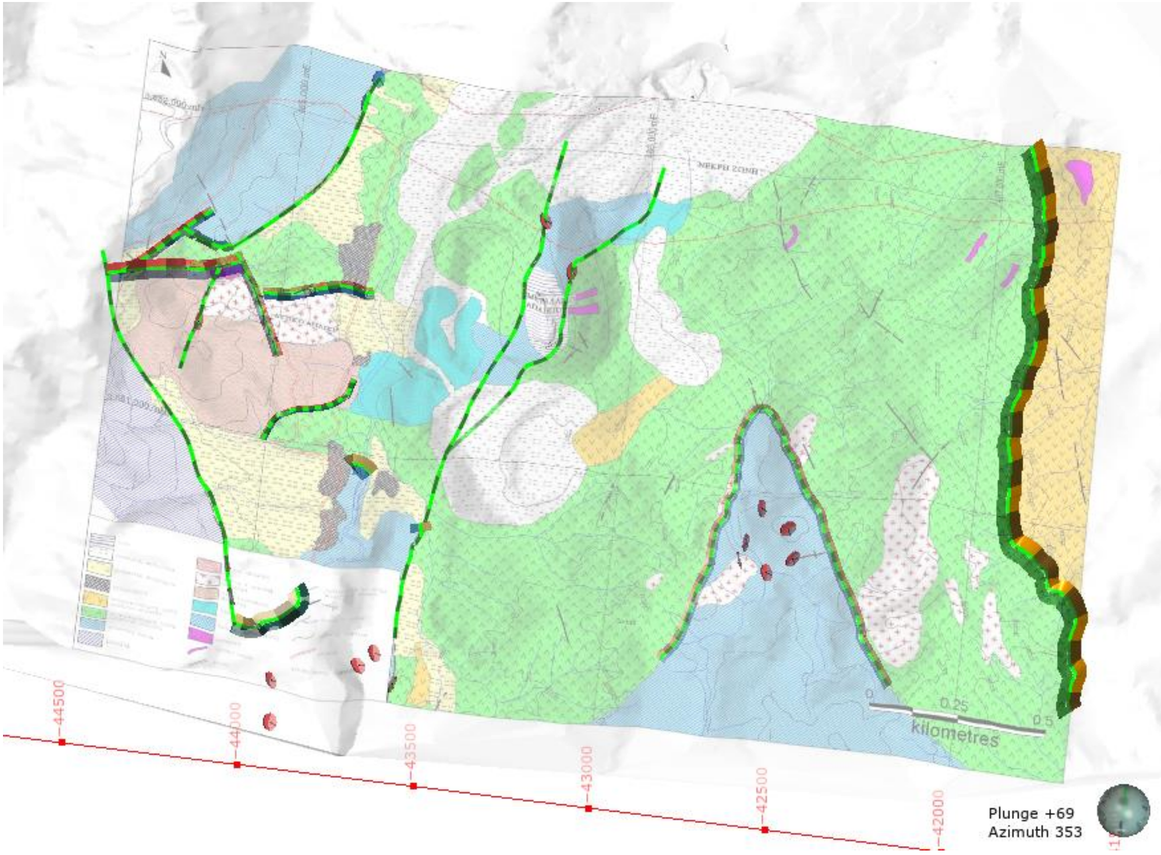

Figure 4.4.7. Polylines tracing the faults and lithological contacts from the geological map and disks indicating the structural measurements on fault planes and diabase sheets which together constrained the 3D geological model (Figure 4.4.6).

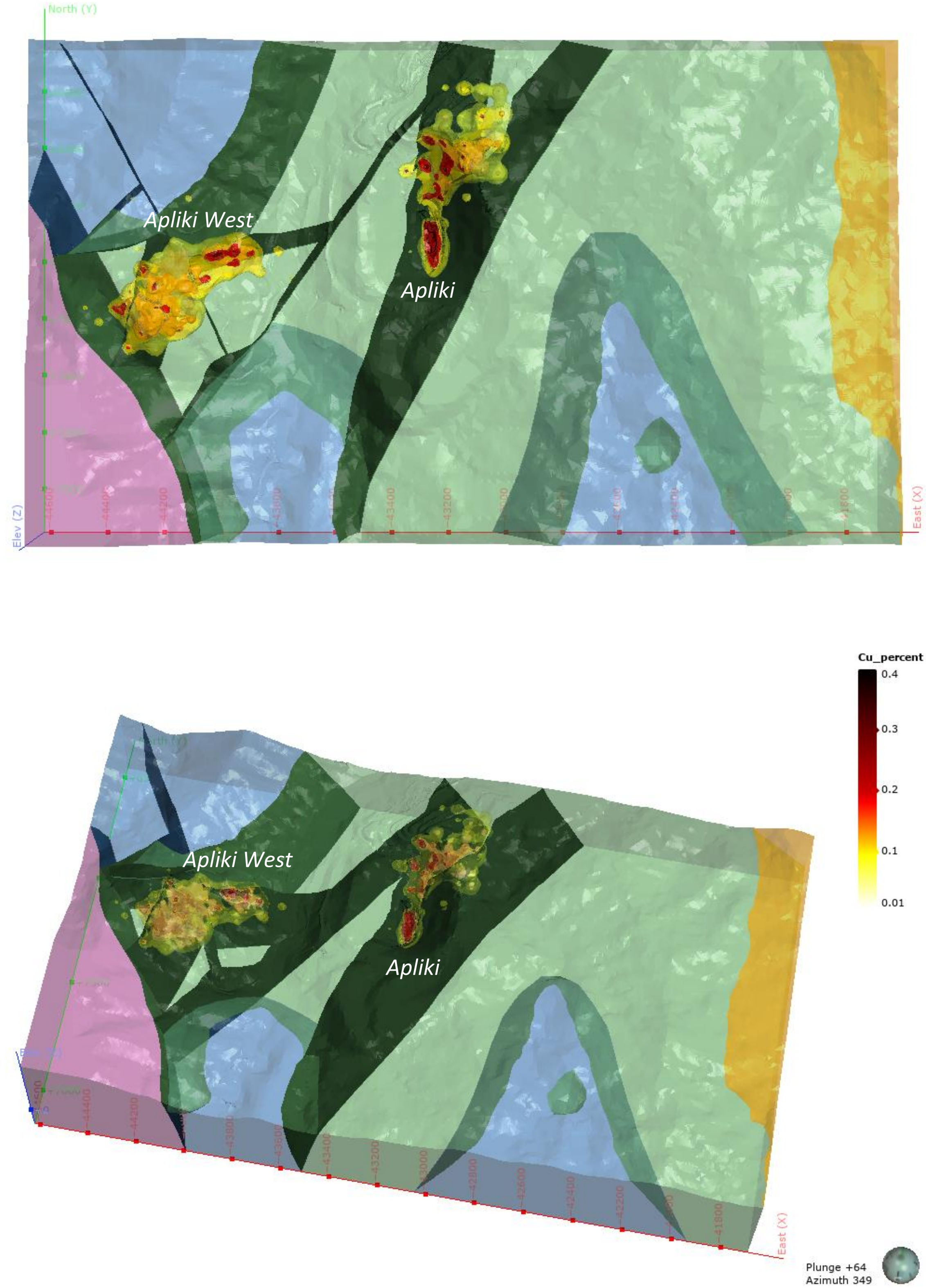

Figure 4.4.8. Impressions of the 3D model. Top: View looking down. Lithological units: Violet – Diabase Group, Blue – Basal Group, Green – Lower Pillow Lavas, Orange – Upper Pillow lavas. Black planes are faults.

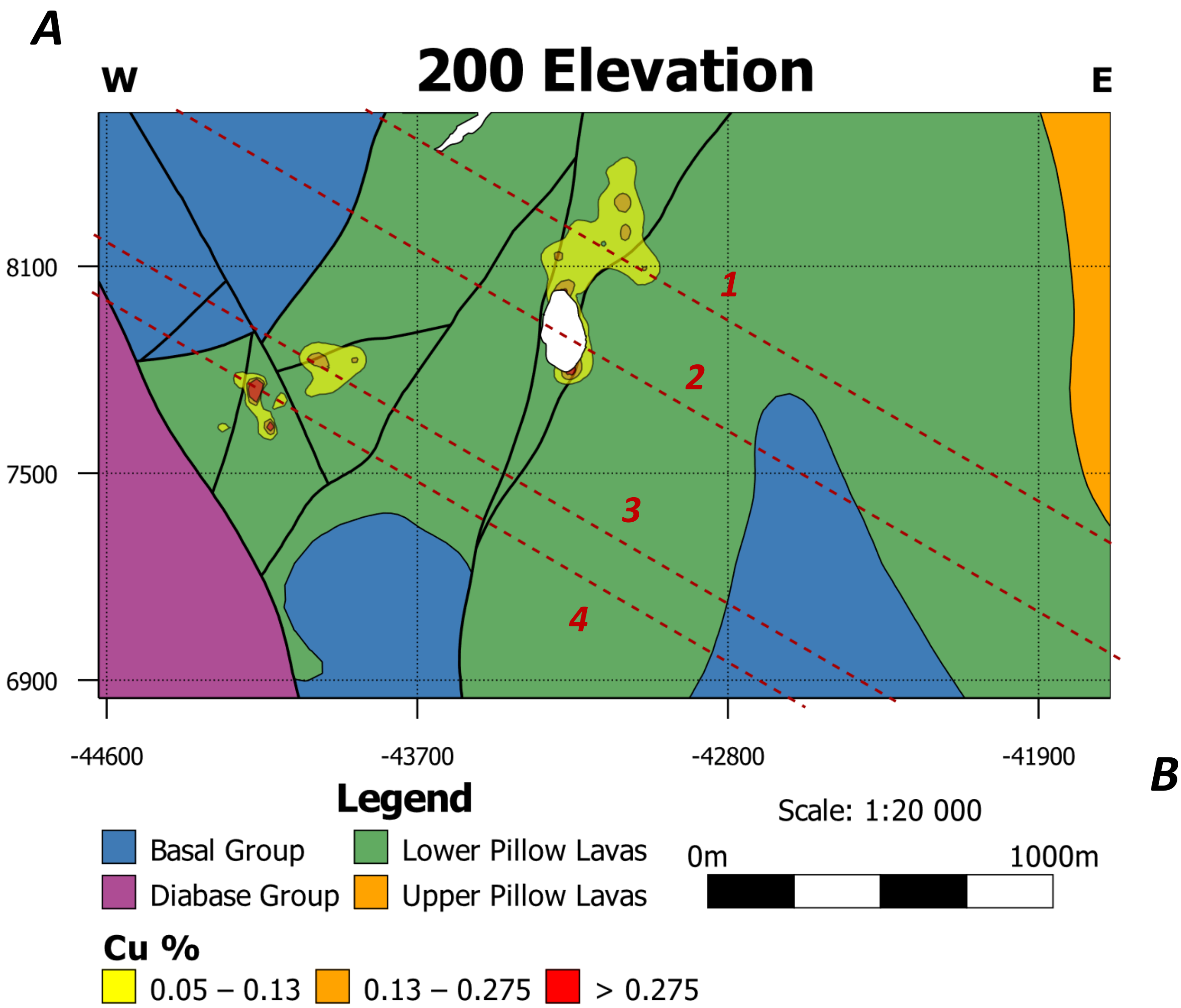

Figure 4.4.9. Section through the 3D geological model at 200m elevation with the location of the cross sections from figure 8 indicated as red dashed lines. The sections from north east to south west are called 1. Apliki East, 2. Apliki Main, 3. East West Apliki and 4. West Apliki.

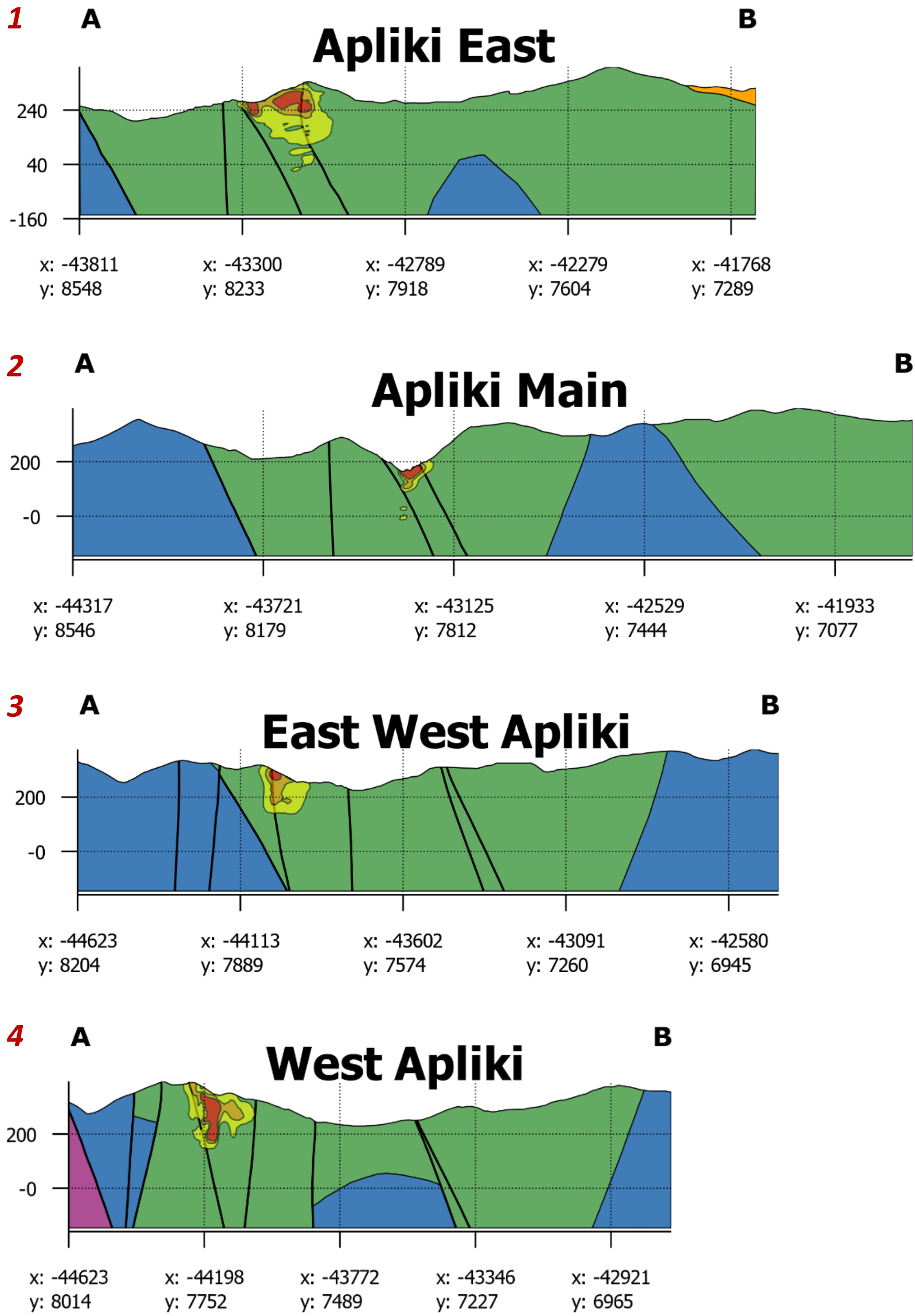

Figure 4.4.10: Cross sections through the 3D model indicated red dashed lines on figure 3 from north east to south west. A clear relationship can be seen between the fault structures and the mineralization.

4.4.3 Approach and on-going work

Preparation for D1.3 In-Mine Ore models has started simultaneously with the work on D1.2. The focus for HCM for D1.3 will be on the West Apliki deposit. On-going preparations include the creation of a fault and mineralization model (Fig. 4.4.11) and an alteration model based on drill hole data (Fig, 4.4.12). The next step will be to integrate new X-Mine surface drilling into these models to refine them into higher resolution, providing a better understanding of the deposits.

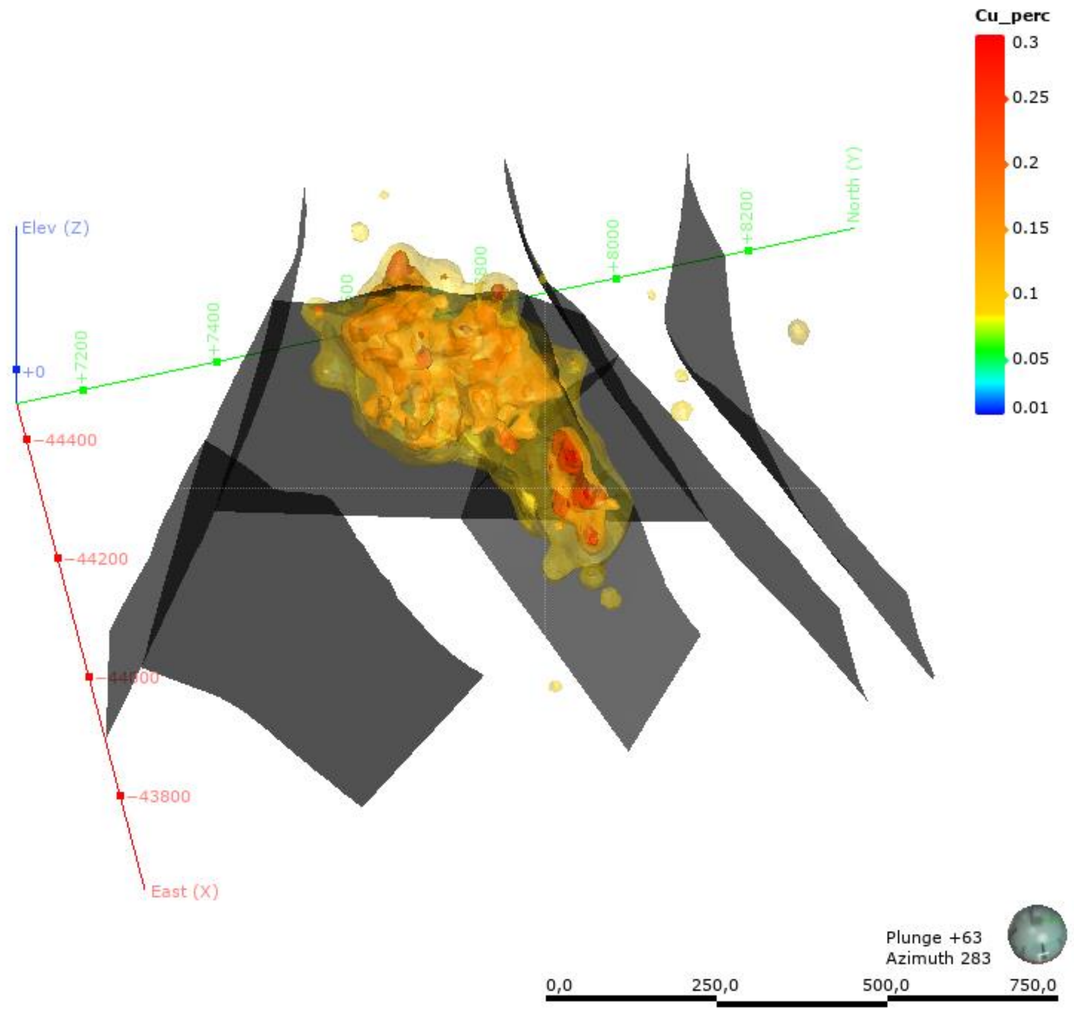

Figure 4.4.11. Mineralization and fault model of Apliki West. A clear relationship can be seen between the mineralization and the fault structures.

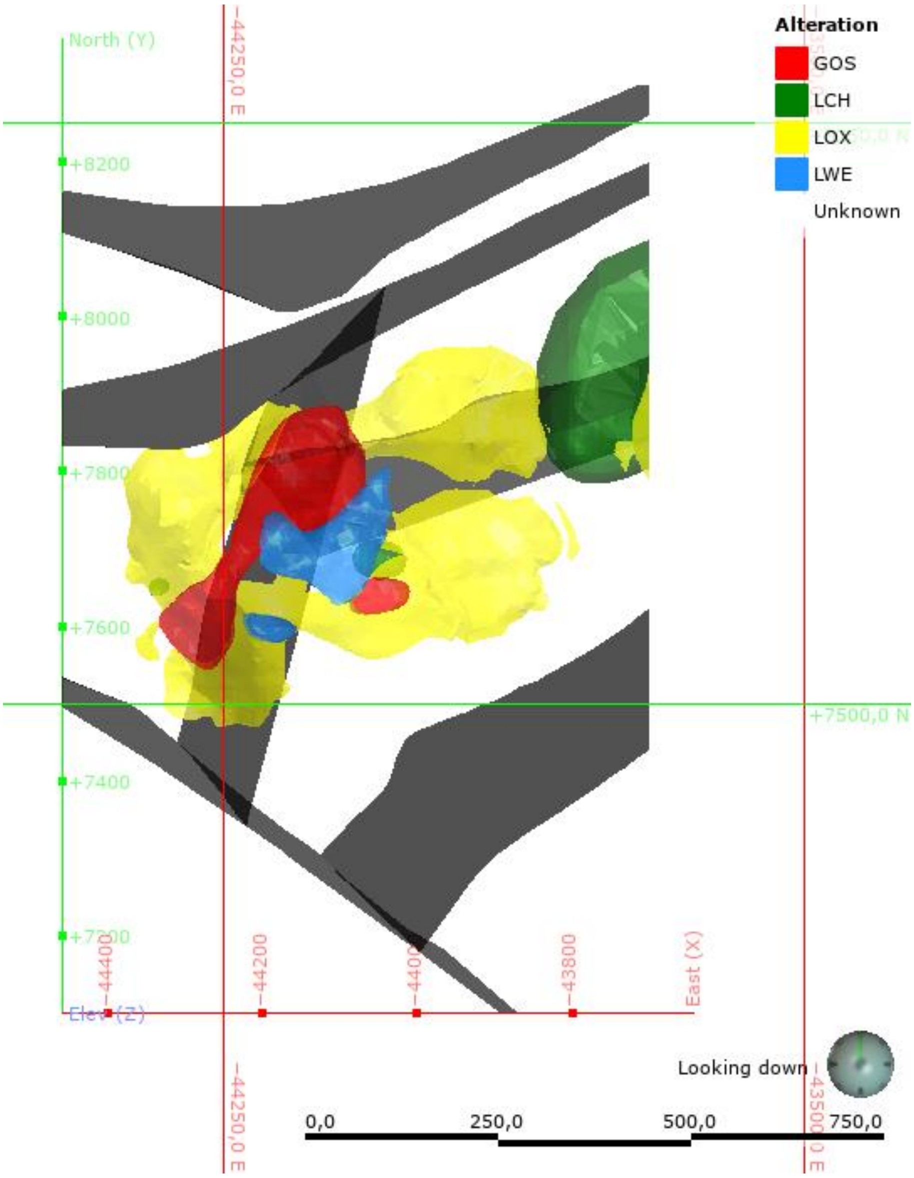

Figure 4.4.12. View looking down on the Apliki West alteration model with Red – Gossan, Yellow – Oxidation, Blue – Weathered Lava, and Green – Chloritized lava.

5. Summary and Conclusions

Using all the available information 3D-geomodelling technology allows to integrate and compare multidisciplinary sources of data to better understand the relationship between faults, lithology, alteration zones, metal zoning and the sites of highest potential for mineralisation. This way of 3D-visual approach has an increasingly important role in integrating and analyzing of geoscientific information for constructing more detailed and efficient mineral exploration models and related applications.

X-Mine driven 3D-geomodelling technologies were applied in four mine pilots in Sweden, Bulgaria, Greece and Cyprus addressing and targeting near-mine exploration considering also the use potential of XRF/XRT scanning. The present D1.2-report demonstrates that the 3D-geomodels, respectively developed for each one target area, contribute in improving knowledge and better understanding of mineralised structures and related geological setting. Further upgrading and progressing of the 3D geological models may prove to be significant tools for exploration and lead to new near-mine discoveries, using the options and the solutions provided by SKUA-GOCAD and Leapfrog Geo.

In Swedish Lovisa mining area pilot the presented geological- and geophysical models provide a good three-dimensional understanding on the shape and spatial distribution of the Lovisa, Håkansboda, Stråssa and Blanka ore bodies as well as on their regional geological framework (Guldsmedshyttan syncline). The modelled ore bodies reach between 38 and 1200 meters below the surface, but most bodies are likely to continue to greater depths according to interpretations from geophysical modelling (Stråssa) and drilling (Håkansboda).

In Bulgarian Assarel, based on the modelled fault network, a total of 122 fault blocks subdivide the near-mine model area. In general, a higher concentration of smaller blocks occurs near the Assarel and Medet deposits, while the Chugovitsa, Petolovo and Assarel volcanic formations form larger fault blocks south of Assarel. This spatial variation may reflect the greater number of NE-aligned “cross-faults” at the deposit sites, and/or the availability of more structural information for these areas. Cross-faulting at both Assarel and Medet comprises c. NE-trending faults that are either bound or cross-cut by WNW- to NNW-oriented faults (Fig. 4.2.7C). These structural intersection zones represent areas of higher secondary permeability and likely formed focused zones of increased hydraulic conductivity and fluid flow, which may have promoted Cu ± Au ± Mo mineralization.

Geological and geophysical modelling has been carried out on a semi-regional- to deposit scale for the Greek Mavres-Petres mining area. Along the Stratoni Fault Zone (SFZ), a semi-regional scale model is presented for the Piavitsa prospect together with two deposit-scale models for the Mavres Petres (MP) and Madem Lakkos (ML) deposits. Modelling on a deposit scale was conducted for the polymetallic Au-Ag-Pb-Zn structural controlled carbonate replacement deposits of Mavres Petres (MP) and Madem Lakkos deposits (ML). The MP deposit model is based on a large number of drill holes (exploration and resource conversion) and in-mine observations and was produced by Hellas Gold Exploration. The model is regularly updated and modified as mining and near-mine exploration is ongoing by the time of writing. Like the semi-regional scale model of Piavitsa, the MP model is intersected by the mineralized Stratoni fault zone dividing the model space from north to south into a footwall-, fault zone-, and hanging-wall block. In general, the presented models provide a good three-dimensional overview on the spatial distribution of mineralization and their hosting lithological units along and within the Stratoni fault zone. The combined visualization of geological and geophysical models at various scales contributed to the characterization of the lithological units and the definition and extrapolation of lithological- and tectonic boundaries at depth.

The Cypriot Skouriotissa-Apliki mining area the 3D models highlight a clear connection between the mineralization and the fault structures. This link was known previously, but a more detailed examination is needed to gain a better understanding of the structures themselves and why the mineralization is related to only some of them. This could also be of interest for future exploration efforts in the area.

6. The way forward

Preparation for anticipated and impending Deliverable 1.3 (D1.3), "In-Mine Ore models" has started simultaneously with the work on D1.2. This goes along with key task of X-Mine WP1 activities to provide the geological context for XRT-XRF drill core scanning and offer a sound platform for calibration of the pilot scanning technology. In relation to this, the oriented drilling underway in all mine pilots and the XRF/XRT scanning of the cores obtained will provide fitting information to build up solid in-mine models.

For example, on-going X-Mine WP1 geomodelling work for the Assarel test site aims to complete the near-mine model and progress to the full construction of the Assarel within-mine model. The integration of these two scales and their respective datasets should provide a comprehensive assessment of the 3D setting and character of the Assarel porphyry Cu-Au system. Importantly, within-mine modelling will incorporate 3D drill core XRT-XRF results using X-Mine pilot scanning technologies (e.g. X-Mine Work Package 5). This information will provide further constraints on the character of the Cu-Au mineralization in 3D space. The planned campaign of oriented drilling within X-Mine WP1 will help further constrain the structural and lithological character of the ore body. In Mavres Petres deposit semi-regional model the displaying stratification of the Stratoni Fault Zone block, with carbonaceous schist at the base, structurally overlain by marble, mineralization and fault gouge at the top, will be further studied along with the new information collected and related 3D in-mine modelling. In Cyprus the next step will be to integrate new X-Mine surface drilling into the near-mine models to refine them into higher resolution, providing a better understanding of the deposits. The ongoing in-mine ore models in west Apliki will include the creation of a fault and mineralization model and an alteration model based on drill hole data using also the new XRF/XRT information.